Electroless Etched Silicon Nanostructures for Solar Energy Conversion

Dissertation

zur Erlangung des Doktorgrades

der Ingenieurwissenschaften (*Dr.-Ing.*)

des Zentrums für Ingenieurwissenschaften

der Martin-Luther-Universität Halle-Wittenberg,

vorgelegt von

Herr M.Sc. Xiaopeng Li

geboren am 14.11.1986 in Jiangsu, China

1. Gutachter: Prof. Dr. rer. nat. Ralf B. Wehrspohn

2. Gutachter: Prof. Dr. rer. nat. Helmut Föll

Tag der Verteidigung: 18.12.2013

Xiaopeng Li: *Electroless etched silicon nanostructures for solar energy conversion*, Dissertation, ©August 2013

ABSTRACT

Pursuing solar energy conversion devices with low cost and high efficiency has become the major task of scientists and engineers in our age. Nanotechnology provides the exciting future for achieving this aim. Si nanowire (SiNW) and porous Si (PSi) have received great attention due to their unique chemical, optical and electrical properties. They offer the possibilities of boosting cell efficiency, reducing the expensive material use, and allowing the deployment of low quality materials. In this thesis, we obtain SiNW and PSi on wafer scale through advanced cost-effective nanofabrication technique ‘metal assisted chemical etching’ (MaCE). In case of SiNW, we find that during etching of ‘dirty’ Si (e.g. metallurgical silicon (MG-Si)), superior purification effect is observed, and metal impurities inside ‘dirty’ Si can be effectively removed. Depending on their concentrations, these dissolved metal ions in the etchant, are capable of developing unique features at SiNWs such as line etching defects or uniform porosity. We additionally apply SiNWs in photoelectrochemical (PEC) water splitting. SiNWs show significant improvements in both photocurrent and on-set potential for hydrogen evolution. We propose that the surface effect strengthens the band bending in SiNWs, and facilitates the separation of photon generated electron and hole pairs.

In case of PSi, we successfully obtain meso-PSi with high uniformity. The porosity can be flexibly tuned by changing HF or H_2O_2 concentration. Compared with traditional electrochemical etching method, this simple new technique has fast etching rate (~1.7 µm/min), and the ability of developing uniform PSi morphology. Thus, it can be directly applied in layer transfer photovoltaics while significantly reducing process complexities and improving the yield.

Contents

ACRONYMS

CVD	chemical vapor deposition
ECE	electrochemical etching
EDX	energy-dispersive X-ray spectroscopy
EG-Si	electronic grade silicon
HER	hydrogen evolution reaction
ICP-MS	inductively coupled plasma mass spectrometry
ICP-OES	inductively coupled plasma atomic emission spectroscopy
MaCE	metal assisted chemical etching
MG-Si	metallurgical silicon
OCP	open circuit potential
PaCE	Pt assisted chemical etching
PEC	photoelectrochemical
PS	polystyrene spheres
PSi	porous silicon
PV	photovoltaic
QSSPC	quasi-steady-state photo conductance
RIE	reactive ion etching
SCR	space charge region
SG-Si	solar grade silicon
SEM	scanning electron microscopy
TEM	transmission electron microscopy
SiNW	silicon nanowire
UMG-Si	upgraded metallurgical silicon

Part I

THE BASICS

INTRODUCTION AND MOTIVATION 1

1.1 Historic background

The energy demand of human-beings is ever increasing. The world-marketed energy consumption would grow by 44% over the 2006 to 2030 period (from 15.8 TW in 2006 to 22.7 TW in 2030). Currently over 80% demand is met by the consumption of fossil fuels in the form of oil (~5.3 TW), coal (~4.2 TW) and natural gas (~3.5 TW) [1,2]. Although oil reserves are diminishing, coal is rather abundant, which is capable of supporting a 30 TW burn rate for centuries [1]. However, the combustion of fossil fuels raises up the CO_2 levels in the atmosphere, which cause an increase in an average of global temperature and a rapid changing climate. Thus, it is imperative to develop and promote carbon-neutral renewable energy sources.

Among various renewable energies, such as wind, geothermal and hydropower energy, solar energy is the most abundant, and universally available. Sunlight strikes the Earth's surface at a rate of ~120,000 TW [3]. Sunlight can be captured and converted into electricity by solar cells. It can also produce chemical fuels such as methanol and hydrogen via CO_2 reduction [4] and water splitting [5,6] in photoelectrochemical (PEC) cells. However, the solar energy is diffuse (~100 mW/cm^2) and diurnal [1,3], requiring large areas of solar collectors to harvest significant amounts of power.

Until now, the high cost and low efficiency hinder the wide installation of these solar energy conversion systems. For example, even though the solar cell industry has experienced a significant expansion in the past decade, the total installed capacity is only ~0.070 TW in 2011. Assuming a 20-year lifetime of the solar cells, the electricity price USD 0.25-0.65/kWh is four times higher than the coal based electricity price ~USD 0.05/kWh [7]. Therefore, it is crucial to develop cost-effective solar energy conversion systems with high light absorption and to break the current bottleneck.

1.2 Semiconductors for harvesting solar energy

The photovoltaic (PV) effect was firstly discovered by the French scientist Edmond Becquerel by shining light on the silver-chloride in an acidic solution [8]. His discovery then sparked the idea of using semiconductor materials as sources to convert solar power into electrical energy. Photovoltaics take advantage of the fact that photons falling on a semiconductor can create free electrons and holes, which can be separated by the junction between two different materials and then collected to power the external circuit.

Until now, hundreds of semiconductors have been discovered and artificially synthesized, mostly commonly used are semiconductors such as CdTe [9], GaAs [10], TiO_2 [11], and $CuInGaSSe_2$ (CIGS) [12].

However, several requirements need to be satisfied for large area installation:

1. Relatively high efficiency >10%,
2. High optical absorption,
3. Inexpensive and non-toxic,
4. Stable under long time exposure to sunlight,
5. Matured industrial processes.

Most of semiconductors fail to fulfill these requirements. For example, TiO_2 can only utilize 5% of the total solar energy due to its large bandgap (3-3.2 eV) [11]. New candidate materials for thin film solar cells lose their competiveness either in high material costs such as CIGS, or in toxicity such as CdTe.

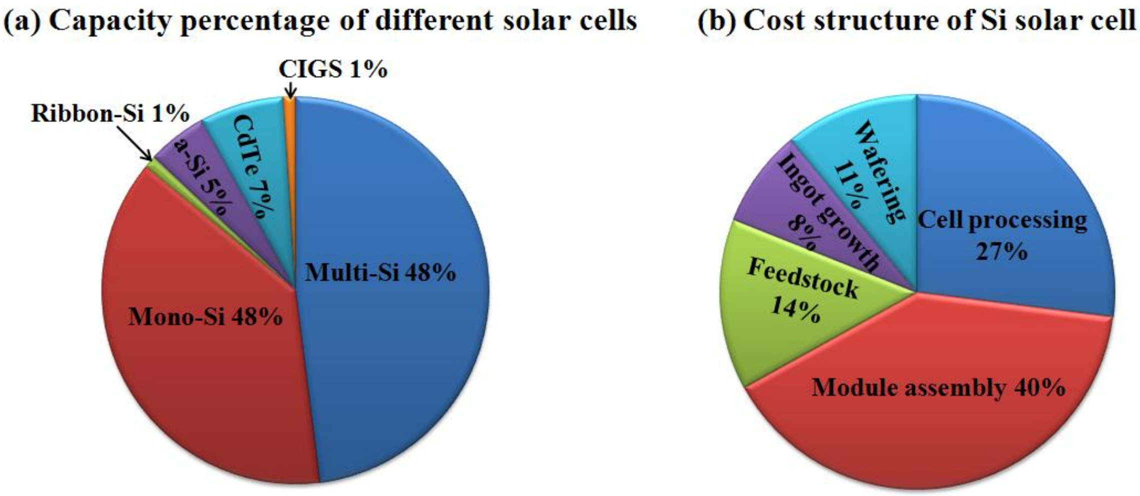

Figure 1.1 Pie charts of (a) capacity percentage of solar cells based on different materials, and (b) cost structure of crystalline Si solar cell. Data is from Ref. 13.

Silicon is probably the only material meeting all requirements at present. Firstly, Si is the second most abundant element (25.7%) of the earth's crust, which guarantees that Si would be available forever [13]. Secondly, Si is stable and resistive to most acids without any protection layer, and it is non-toxic. Thirdly, benefiting from the tremendous development of microelectronics, the process technology of Si is matured. The metal contact and dielectric passivation techniques are readily available. Therefore, Si is currently playing a dominant role in the solar cell market (see **Fig. 1.1**(a)).

Although state-of-art solar cells have achieved an efficiency of ~25% [14], the cost is rather high. The metal impurities have detrimental effects on the Si solar cell efficiency. The transitional metals such as Fe, Cr, and Mo create deep levels in the bandgap inducing strong recombination activities. Their concentrations need to be controlled less than 1 ppm (parts per million) or even 1 ppb (parts per billion) range [15]. Furthermore, Si has a relatively low absorption coefficient throughout much of the visible and near infrared ranges [16]. Crystalline Si solar cell must be thicker than 500 μm to absorb most of light. In PV industry, chemical texturing (e.g. KOH or HF/HNO_3 etching) and antireflective layer coating (e.g. SiNx, SiO_2) are applied to suppress optical reflection [13]. These additional processes again increase the process complexity and cost. Fig. 1.1(b) shows the cost structure of crystalline Si solar cell, Si feedstock and cell processing occupy more than 40% of the total costs.

In order to make solar energy competitive with traditional fossil fuels, continuous price reduction is required. From material perspective, there are three basic strategies to break the current bottleneck for a word-wide installation of Si-based solar energy conversion devices.

Firstly, one can continue to improve the efficiency. However, conventional solar cell designs based on planar p-n junction have rather limited space to further improve the efficiency above ~25% even with advanced surface passivation techniques. The main reason is that the charge carriers generated far from the junction cannot be effectively collected due to the limited minority carrier diffusion length. A new cell design which can absorb nearly all the light above the bandgap, effectively separate and collect all the generated charge carriers would be expected to significantly exceed the current efficiency limit.

Secondly, one can try to reduce the expensive material use such as reducing the thickness of high quality crystalline Si material. This needs a challenging manufacturing approach to ‘peel off’ ~20-50 μm Si thin film from Si substrate, which cannot be realized by current wafer sawing techniques (minimum wafer thickness ~100 μm). This strategy also requires a new antireflection layer technique due to the low light absorption of thin film crystalline Si.

Thirdly, one can use cheaper Si feedstock with more metal impurities than solar grade (99.9999% pure, SG-Si) or even electronic-grade (>99.999999% pure, EG-Si) Si. **Fig. 1.2** shows the solar value chain. Metallurgical grade silicon (MG-Si) is firstly obtained by reducing quartzite (SiO_2) with charcoal in an arc furnace. Afterwards MG-Si (98.5% pure) is purified to SG-Si or even EG-Si by the typical ‘Siemens’ process. Such process is very energy intensive, amounting to the hundreds of kWh/kg. This process is also not environmental friendly. The side products such as halogenated silicon compounds are toxic and flammable [13,15]. Therefore, high fabrication costs are imposed at the purification step. If one can successfully apply the ‘dirty’ silicon including upgraded metallurgical Si (UMG-Si) and MG-Si in solar energy conversion devices without sacrificing too much efficiency, or invent a new simple purification method to avoid the ‘Siemens’ process, it would be an impactive technological breakthrough.

To realize these strategies, we look into current nanotechnological approaches, which may perfectly solve the challenging issues. This is also the main motivation in this thesis.

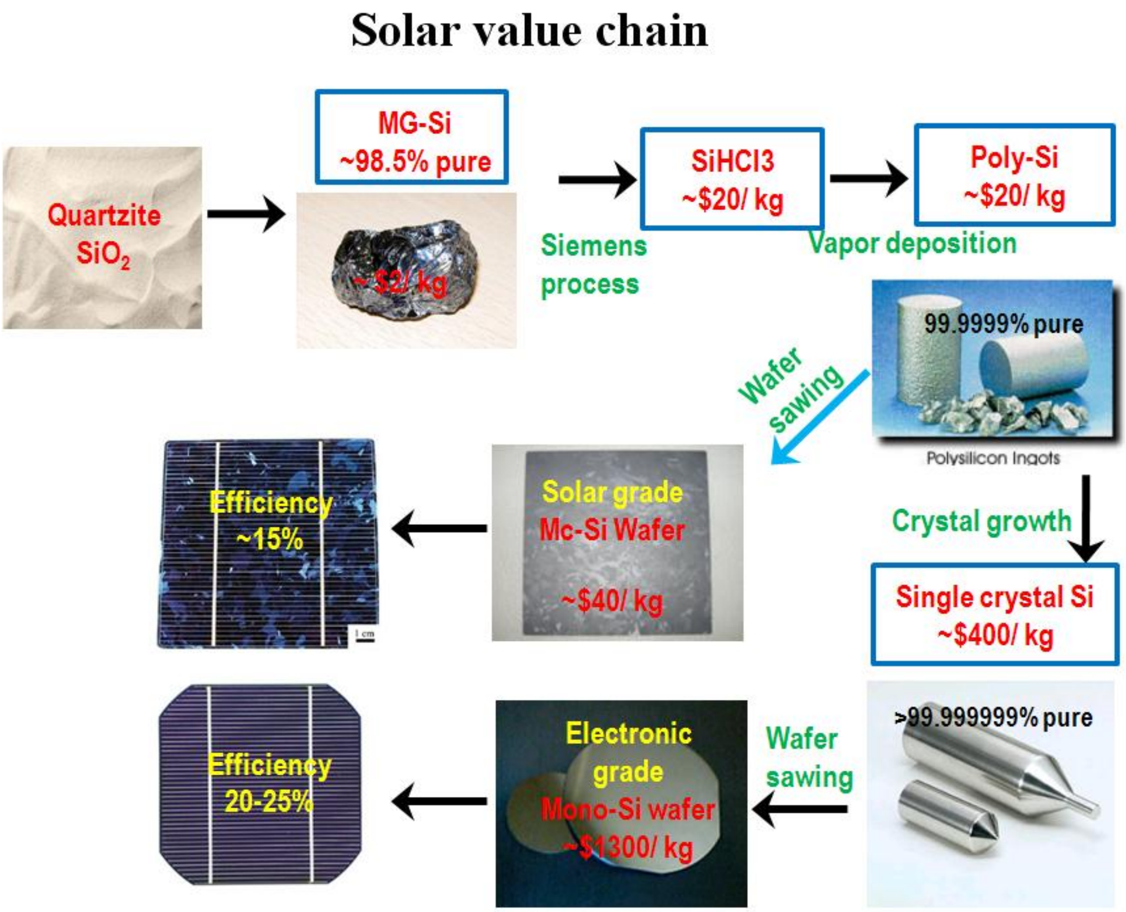

Figure 1.2 A solar value chain showing the fabrication from quartzite to Si solar cells. Parts of figures are from Ref. 17.

1.3 Motivation: Applying Si nanotechnology

1.3.1 Current status: Summary of various fabrication methods

Benefiting from its key role in modern microelectronics and enormous development of nanotechnology in the past decades, Si now possesses possibly the richest family of nanostructures among all semiconductor materials. Various Si nanostructures ranging from 0-D to 3-D have been fabricated, such as nanocrystals [18], nanowire [19], nanotube [20] and porous

Si [21,22].With the shrinkage of structural dimensions and the increase of surface to volume ratio, Si nanostructures become more optically [23], electrically [24] and chemically [25] active than bulk silicon. Due to their unique properties, Si nanostructures have been considered of having a great potential to improve the device performance. Especially in PV applications, nanostructured Si offers new opportunities to address the challenges mentioned before, such as perfect absorption [24], ‘peeling off’ thin film Si [26], applying ‘dirty’ Si in solar cells. In addition, it can also serve as a novel platform for designing a new type of solar energy conversion device. In this thesis, we mainly concentrate on two types of nanostructures: Si nanowire (SiNW) and porous Si, which have been mostly studied in the past decades.

Current nanofabrication methods can be roughly divided into two groups: top-down and bottom-up. The bottom-up methods begin with atoms or molecules to build up nanostructures; on the other hand, top-down methods prepare nanostructures via dimensional reduction of bulk Si by lithography and etching [27]. **Fig. 1.3** shows the schematic setups of commonly used methods for Si nanowire fabrication, including one bottom-up method: chemical vapor deposition (CVD) [19], and three top-down methods: reactive ion etching (RIE) [26], electrochemical etching (ECE) [28], metal assisted chemical etching (MaCE). Fig. 1.5 shows the obtained Si wire structures. Despite of significant advances in the bottom-up methods such as CVD, the cost is still high. The process usually requires high temperature 500-1000 ^{o}C (see **Fig. 1.4**), and the silane precursor cost is higher than ~USD 130/kg. In addition, the metal catalysts would be partially dissolved in SiNWs, resulting in the shortened carrier diffusion length.

For top-down methods, the cost difference also comes from the fabrication processes. RIE loses its competiveness due to the vacuum process and the requirement of additional lithography. ECE is able to create deep pores and wires; however, the obtained structures are always restricted to the dimension of a space charge region (SCR) [28,29]. For commonly used Si wafers with resistivity 1-10 Ω cm, the diameter of the obtained Si wire cannot achieve below 500 nm [30]. Moreover, the etching area is restricted to an O-ring size. It is hard to achieve wafer scale etching with nice uniformity. The risk of leakage of HF solution also imposes serious safety issues.

Meal assisted chemical etching (MaCE) [31-33], is a purely solution processed, high throughput technique. It was firstly invented by Li et al. in 2000 [31], and further developed by Peng et al. [29]. MaCE involves two successive steps, nucleation of metal nanoparticles and anisotropic etching in a solution containing HF and oxidant agents [32]. MaCE is able to create SiNWs with dimension ranging from tens to hundreds of nanometers on a wafer scale.

For porous Si fabrication, commonly fabrication methods are mostly top-down wet chemical etching approaches including stain etching [34], ECE and MaCE. Stain etching has a quite limited etching depth and lack the controllability of pore size and porosity. Therefore, considering its low cost, simple process and high controllability, MaCE is chosen to fabricate SiNWs and porous Si for device application in this thesis.

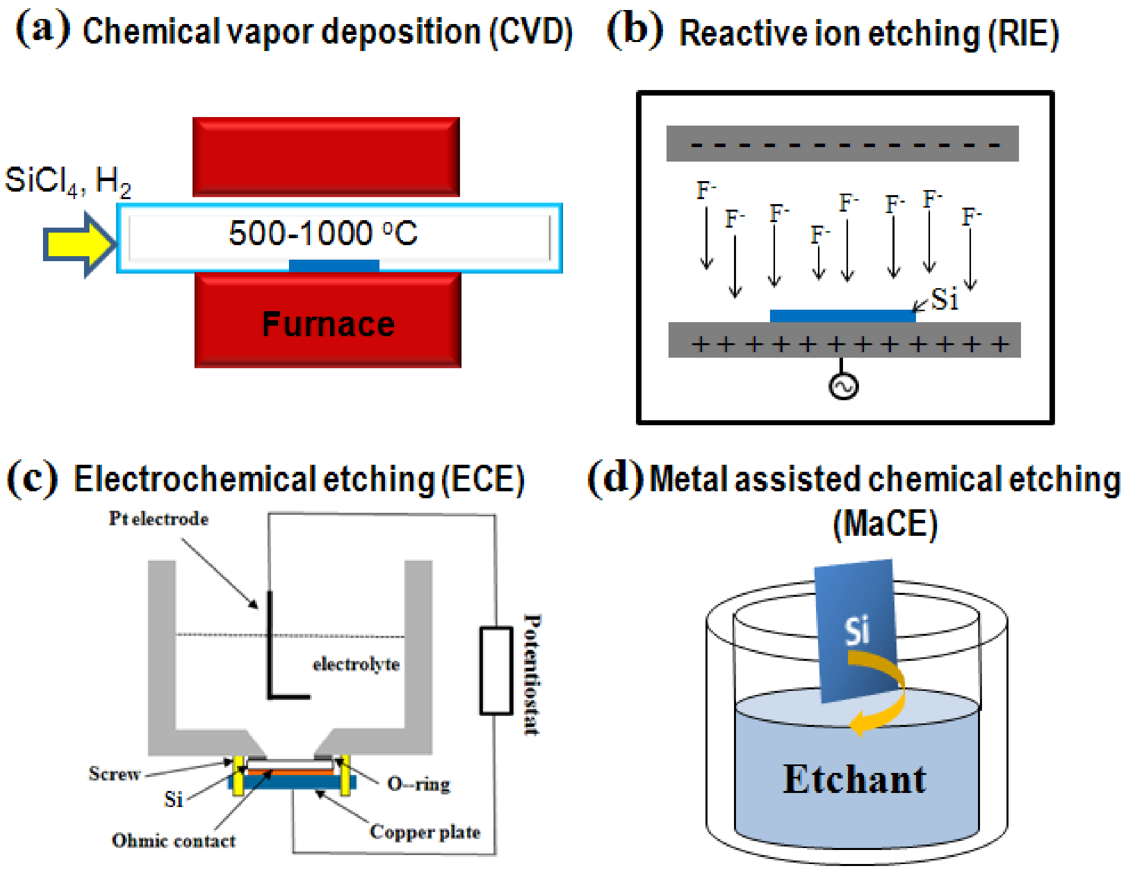

Figure 1.3 Schematic experimental setups for (a) CVD, (b) RIE, (c) ECE and (d) MaCE.

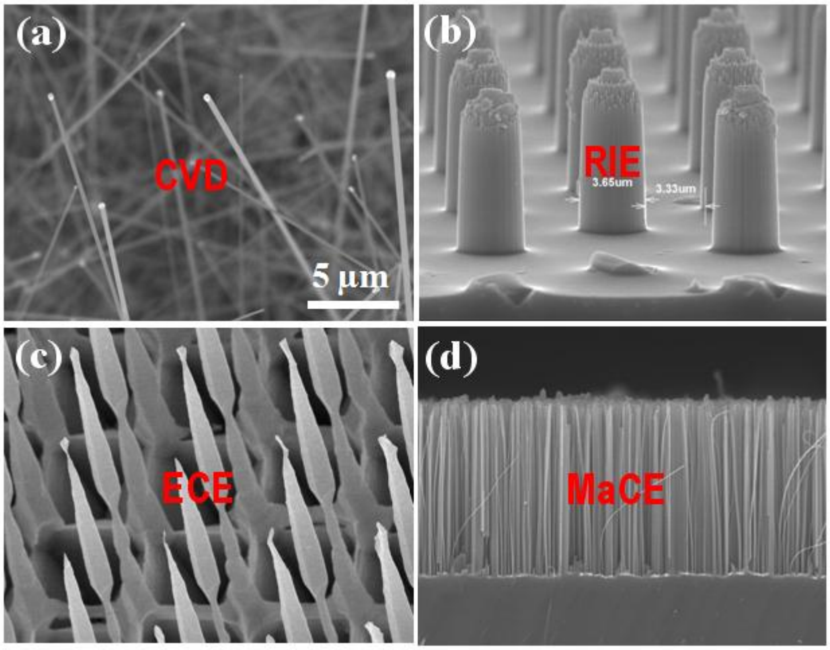

Figure 1.4 SEM images of Si wires fabricated via (a) CVD (White dots at the top of the SiNWs are the Ni catalysts. $SiCl_4$ was supplied as a Si source heating at ~1000 ^oC.), (b) RIE (Si_3N_4 dots worked as the etching mask, the etching gas was a mixture of SF_6 and O_2.), (c) ECE (The starting pattern was a lithography defined inverted pyramid arrays in a Si substrate. The ECE was conducted under a constant potential 2 V with a backside illumination at 300 W. Post KOH etching was applied to obtain free-standing wire arrays [28].), and (d) MaCE (SiNWs were obtained by etching a Si substrate loaded with Ag catalysts in a HF and H_2O_2 mixed solution at room temperature.).

1.3.2 Advanced concepts of applying Si nanowire (SiNW) in solar energy conversion

Fig. 1.5(a) shows the color contrast between a planar EG-Si and a SG-Si wafer before and after NW texturing. The NW sample is black indicating high light absorption. Both experimental and theoretical works have demonstrated that 100 times less Si materials in the form of SiNW arrays can achieve the same amount of absorption as thick bulk Si materials [35]. Previous literatures attributed the strong light trapping properties of SiNW to the gradient refractive index effects and the long optical path lengths of incident lights. With the light absorption advantage, SiNW-based solar energy conversion devices are very promising to continuously improve the device efficiencies. In addition, SiNWs will also allow the continuously thinning the Si substrate to 20-50 μm without influencing much of the total light absorption [36]. By simply taking SiNW as an antireflective layer, the SiNW solar cell shows ~4% efficiency enhancement over the controlled planar Si [37].

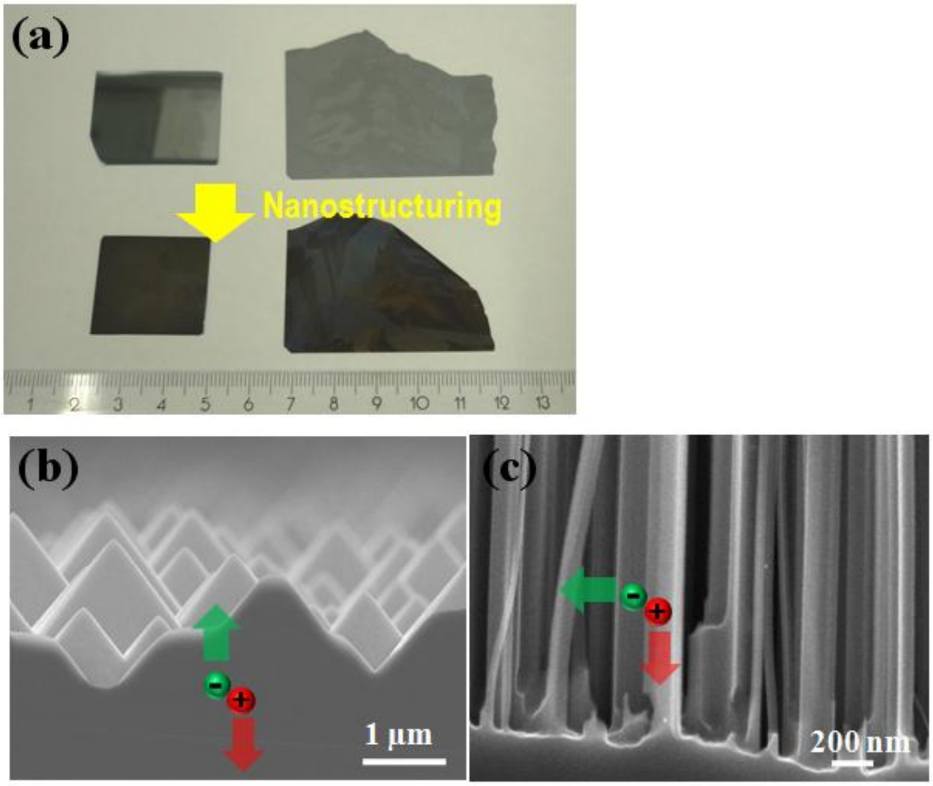

Figure 1.5 (a) Photograph of planar EG-Si and SG-Si wafer before and after NW texturing. Cross-sectional SEM images of the Si surface textured by (b) micro-pyramids and (c) SiNWs. The green and red circles represent electrons and holes, respectively. The arrows are their moving directions.

Another key advantage of SiNWs is that they can orthogonalize the direction of light absorption to the charge carrier collection. Fig. 1.5(b,c) show the difference between the traditional micro-pyramid planar junction design and the nanowire junction deign. The photon generated electrons only need to travel very short distances in a radial direction (smaller than the NW diameter) to be collected [38-40]. In contrast, in the traditional design, the collection efficiency of charge carriers at a given distance from the junction depends on the minority carrier diffusion length. Therefore, for the traditional design, the Si material needs to be extremely pure single crystalline Si to minimize carrier recombination. Since the NW radial junction design is highly tolerant to the defects and impurities inside material [38], low quality material such as UMG-Si or even MG-Si can be applied without degrading the efficiency, or even shows higher efficiency than the high quality Si solar energy conversion device with the traditional design.

The first theoretical work of this new concept was demonstrated by Atwater group in 2005. The calculation demonstrated that the radial p-n junction can greatly enhance the charge carrier collection [38]. Inspired by the theoretical work, the first radial p-i-n NW junction device was realized by Lieber group in 2007 with single NW efficiency 3.4% [39]. However, the continuous work on the SiNW radial p-n junction solar cells met several difficulties, such as exactly controlling the doping level at the nanoscale, severe surface/interfacial recombination, high resistance and large shunting [40]. The efficiency of SiNW based solar cell was reported only 0.1% in 2007 [41] and 0.5% in 2008 [42]. Therefore, lots of work switched to the microwire radial p-n junction solar cells [43], SiNW-organic polymer hybrid solar cells [44] and SiNW based photoelectrochemical (PEC) cells [45]. Moderate efficiencies ~11% for the microwire [46] and ~10.3% for the SiNW-polymer hybrid solar cells [47] have been achieved with adequate metal electrode design and surface passivation.

In contrast to the solid-state radial junction Si wire solar cell, the PEC cell requires no high temperature dopant diffusion or CVD process. Since the electrolyte closely contacts with the NW forming conformal radial NW-electrolyte junctions, the NW based PEC cell becomes a perfect platform to investigate the NW formation and facilitated carrier collection in the solar energy conversion [48].

Motivated by the above advantages, in most of this thesis (Chap. 3 and 5), we concentrate on fabricating SiNWs fabrication from ‘dirty’ Si including UMG- and MG-Si, and exploring the merits of SiNW application in PEC cells for H_2 fuel production.

1.3.3 Advanced concepts of applying porous Si

PSi can be classified into three types in terms of pore diameter d: micro-PSi ($d \leq 2$nm, meso-PSi $2 < d \leq 50$ nm and macro-PSi ($d > 50$nm) [49]. Currently there are three basic ‘tricks’ using meso-PSi [50] and macro-PSi [51,52] to fabricate and detach thin film Si from the crystalline Si substrate.

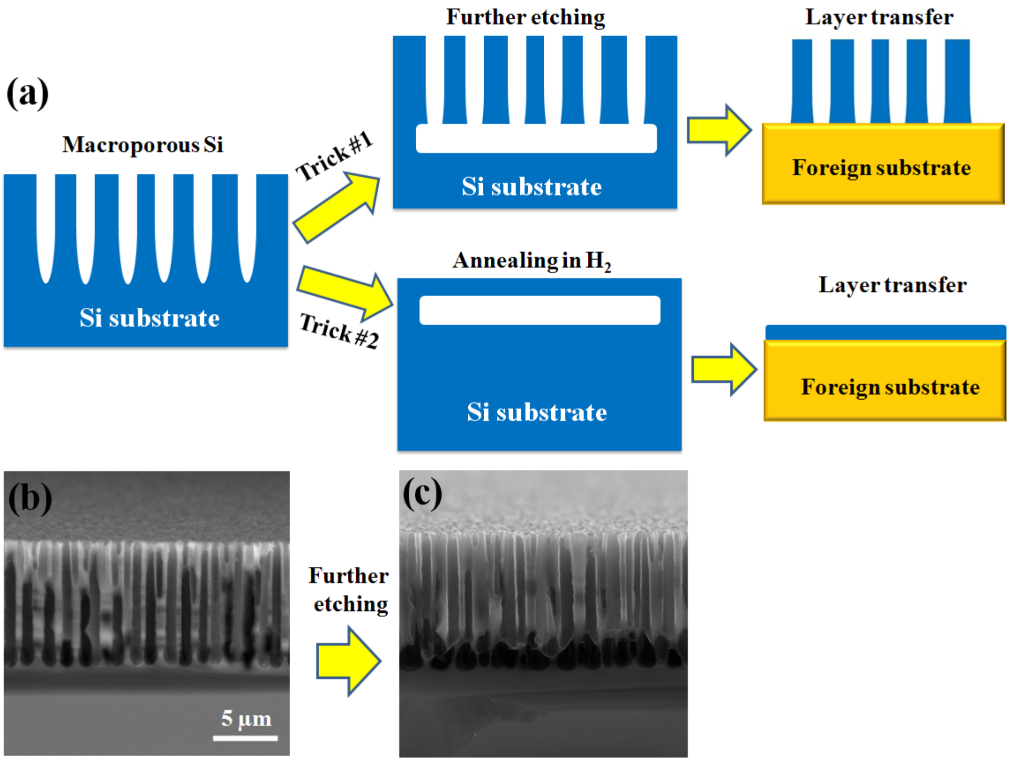

Figure 1.6 (a) Schematic of two different layer transfer tricks based on patterned macro-PSi. (b,c) SEM images of non-patterned macro-PSi formed by ECE. Sample shown in (c) has an additional highly porous Si separation layer.

Fig. 1.6 shows the processes of two tricks based on macro-PSi. Both tricks start with lithography defined macro-PSi layer with different etching technique: ECE (#1) and RIE (#2). The #1 trick developed by Brendel et al. [51] adds a separation layer by increasing the etching current. The macro-PSi layer is detached for further solar cell fabrication. The final efficiency can achieve 13.1%. The #2 trick directly anneals the macro-PSi in H_2 atmosphere at 1150 ℃, a thin Si film with thickness 1-5 µm can be formed ready for detachment. After solar cell fabrication, the cell efficiency can achieve ~4% [52]. Both methods have the advantages of greatly reducing the thin Si film thickness and reusing the mother substrate, however the disadvantage of using lithography imposes extra costs. Moreover the production speed is very limited by the batch processes of RIE and ECE.

The meso-PSi trick was also developed by Brendel et al. [50,53] as shown in **Fig. 1.7**. ECE is applied to fabricate porous double layers consisting of a high porosity layer beneath a low porosity layer [54]. Upon annealing at temperatures above 1000˚C in H_2, the upper layer takes on an originally polished and monocrystalline quality, which allows further epitaxial growth of a higher quality silicon layer. Compared with the macro-PSi tricks, the meso-PSi trick requires no lithography; moreover, the fabricated solar cells from meso-PSi have achieved the highest efficiency 19.1% [50] among three tricks.

Since MaCE has much simpler processes than ECE and RIE, and it is suitable for industrial production, in this thesis (Chap. 4), we apply MaCE to produce meso-PSi and control its porosity for future application in layer transfer photovoltaics.

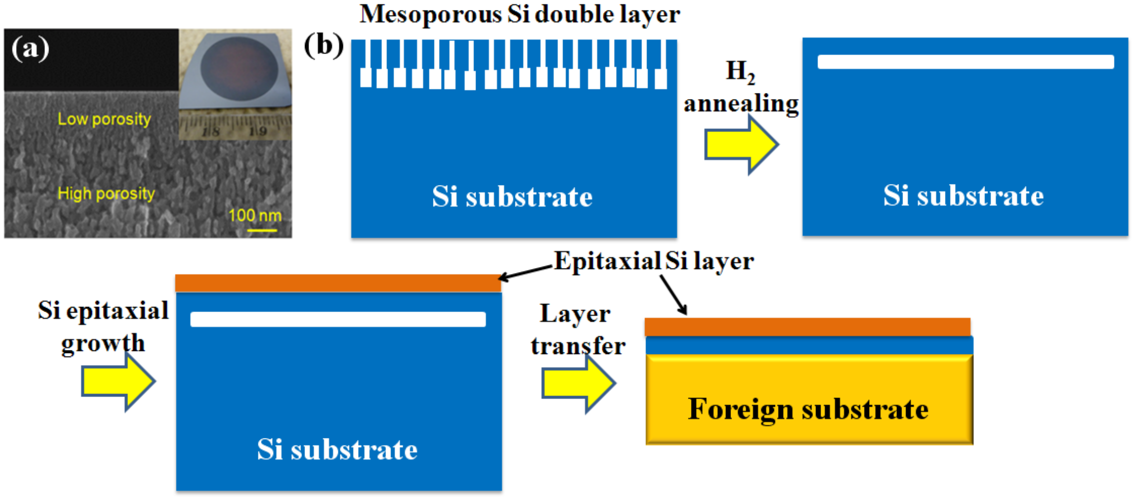

Figure 1.7 (a) SEM image of double layered meso-PSi formed by a two-step etching process. The inset is an optical image of the obtained meso-PSi sample. (b) Schematic diagrams of a layer transfer process based on a double-layered meso-PSi.

1.4 Introduction to metal assisted chemical etching (MaCE):

Basic mechanism and expected purification effect

MaCE consists of two steps: 1. Metal nanoparticle (NP) or film deposition 2. Metal catalyzed silicon etching in aqueous HF solution mixed with an oxidant [33]. The formation of Si nanostructures depends on the anisotropic properties of MaCE: Silicon beneath the metal NPs would be dissolved much faster than its surrounding area.

Since metals should be noble enough for avoiding fast dissolution in HF solution, metal catalysts including Cu [55], Ag [56], Au [57], Pt [58] and Pd [59] have been used and studied. For SiNW synthesis, Ag and Au were found to be the ideal catalysts without formation of extra porous layer [33]. Though controlling the shape of metal catalysts during deposition process, the resulting Si nanostructures can be determined as seen in **Fig. 1.8**. The metal deposition can be achieved by various methods such as thermal evaporation, sputtering and galvanic displacement. Due to its low cost and simplicity, galvanic displacement is favorable in most of literatures for the SiNW synthesis.

The galvanic displacement can be conducted by simply immersing Si wafer into the HF solution mixed with metal salt, such as $AgNO_3$ and $KAuCl_4$. **Fig. 1.9**(a) shows the diagrams of the comparison between the electrochemical potentials of metal redox systems and the Si band edges. Taking Ag as an example, the electrochemical potential of Ag^+/Ag is located below the valence band of Si; therefore, Ag^+ ions are able to inject hole into Si. During this process, Ag^+ would be reduced accompanying Si dissolution. The half reactions are as follows [33]:

Metal reduction: $Ag^+ + e^- \rightarrow Ag$ E_{Ag}= 0.7996 V (vs. NHE) (e.q. 1.1)

Si dissolution: $Si + 4HF_2^- \rightarrow SiF_6^{2-} + 2HF + H_2\uparrow + 2e^-$ E_{Si}= -1.2 V (vs. NHE) (e.q. 1.2)

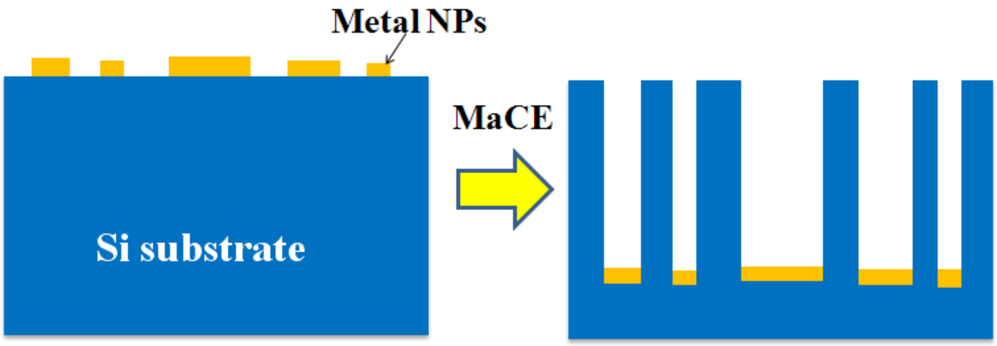

Figure 1.8 Schematic of Si substrates loaded with metal nanoparticles in different sizes before and after etching.

After coating Si with interconnected metal NPs, the Si samples are etched in a mixed solution with HF and an oxidant. For MaCE, there are several oxidants available, e.g. $K_2Cr_2O_7$ [60],

$KMnO_4$ [60], $AgNO_3$ [61], $Fe(NO)_3$ [32] and H_2O_2 [31]. As shown in Fig. 1.9(a), the electrochemical potentials of these oxidants are much more positive than the Si valence band. They are able to inject holes to Si and cause Si dissolution. Until now, $AgNO_3$ and H_2O_2 are considered as the best oxidants for SiNW synthesis, while other oxidants such as $K_2Cr_2O_7$, $KMnO_4$ lead to non-uniform porous structures [60]. Using $AgNO_3$ for metal coating and also as the oxidant for SiNW fabrication can be achieved by simply immersing Si samples into HF and $AgNO_3$ for long time [61]. Thus this approach is so-called 'one-step' etching.

In our work, we adopt a 'two-step' etching method using H_2O_2 as the oxidant, because the SiNW growth speed in HF + H_2O_2 is much faster than that in HF + $AgNO_3$, and the H_2O_2 concentration can be used as another factor for tuning the porosity of Si nanostructures. As shown in Fig. 1.9(c), Si etching involves a local coupling of two redox reactions at the metal NPs. The etching process starts with H_2O_2 reduction. The surface area of metal NPs facing the etchant would act as cathodes:

Cathodic reaction [62]:

$H_2O_2 + 2H^+ \rightarrow 2H_2O + 2h^+$, E_{H2O2}= 1.76V (vs. NHE) (e.q. 1.3)

Since the metal-Si interface exhibits a much lower Schottky barrier height as compared to the electrolyte-Si contact, the generated holes (h^+) are effectively injected though the metal-Si contact [55], leading to a h^+-rich region of silicon which surrounds metal NPs [59,63]. Thus, NPs facing the Si act as anodes for Si dissolution.

Anodic reaction [62]:

Si dissolution could either be in divalent state (dissolution valence n=2)

$Si + 4HF_2^- \rightarrow SiF_6^{2-} + 2HF + H_2\uparrow + 2e^-$ E_{Si}= -1.2 V (vs. NHE) (e.q. 1.4)

Or in tetravalent state (electropolishing, n=4)

$Si + 2H_2O \rightarrow SiO_2 + 4h^+ + 4e^-$

$SiO_2 + 6HF \rightarrow H_2SiF_6 + 4\ H_2O$ E_{Si}= -0.84 V (vs. NHE) (e.q. 1.5)

The driving force for anodic dissolution is the electrode potential difference between anode and cathode. As a consequence of the microscopic reactions, Si beneath the metal NPs is dissolved and the NPs drill deep into the Si substrate.

Since Si(100) plane has the fewest bonds to break than other planes, the ‘drilling’ directions of metal NPs mostly follow the <100> direction [33]. In order to explain the autonomous motion of metal NPs, Peng et al. [64] proposed an electrokinetic model as shown in Fig. 1.9(c, d). The electron flow through NPs is coupled with proton translocations in the fluid, which implies an electrical field capable of introducing electrokinetic effects. However, this model cannot explain the unexpected non-<100> directions, we propose that the unexpected motion of metal NPs is due to the unbalanced cathodic current (j_C) and anodic current (j_A), which would be discussed in detail in Chap. 4.

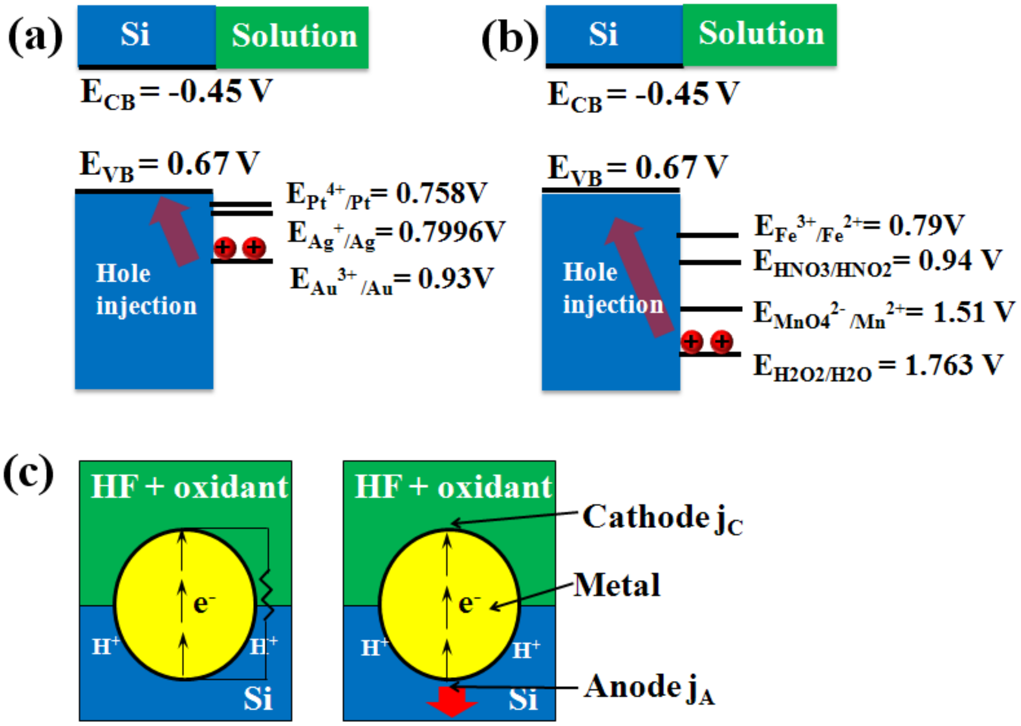

Figure 1.9 (a) Comparison of the Si band edge energies and the electrochemical redox potentials of different metals ($E_{M^+/M}$). (b) Comparison of the Si band edge energies and the electrochemical redox potentials of various oxidants. E_{CB} and E_{VB} are the conduction band and the valence band of Si, respectively. Red circles represent holes. Red arrow represents the hole injection into Si. (c) Schematic illustration of the autonomous Au particle movement in bulk Si.

Another unique feature of MaCE is that large surface areas of Si nanostructures are exposed to the acidic etchant during the ‘drilling’ process of metal NPs. Thus, we expect that metal impurities including their precipitates and silicides would be dissolved upon exposing to the HF solution. In other words, MaCE would induce enhanced purification effect than traditional acid washing technique. It may provide another way to skip the expensive ‘Siemens’ process by nanostructuring ‘dirty’ Si. The purification effect and the underlying mechanism will be discussed in Chap. 3.

Besides the capability of fabricating SiNWs, MaCE is also able to form highly porous structure. Several literatures have reported using Pt to fabricate micro- or meso-PSi due to its strong catalytivity in decomposing H_2O_2 over Ag and Au [31,65]. However, there are no systematic studies, the origin of porous Si layer formation remains clear. This is also part of the motivation of investigating Pt nanoparticle assisted chemical etching (PaCE) in Chap. 4.

1.5 Introduction to photoelectrochemical (PEC) water splitting using Si as photocathode

In contrast to solid state solar cells, PEC cells can directly convert solar energy to chemical fuels such as H_2, methanol and glucose [66-68]. This technique offers an alternative way to store the solar energy in a chemical way; the generated fuels can be stored, transported and burnt, solving short-term fluctuations in output from sunlight capture.

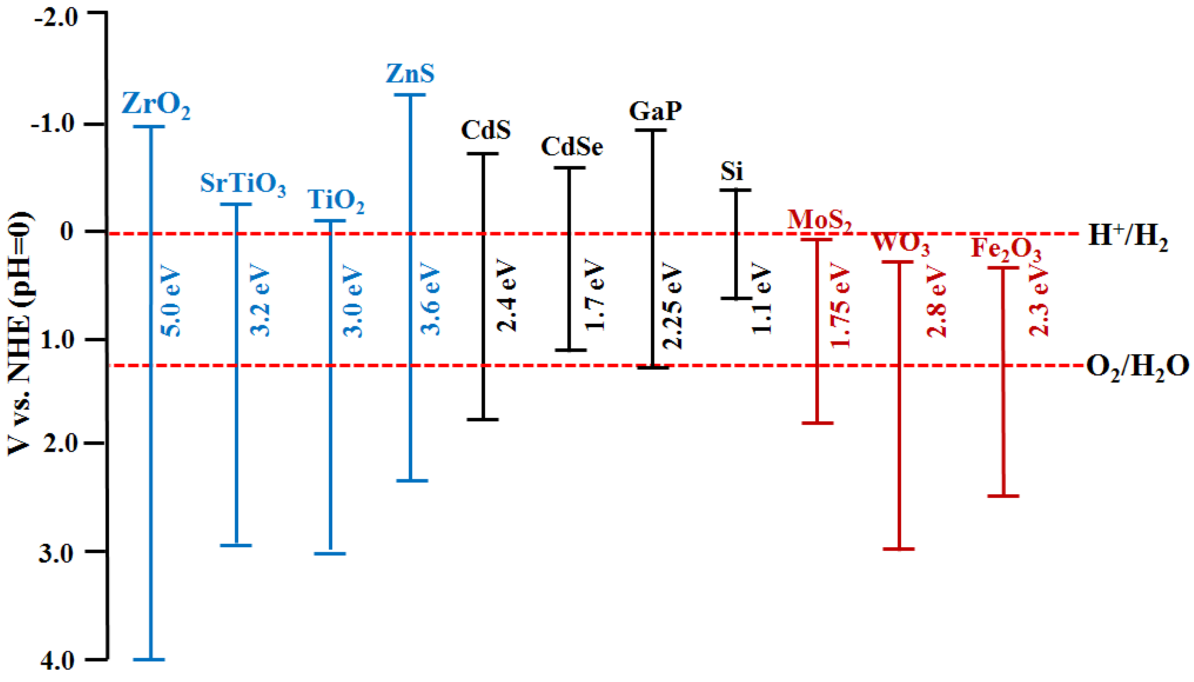

Figure 1.10 Relationship between band structures of semiconductor and redox potentials of water splitting. The bandgap values are from Ref. 67 and 68.

Since H_2 is considered the cleanest energy among various fuels without any carbon emission, in this thesis (Chap. 5), PEC water splitting based on Si is studied. The water splitting reactions taking placed at cathode and anode are described as [69]:

$2H^+ + 2e^- \rightarrow H_2$ (cathode) (e.q. 1.6)

$H_2O \rightarrow \frac{1}{2} O_2 + 2H+ + 2e^-$ (anode) (e.q. 1.7)

The Gibbs free energy change ΔG^0 of the net reactions at room temperature is 237 kJ/mol, which is equivalent to $\Delta E^0 = 1.23$ V according to the Nernst equation. In an ideal case, a semiconductor can absorb most of solar spectrum, and has a band gap energy larger than 1.23 eV [66,69]. The conduction band-edge (E_{CB}) and the valence band-edge (E_{VB}) should straddle the electrochemical potentials of $E^0(H^+/H_2)$ and $E^0(O_2/H_2O)$ [68]. Fig. 1.10 shows the relationship between the band structures of some commonly used semiconductors and the redox potentials of water splitting. Most of semiconductors with large bandgap (e.g. TiO_2, ZnS and $SrTiO_3$) can generate enough photovoltage for water splitting; they can only absorb small portion of sunlight in the UV region. Some semiconductors with moderate bandgap value (e.g. CdSe and CdS) are suitable for water splitting but own poor stability in contact with aqueous acidic or alkaline electrolytes. Si with small bandgap can absorb most of the visible light, and it has relatively nice stability against corrosion in the electrolyte. Its conduction band edge well locates above $E^0(H^+/H_2)$. Therefore, Si would be an ideal material acting as the photocathode for the hydrogen evolution reaction (HER).

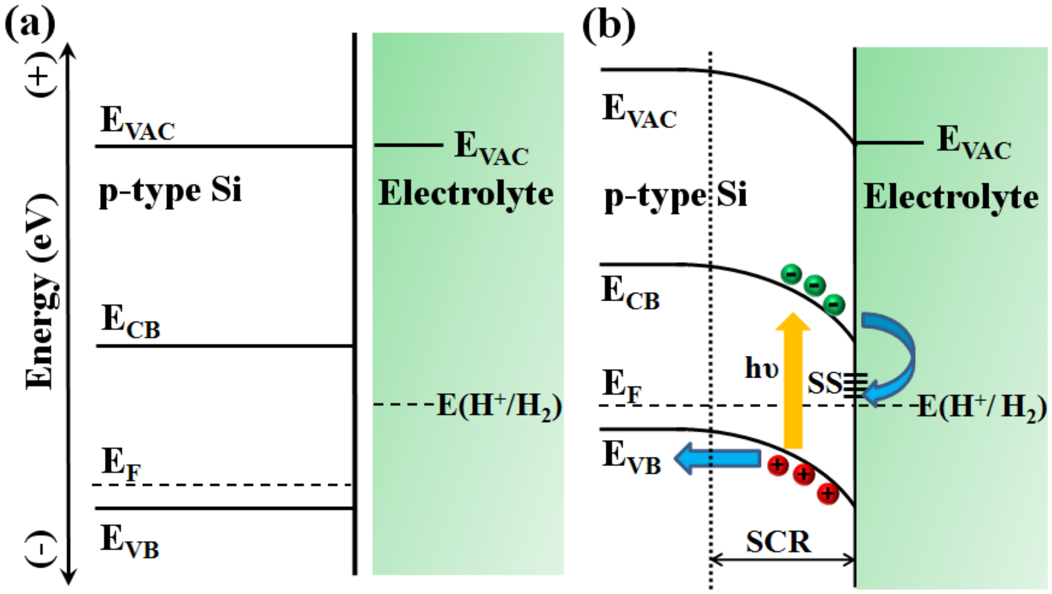

Figure 1.11 Band diagrams of p-type Si before (a) and after (b) contacting with electrolyte. E_{CB} and E_{VB} are the conduction band and the valence band of Si, respectively. E_{VAC} represents the vacuum level. Red circles represent holes. As the Fermi level of Si (E_F) and $E(H^+/H_2)$ equilibrate,

the energy bands of Si bend downwards. A SCR layer is formed, which is capable of separating photon generated electrons (green balls) and holes (red balls). SS represents the surface states.

Fig. 1.11 shows the band diagrams of p-type Si before and after contacting with a liquid electrolyte. After bringing Si into contact with an electrolyte, the Fermi level in both Si and electrolyte must equilibrate ($E_F = E^0(H^+/H_2)$). Since $E^0(H^+/H_2)$ is higher than E_F in p-type Si, the majority carriers (i.e. holes) would flow to the solution phase. Consequently, the resulting excess charge in Si would distribute in a region near the Si surface called space charge region (SCR) [67]. The resulting electric field in the SCR is shown as the downward band bending in Fig. 1.10. At the electrolyte side, an ionic layer on the solution side establishes an electric field double layer (Helmholtz layer and Gouy layer) between Si and electrolyte [70].

The photon generated electrons and holes can be separated due to the electrical field built in the SCR. Electrons would flow the Si cathode surface leading to H_2 formation, meanwhile holes would transport through the anode for O_2 evolution. However, such flow is limited to the existence of surface states in the bandgap shown in **Fig. 1.11**. The surface states are caused by the dangling bonds of surface atoms or surface defects. Without adequate surface passivation (e.g. H termination by HF dipping), these surface states would trap the electrons leading to the strong surface recombination. The surface recombination would become much more severe while increasing the surface roughness by nanostructuring [69, 71, 72]. Investigation of the surface state density in Si nanostructures on the photocurrent would be one of topics in Chap. 5. Since Si cannot generate high enough photovoltage for water splitting, a small overpotential (~-

0.6 V for planar Si) needs to be applied. Through applying nanostructured Si, the overpotetnial can be minimized to ~-0.2 V [67,68], the mechanism behind the lowering overpotential would be also discussed in Chap. 5.

1.4 Summary

In this chapter, we introduce our motivation: applying nanotechnologies to break the current high cost bottleneck of solar energy conversion devices. We propose three basic strategies: (1) Improving the solar conversion efficiency, (2) Utilizing cheap ‘dirty’ UMG-Si or even MG-Si and (3) Reducing the expensive materials use. Strategy (1) and (2) can be realized based on the new radial junction design based on SiNW structure. The new design would orthogonalize the directions of light absorption and charge carrier collection. The enhanced charge carrier collection allows further efficiency improvement of high quality material and the use of low quality UMG-Si or MG-Si without sacrificing much efficiency. The wet chemical NW fabrication method MaCE is also expected to remove the metal impurities inside ‘dirty’ Si. In Chap. 3, we will show the SiNW construction on EG-, SG- UMG- and MG-Si by MaCE. The purification effect induced by MaCE is also confirmed. In Chap. 5, we will investigate the PEC performance of the obtained SiNW to verify the advantages of radial NW-electrolyte junction. Strategy (3) can be achieved by another nanotechnological approach: meso-PSi based layer transfer technique. In Chap. 4, we will demonstrate that similar as ECE, MaCE is also capable of fabricating meso-PSi and flexibly controlling the porosity.

EXPERIMENTAL

2

2.1 Etching Process

2.1.1 SiNW fabrication from different grades of silicon via MaCE

Four different grades of silicon shown in **Fig. 2.1** were used, including, MG-Si pieces and powder (~99.74% pure, from Q-Cells GmbH), UMG-Si (multicrystalline, p-type, 0.2-0.5 Ω cm, 99.999772% pure, from Fraunhofer IWM), SG-Si (multicrystalline, p-type, 1-3 Ω cm, 99.9999% pure, from Fraunhofer IWM) and EG-Si (monocrystalline, (100) orientation, 1-10 Ω.cm, >99.999999% pure, from Si-Mat GmbH).

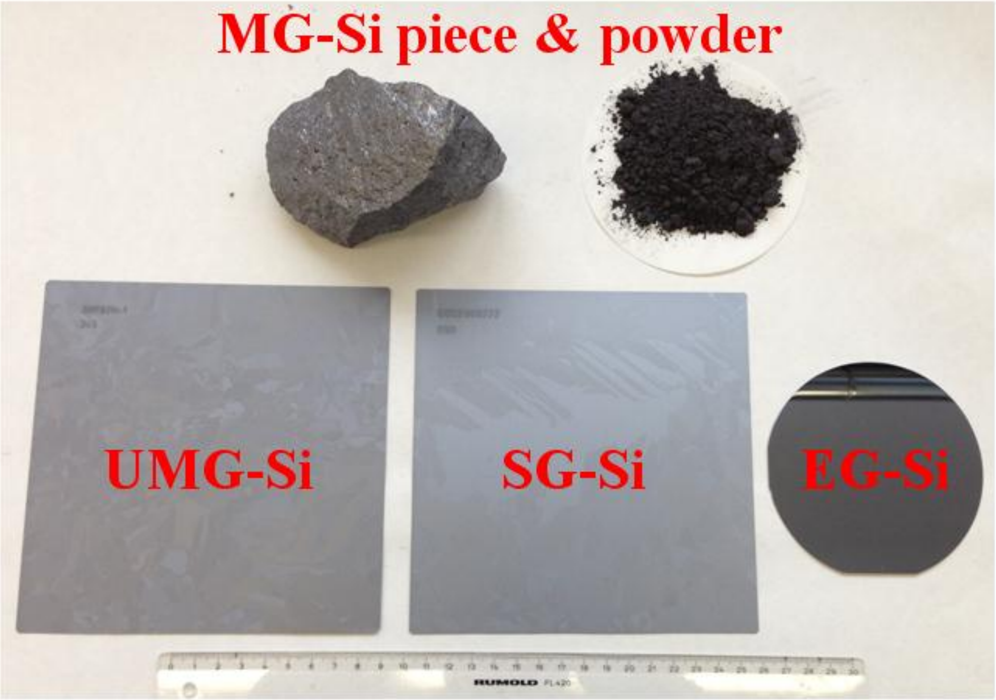

Figure 2.1 Photographs of four different grades of silicon including MG-Si piece and powder, UMG-Si, SG-Si and EG-Si wafers.

Prior to the etching, Si wafers were cleaned in Piranha (98% H_2SO_4/ 30% H_2O_2 = 3:1, (v/v)) for 15 min and afterwards rinsed by DI water. Clean Si wafers were cut into pieces of suitable size and dipped into 5% HF solution for 3 min to remove the native oxide. Subsequently, the MaCE was carried out by immersing Si samples into 5 M HF and 10 mM $AgNO_3$ solution for deposition of Ag nanoparticles (AgNPs) and then etched in an aqueous etchant containing 5 M HF and 0.3 M H_2O_2 shown in **Fig. 2.2**. After etching, the Si samples were rinsed with DI water and dried by N_2 gas blowing. All experiments were performed at room temperature inside a fume hood (~ 20 ^{o}C).

For MG-Si powder etching, 25% ethanol was added to wet the particle surface. After each step of MaCE, the MG-Si powder needed to be filtered and washed with the help of filter papers.

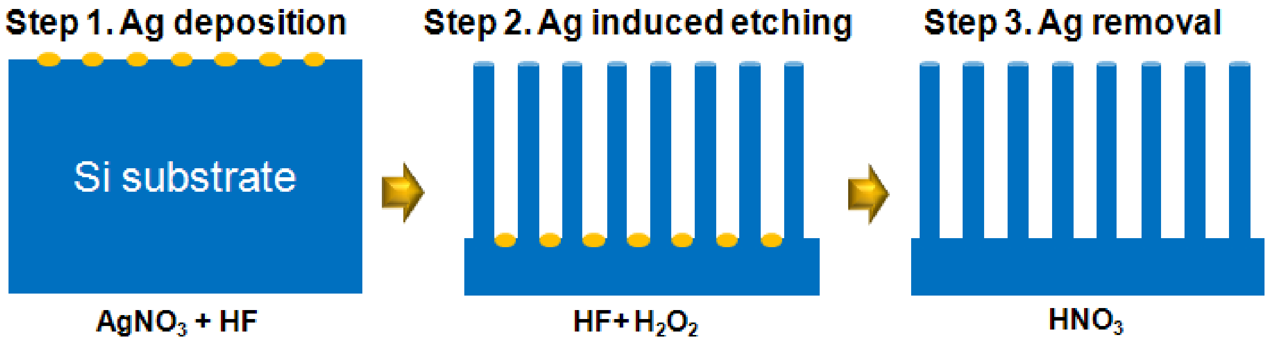

Figure 2.2 Schematic representation of the formation of Si nanowires by MaCE.

2.1.2 Porous Si fabrication via MaCE

To investigate porous Si formation by MaCE, single-crystal EG-Si (100) wafers with two types of resistivity were used: 1-10 Ω cm (p^-, n^-, moderately doped) and 0.01-0.02 Ω cm (p^+, n^+, highly doped). The etching process was the same as SiNW fabrication, except that Pt nanoparticles (PtNPs) were used instead of AgNPs as the catalysts for etching. PtNPs were deposited on the Si surface by immersing the Si samples into a solution containing 0.5 M HF and 1 mM K_2PtCl_6.

2.2 Photoelectrochemical (PEC) measurement

2.2.1 PEC setup

A PEC cell was constructed in a three electrode configuration as shown in **Fig. 2.3**. An Ag/AgCl, KCl (3M) electrode acted as the reference electrode and a platinum mesh was used as the counter electrode. Fig. 2.3(b) shows the design of our silicon photocathode. An Ohmic contact was formed by smearing In-Ga eutectic on the backside of Si sample. Then, the sample was attached to polyvinyl chloride (PVC) holder. At the center of the substrate, there was a small square copper plate with its backside connected with a copper wire. In order to protect the backside electrode from the acidic electrolyte, PDMS or resin was used to encapsulate the backside of the sample. We used a mixture of polydimethylsiloxane PDMS (Sylgard 184, Dow Corning) and PDMS curing agent with a weight ratio (10:1). After uniformly coating the sample backside with the mixture, the sample was placed into the vacuum chamber and baked at 80^{o}C for 12 hrs. The formed PDMS is resistive to the sulfuric acid.

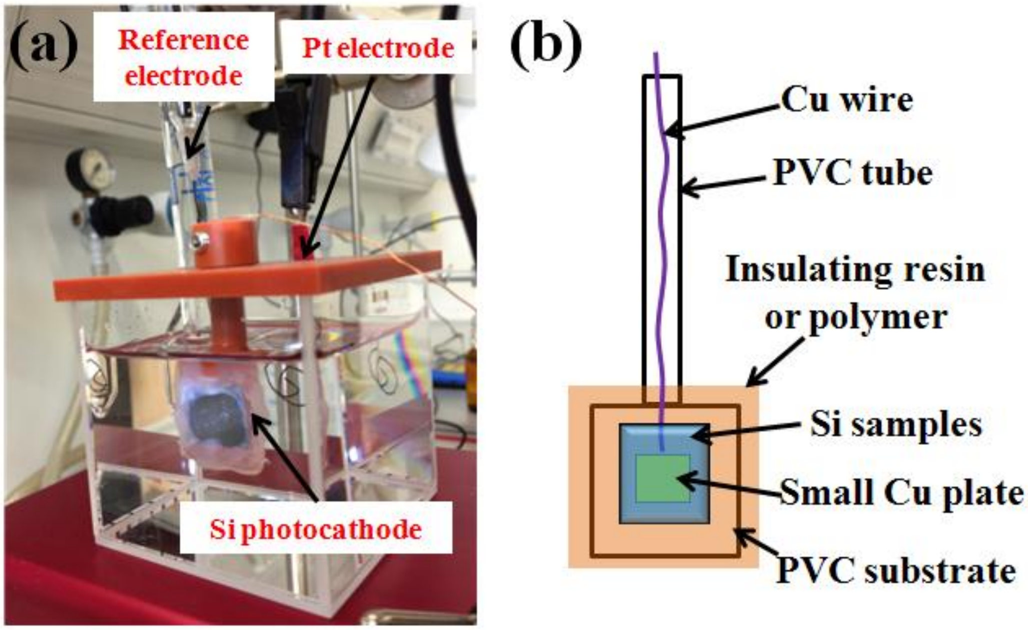

Figure 2.3 (a) Photograph of a PEC cell consisting of a quartz cell, a Si photocathode at the front side, a reference electrode, and a Pt counter electrode at the backside. (b) Schematic design of the photocathode with a Si sample attached to a PVC substrate.

The light source is critically important for PEC measurements. It should have stable intensity, and a similar spectrum as the natural sunlight. A Xenon lamp (50 - 200 W Research Arc Lamp, Newport Corporation) was used to simulate the sun light. **Fig. 2.4** shows its spectrum. Since its intensity is too high intensity in the range of 800 to 1100 nm, a glass filter (FSR-KG2, Schott GmbH) was added to shape the lamp spectrum. The light intensity could be flexibly tuned by changing the applied current of the lamp. To get the light focused on the Si samples with a small circle area about 0.4cm^2, an iris and a lens were used. **Fig. 2.5** shows the optical setup. For the data shown in Section 4.1, the light intensity was around 200 W/cm^2. Since the standard AM 1.5

light source was purchased later, the light intensity was changed to 952 W/cm^2. The obtained PEC data was shown in Section 4.2.

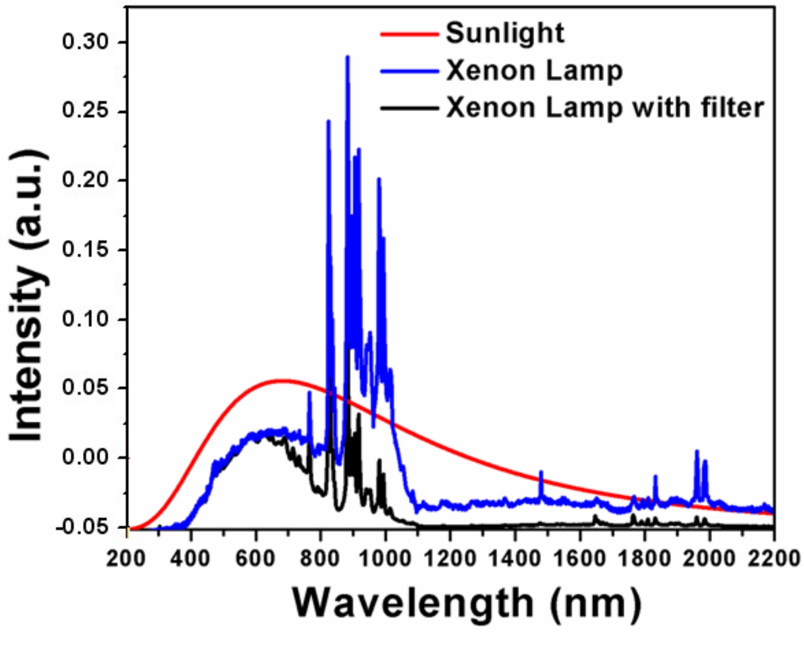

Figure 2.4 The spectrum of the Xenon lamp before (blue) and after (black) using an optical filter. The red curve represents the rough spectrum of sunlight.

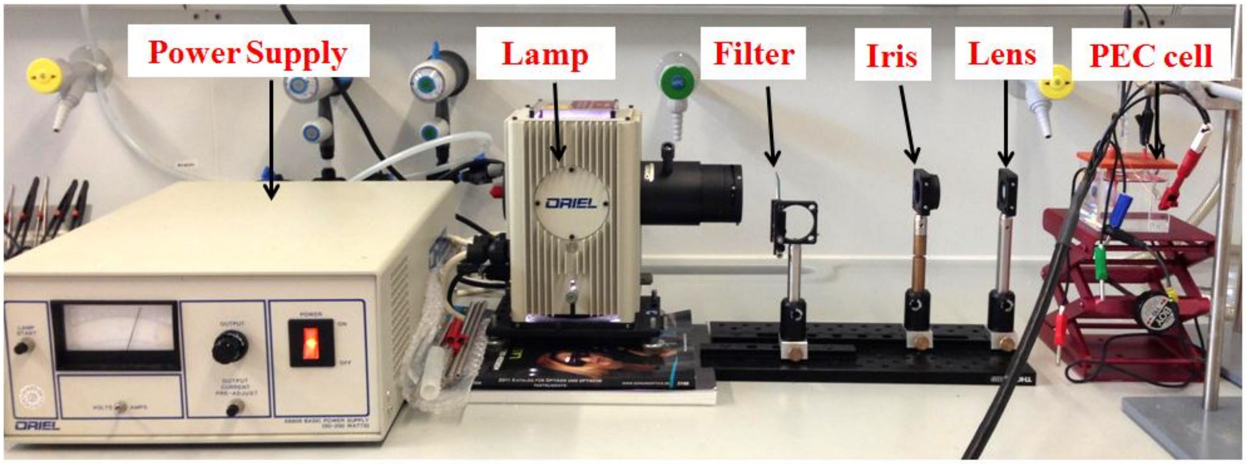

Figure 2.5 Optical setup for the PEC consisting of a power supply, a lamp, a light filter, an iris, a lens and a PEC cell (from left to right).

2.2.2 PEC characterization

The PEC J-V curves were ramped from – 1.6 V to 0.2 V (vs. Ag/AgCl reference electrode) at a rate of 50 mV/s. The photoelectrode stability tests were done by switching on-off light source every 20 s.

2.3 Characterization and other measurements

2.3.1 Scanning electron microscopy (SEM)

Si nanostructures were characterized by SEM (JEOL 6700F). In order to cut the MG-Si particles, plasma focused ion beam (TESCAN USA) was used.

2.3.2 High resolution transmission electron microscopy (HRTEM)

For TEM characterization, SiNWs were sonicated from the substrate, and dispersed in an ethanol solution (see in **Fig. 2.6**). A gold TEM grid was dipped into the NW solution and dried in air. HRTEM images were obtained by JEOL 4010.

For MG-SiNW, TEM images were obtained by FEI Titan G2 60-300 scanning transmission electron microscopes (STEM) with Cs-correction, the EDX spectrum and mapping was done by Super-X EDX (installed in STEM), the counting time was 1 hr for one nanowire.

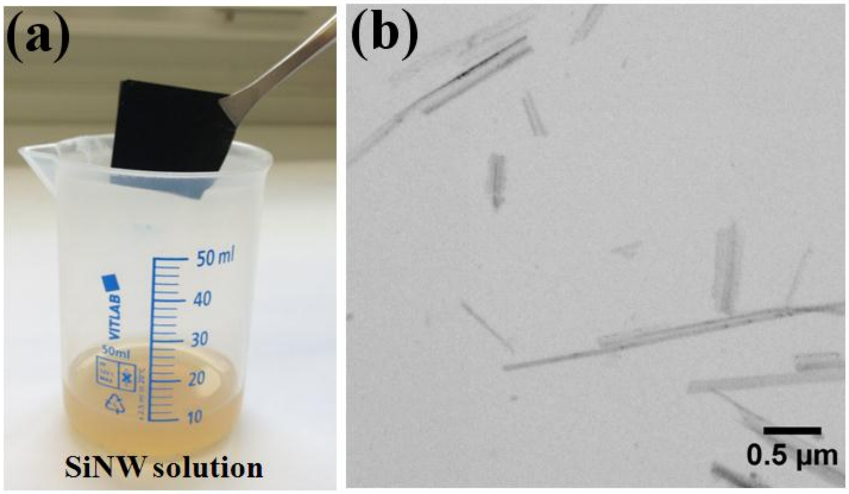

Figure 2.6 (a) Yellow SiNW ethanol solution formed by sonicating NW structured Si substrates, (b) TEM images of SiNWs dispersed on the TEM grid.

2.3.3 Inductively coupled plasma mass spectrometry (ICP-MS) and inductively coupled plasma optical emission spectrometry (ICP-OES)

The ICP-MS and ICP-OES analysis were performed using Element XR and iCAP 6500 (Thermo Scientific) instruments respectively. The calibration was done with commercial multi element standard solutions. Since ICP-MS is very sensitive to the impurities, the experiments need to be carried out very carefully to avoid any possible environmental contamination. The UMG-Si wafers were firstly cleaned by piranha solution, and then etched for several hours in such a way that 50-60% of the wafer thickness was converted to nanowires. The etched wafer was immersed in fresh HNO_3 (68%) and rinsed by DI water for 3 hours, and such a HNO_3 process was repeated for 3 times to ensure complete removal of Ag catalysts. The etched wafer was again cleaned by piranha to remove all the possible contaminations induced during chemical etching.

After drying the samples in a flow box (clean room conditions) the etched and non-etched wafers were completely dissolved with HF/HNO_3 and evaporated to almost dryness. Prior to ICP-MS analysis the samples were diluted with a 2% HNO_3 solution. A thorough background determination was performed by analysing multiple control samples without silicon. Based on the variation between control samples, the limit of detection (LOD) was determined for each element.

Element analysis of MG-Si powder by ICP-OES followed similar operations as ICP-MS. Due to the high reactivity of MG-Si powder, HF/HNO_3 dissolution needs to be carefully controlled to avoid very rapid reactions.

2.3.4 Reflectance measurement

The measurements were conducted in LAMBDA 750 UV/Vis/NIR Spectrophotometer (*Perkin-Elmer Inc.*).

2.3.5 Quasi steady state photoconductivity (QSSPC) measurements

The carrier lifetime measurements were performed by the quasi steady state photoconductance (QSSPC) measurements (*Sinton Instruments WCT-120*).

2.3.6 Electrochemical measurement: Open circuit potential (OCP), short circuit current

In order to obtain stable OCP, short circuit current and impedance data of silicon samples, an electrochemical cell was constructed shown in **Fig. 2.7**(a,b). It consists of several parts including a Cu plate and a Teflon cell with a hole with diameter ~1.5 cm at the bottom, an O-ring for sealing, an iron hoop and several screws. In-Ga eutectic was smeared at the backside of a Si sample to form an Ohmic contact with Cu. Fig. 2.7(c,d) shows the whole setup. The working electrode of the IVIUM potentiostat was connected with Cu plate, the counter electrode was connected with a Pt wire.

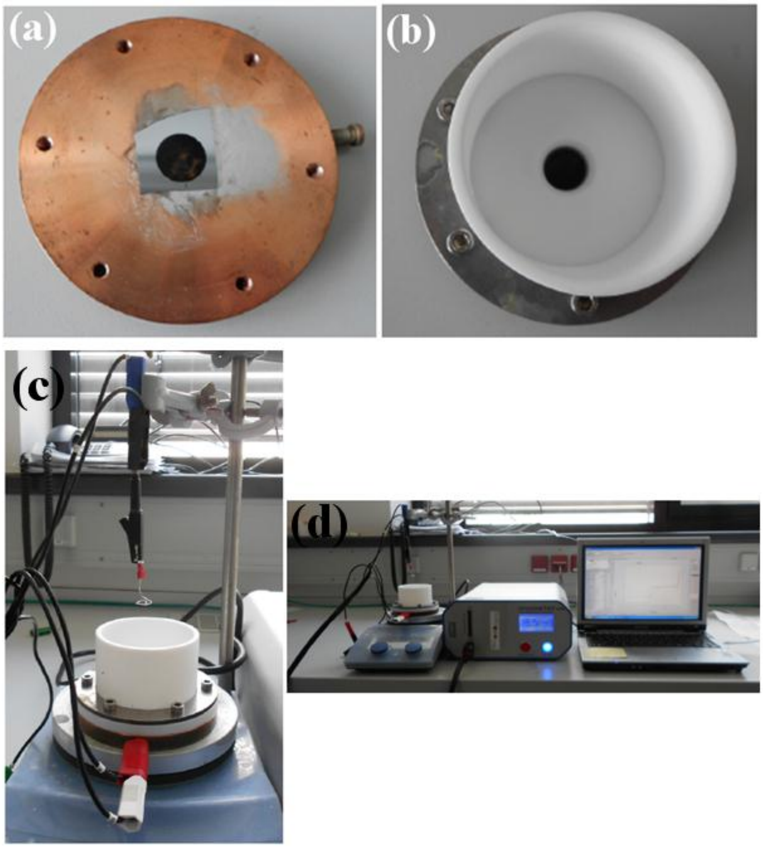

Figure 2.7 (a) A Cu plate with a Si sample. The white metal is In-Ga eutectic. (b) Top view of a sealed electrochemical cell. (c, d) Photograph of the whole setup consisting of an electrochemical cell, an IVIUM pontentiostat and a computer for data recording.

Part II

THE RESULTS

3

Si NANOWIRE (SiNW) FABRICATED BY MaCE

In this chapter, we focus on the fabrication of SiNWs from different grades of Si including EG-, SG-, UMG- and MG-Si by MaCE and the etching mechanism behind it. In Section 3.1, we firstly show the production of SiNWs on a wafer scale. Afterwards, SiNWs etched from ‘dirty’ silicon (UMG- and MG-Si) are demonstrated in Section 3.2. Interestingly, for the first time, we find the existence of line defects in some UMG-SiNWs, and uniform porosity development in MG-SiNWs. Furthermore, through element analysis, we confirm that the metal impurities in Si are removed, and the ‘dirty’ silicon (UMG- and MG-Si) can be upgraded close to solar grade.

In Section 3.3, we discuss the etching mechanism in detail. A new chemical etching model is proposed to explain the removal of metal impurities and the porosity formation in SiNWs during etching of MG-Si.

3.1 SiNW etched from EG-Si and SG-Si

3.1.1 SiNW fabrication from EG-Si

Previously lots of literature reported on the synthesis of SiNW from EG-Si, here we followed the 2-step MaCE process developed by Peng et al. [32]: (1) AgNP deposition in 5 M HF + 10 mM $AgNO_3$, (2) Etching in 5 M HF + 0.3 M H_2O_2. **Fig. 3.1** shows the influence of AgNP coverage on the formation of SiNW from polished p-type Si (1-10 Ω cm) through varying the Ag deposition time. Short deposition time (< 1min) leads to the formation of macroporous Si instead of NWs. Excessive deposition time (> 1min) causes extra dissolution of SiNWs. Thus, we fixed the Ag deposition time at 1 min for all polished Si wafers.

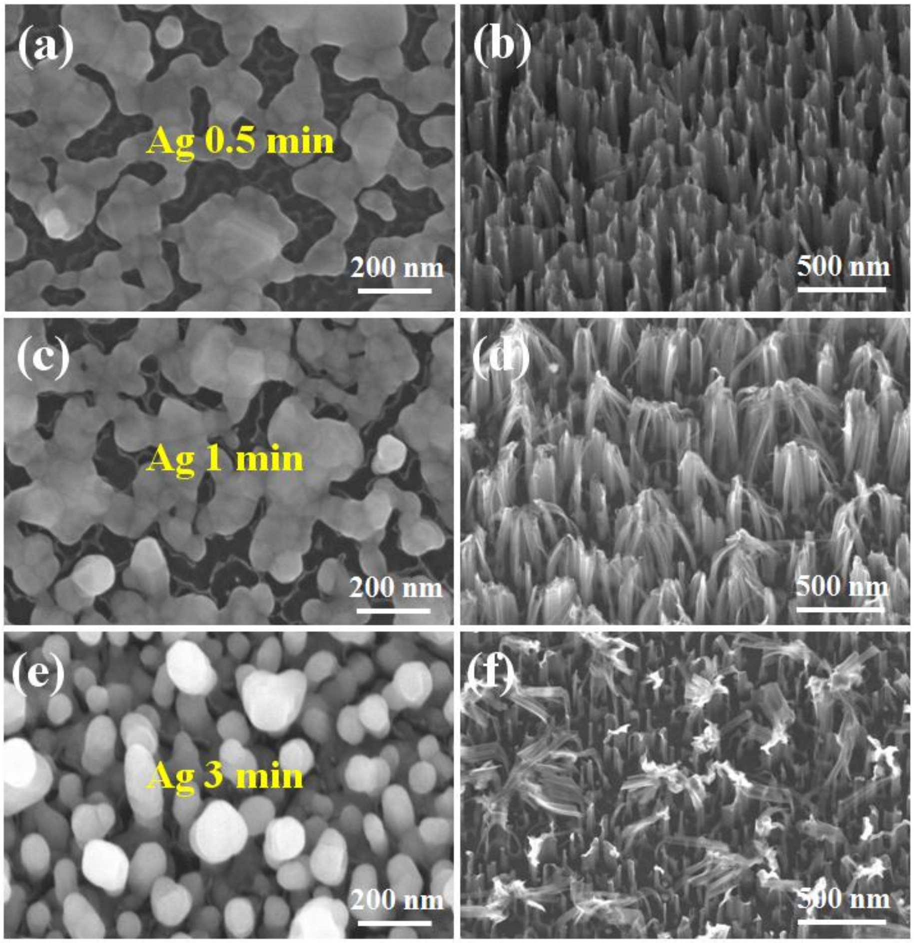

Figure 3.1 SEM images of AgNPs deposited on the polished EG-Si (1-10 Ω cm) surface with different deposition times (a) 0.5 min, (c) 1min and (e) 3min; (b, d, f) are the tilt SEM images of the corresponding Si structures formed after etching in 5 M HF + 0.3 M H_2O_2 for 5 min.

Through measuring the cross-section SEM, we obtained the linear relationship between SiNW length and etching time (see **Fig. 3.2**). The growth rate of SiNW is nearly constant (~0.3

μm/min). The bulk diffusion would not limit the etching if there is enough amount of etchant. Si wafers (~500 μm) can be even etched through by prolonging the etching time.

Fig. 3.3(a) shows the polished EG-Si wafer before and after etching. The etching was very uniform and turned Si surface into totally black. The diameter of SiNWs ranges from 50 to 200 nm seen in Fig. 3.3(b,c). The effect of the doping level of Si substrates on the morphology of SiNWs was also studied. With the increasing of doping level, there were more tiny pores formed at the side walls of SiNWs (see **Fig. 3.4**(a,b), p^+-type Si). For the p^{++}-type Si, SiNWs became totally porous (see Fig. 3.4(c)), agreeing with previous report [73].

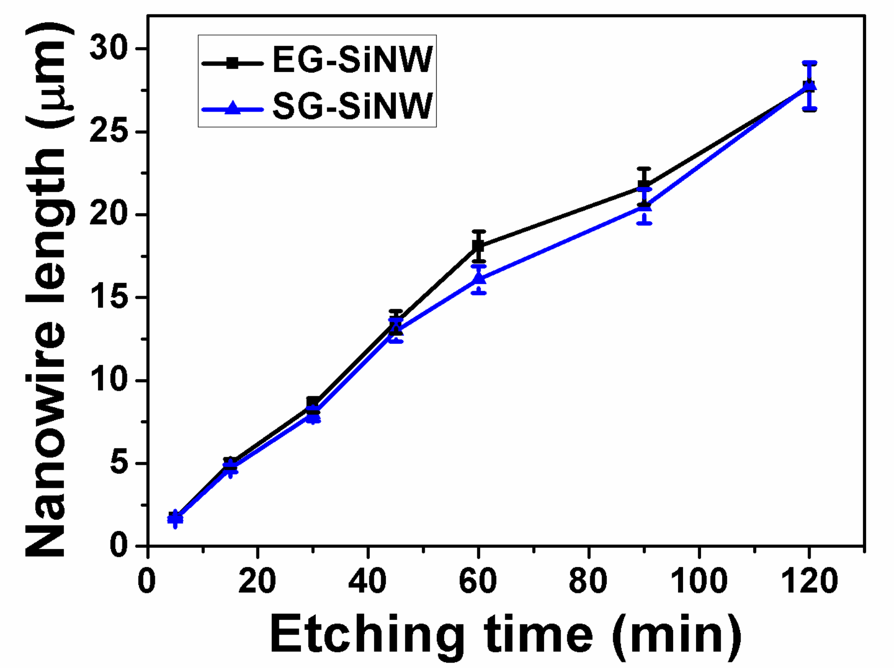

Figure 3.2 Dependence of the etching time on the length of EG-SiNW (black square) and SG-NW (blue triangular). The etching was conducted in 5 M + 0.3 M H_2O_2 solution at room temperature.

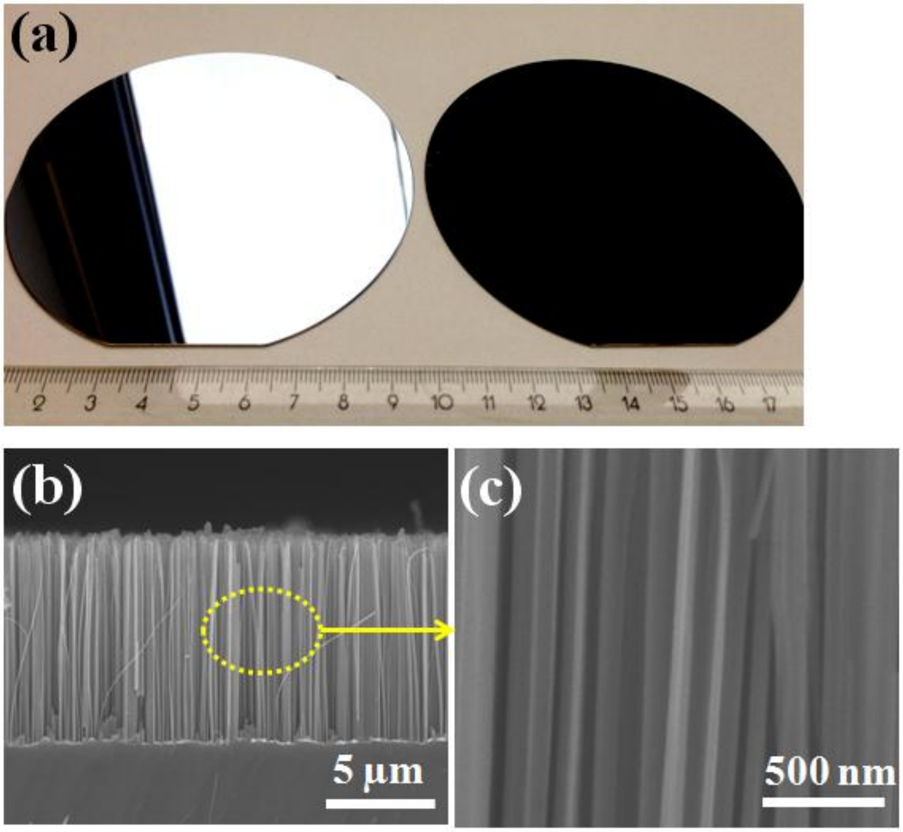

Figure 3.3 (a) Photograph of p-type polished EG-Si(100) wafer (1-10 Ω cm) before and after SiNW texturing. (b) Cross-sectional SEM images of SiNWs. (c) is the magnified view of (b).

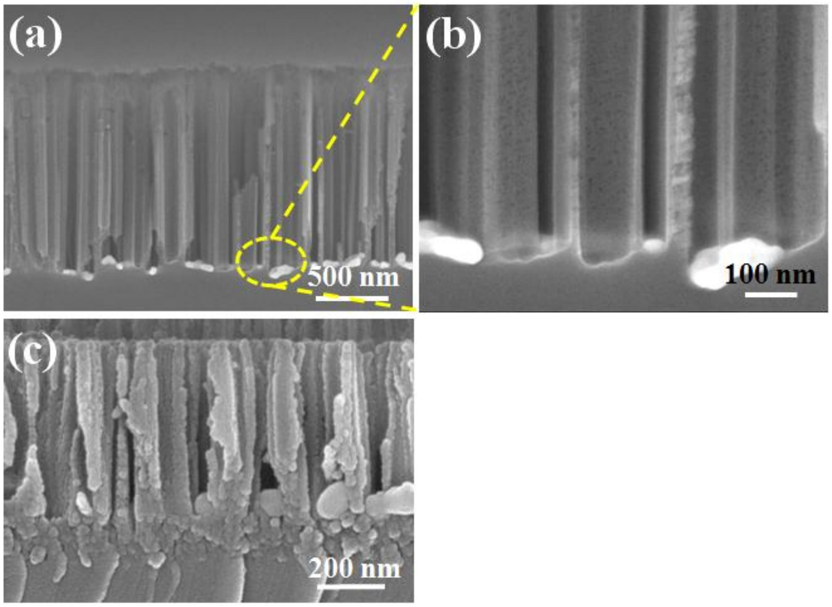

Figure 3.4 Cross-sectional SEM images of silicon nanowire (SiNW) etched from (a) p^+-type Si (0.01-0.02 Ω cm), (c) p^{++}-type Si (0.001-0.002 Ω cm). (b) is the magnified view of (a).

3.1.2 SiNW fabrication from SG-Si

The as-cut multicrystalline SG-Si wafers were sliced by laser and the wafer surfaces were covered with cut-injured regions. **Fig. 3.5**(a) shows the SEM image of AgNPs on the SG-Si surface, more AgNPs were deposited than those on the EG-Si surface. Since there were lots of surface states, defects, and dislocations on the SG-Si surface, the nucleation of AgNPs preferentially occurred at these defect sites, where the energetic barrier was lowered and electrons can easily tunnel through it.

Fig. 3.5(b-d) shows the SEM images of SiNWs formed on a SG-Si wafer. Compared with MaCE of the polished EG-Si wafer (see Fig. 3.1), the reaction of SG-Si was more complex. At first, much more hydrogen bubbles were generated than during the etching of EG-Si indicating a high silicon dissolution speed. Within a few minutes, morphological defects developed by wafer sawing were removed, due to excessive Ag deposition. SiNWs of good crystallinity were formed as shown in Fig. 3.5(c-d). For the SG-Si with different crystallographic grains, SiNWs in different grains were slanted in different angles (see in Fig. 3.5(b)) but the etching directions generally followed the <100> direction.

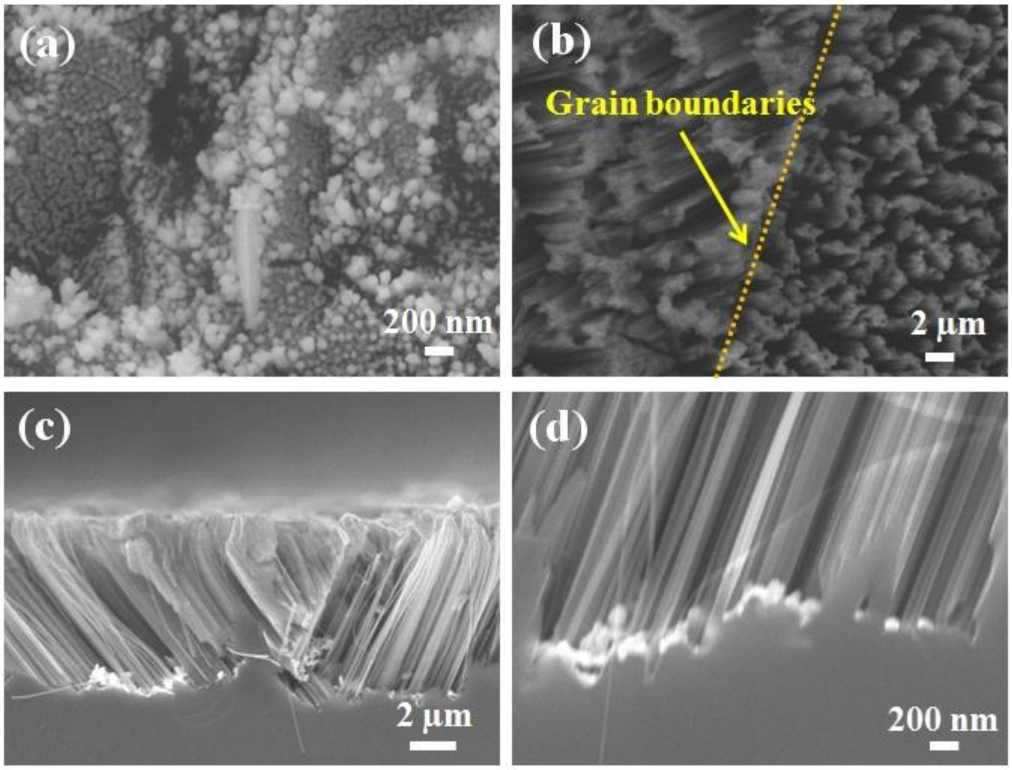

Figure 3.5 Top-view SEM images of (a) AgNPs deposited on SG-Si surface, (b) SiNWs formed on SG-Si surface, (c, d) Cross-sectional SEM images of SiNWs at low and high magnifications.

3.1.3 SiNW array fabrication from SG-Si

Since the shape of the metal film determines the position and size of the remaining Si structures after etching, the controlled fabrication of SiNW array can be realized by using lithography to define the metal mesh on Si surface. However, traditional lithography techniques including photolithography and e-beam lithography are cost-ineffective, and the Si surface needs to be smooth enough for photoresist coating.

Here, we use the nanosphere lithography for patterning of the metal mesh. The low-cost polystyrene beads are self-assembled as a close-packed monolayer at the Si surface serving as the mask for metal deposition. **Fig. 3.6** illustrates the scheme for fabricating size-tunable SiNWs. The as-cut SG-Si wafer was firstly polished in 30 wt% KOH solution at 80 ^{o}C for 3 min. In the second step, PS beads were coated at the SG-Si surface. After O_2 plasma etching, the size of the PS beads was further reduced. Afterwards, an Ag layer with thickness ~20 nm was deposited by thermal evaporation. A silicon nanowire array can be obtained by the subsequent MaCE process.

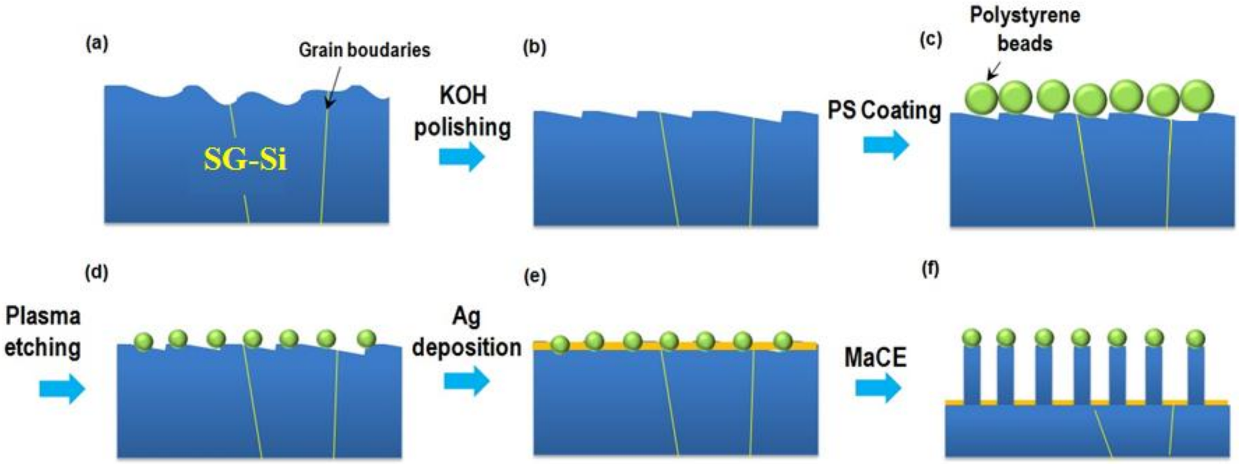

Figure 3.6 Fabrication scheme for a SiNW array combing nanosphere lithography and MaCE.

Fig. 3.7(a,b) show the SEM images of PS beads coated on SG-Si surface before and after plasma etching. Even though the SG-Si surface was rough after KOH polishing, PS beads can be uniformly deposited. The bead size was reduced by 20% after plasma etching. Fig. 3.7(c,d) show the SEM images of the obtained SiNW array after MaCE. It is worth noting that the size of SiNW is ~700 nm, which is bigger than the reduced PS bead size (~200 nm). Moreover, the surface of SiNW was porous. The main reason of this phenomenon is that the Ag mesh was slowly dissolved in the HF and H_2O_2 solution, and the SiNW growth cannot be confined into the patterned area. The dissolved Ag ions would be redeposited leading to the formation of the porous layer at the NW surface. We used 1 wt% KOH solution to remove this porous layer, and solid NWs can be obtained shown in Fig. 3.7(e).

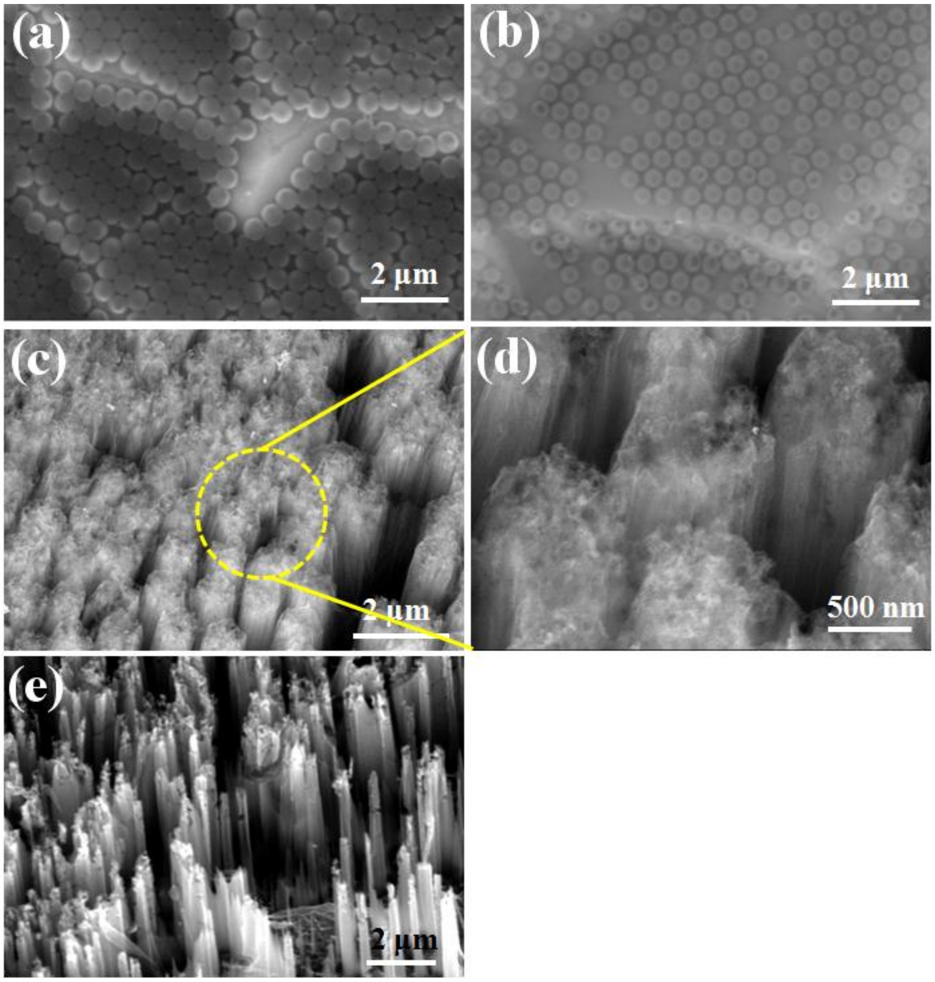

Figure 3.7 Top-view SEM images of (a) PS spheres coated on SG-Si surface polished by KOH solution, (b) PS spheres with reduced size after plasma etching. (c, d) Tilt-view SEM images of MG-SiNW array formed after MaCE at low and high magnification. (e) Tilt-view SEM images of MG-Si array after post KOH etching treatment.

3.2 SiNW etched from UMG-Si and MG-Si

Fig. 3.8 shows the schematic diagrams for the UMG-SiNW and MG-SiNW synthesis by MaCE. Similar as the NW formation in EG-Si, AgNPs drill nanopores deep into UMG-Si and MG-Si, and SiNWs are formed due to merging to adjacent pores. Simultaneously, we expect that metal impurities such as their precipitates or silicides [74] are dissolved upon exposure to the acidic etchant solution. Consequently, SiNWs are purified and local defects or tiny pores would form at NW surface as a result of the impurity removal.

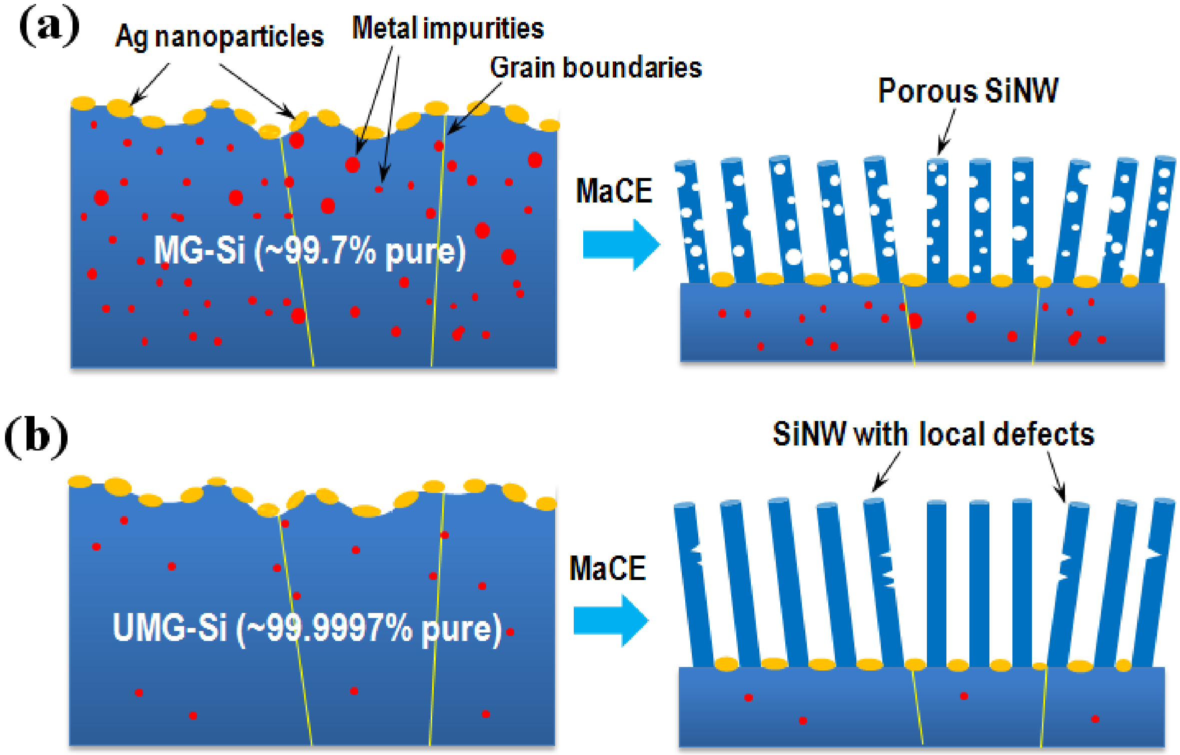

Figure 3.8 Schematic representation of the fabrication process of purified SiNWs from ‘dirty’ silicon via metal assisted chemical etching (MaCE): (a) MG-Si, (b) UMG-Si.

Fig. 3.9(a-d) show the SEM images of the deposited AgNPs and SiNWs formed after MaCE. The reaction of as-cut UMG-Si was same as of SG-Si described in Section 3.1.2. The UMG-SiNWs were also slanted in different angles at different crystallographic grains. The HRTEM image (see Fig. **3.10**(d)) reveals the nice crystallinity. Interestingly, we found there were local etching defects in some UMG-SiNWs confirmed both by SEM and HRTEM images (Fig. 3.9(c,d) and Fig. 3.10(a-b). Such local defects cannot be observed in EG- and SG-SiNWs.

To confirm the reduced impurity level inside the UMG-Si after etching, we used inductively coupled plasma mass spectrometry (ICP-MS) element analysis, which is capable of tracing multi-elements, at the part per trillion levels. The impurity level of a ~50% etched wafer was compared with that of non-etched wafer as shown in **Fig. 3.11**. After MaCE, transitional metals all met reduced levels: Cr (92.6% reduction), Fe (74.3%), Ni (77.6%), Co (78.8%), Mo (79.6%), Cu (17.7%), and Ag (90.6%). The dopant levels such as B, P, and As were not changed, validating the high accuracy of our measurements. UMG-Si was thus upgraded from 99.999772 to 99.999899% in purity.

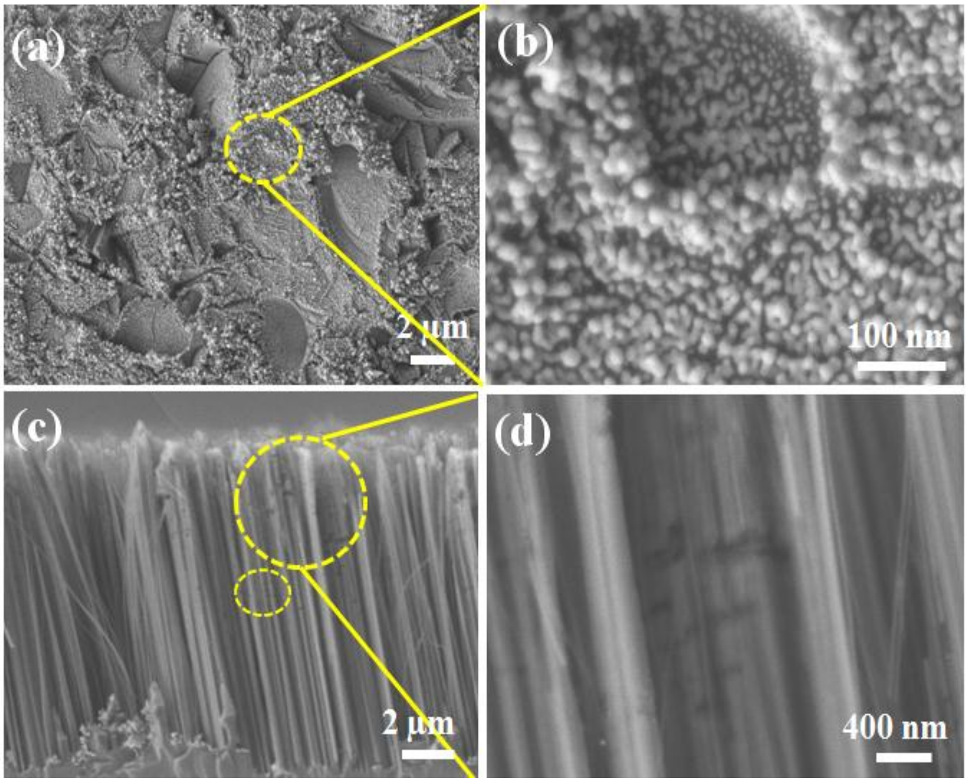

Figure 3.9 (a, b) Top-view SEM images of AgNPs deposited on UMG-Si surface. (c, d) Cross-sectional SEM images of SiNWs etched from UMG-Si.

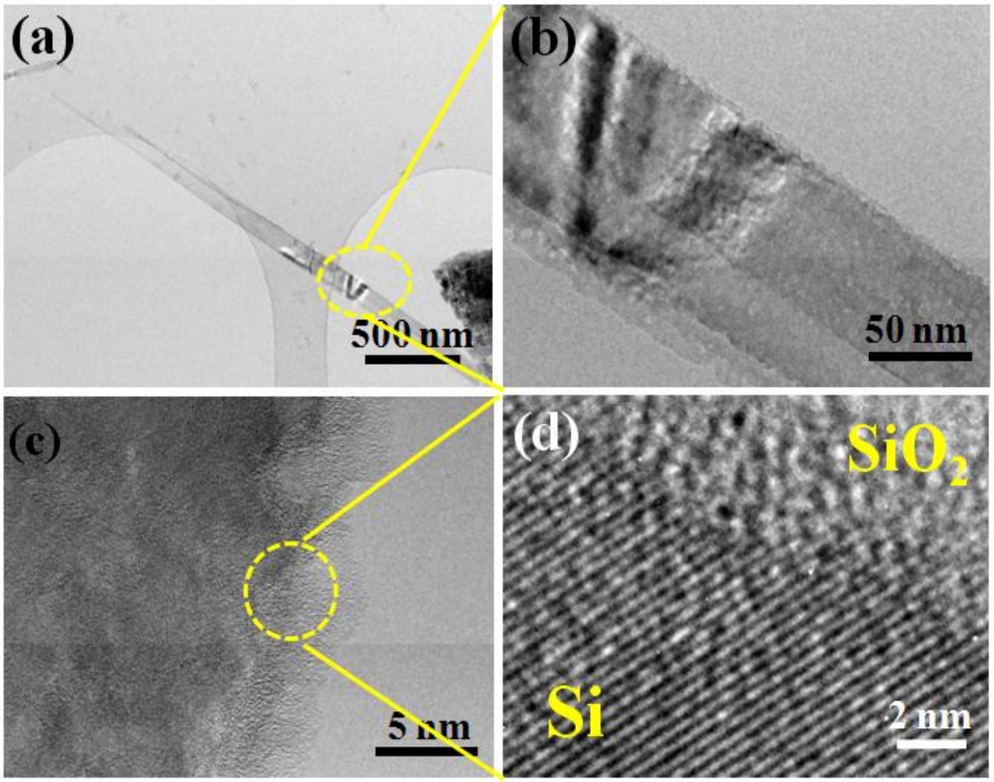

Figure 3.10 TEM images of UMG-SiNWs sonicated from the substrate at different magnification. Two dark lines shown in the (a, b) are defects caused by local etching. There is a line in the middle of SiNW showing two neighboring NWs are sticking together. (c, d) show the high resolution TEM images of the SiNW sidewall.

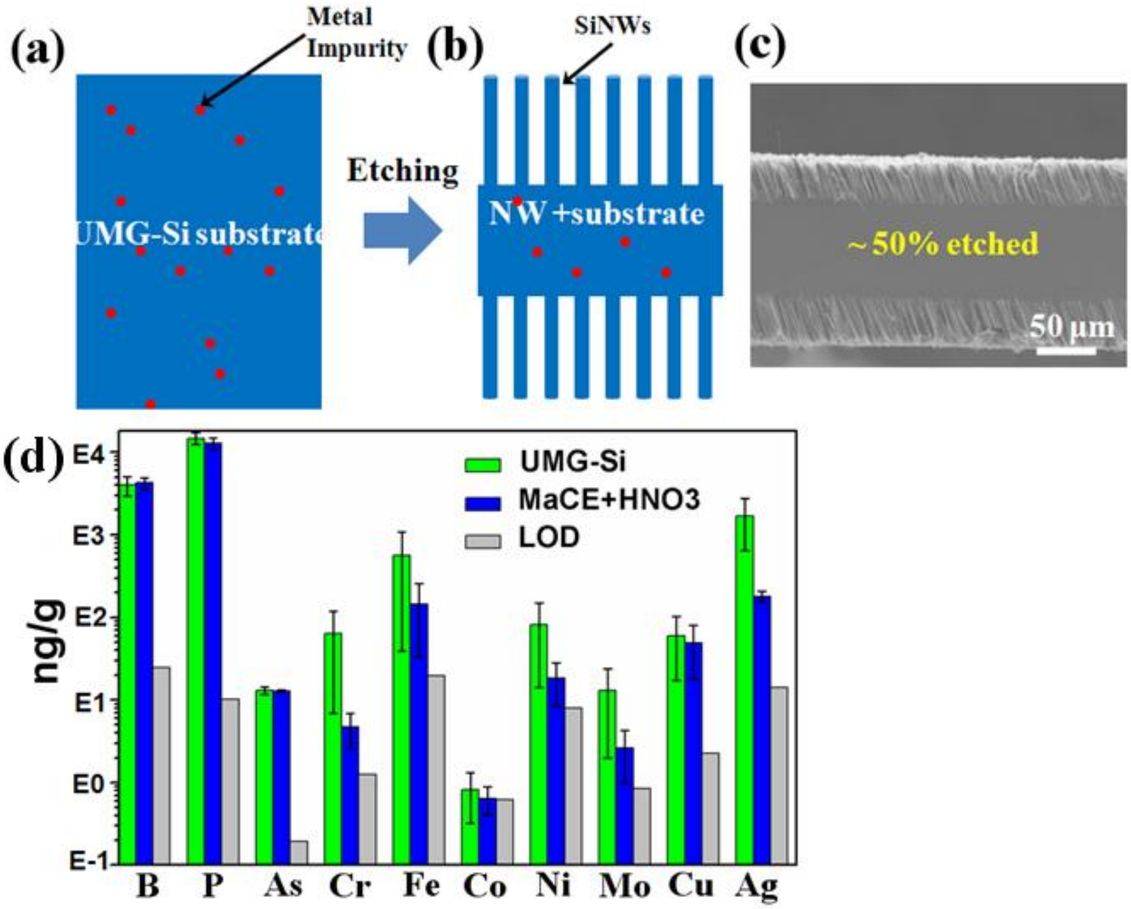

Figure 3.11 (a, b) Schematics of the non-etched and the etched UMG-Si wafers. Red dots are metal impurities. (c) SEM picture of ~50% etched wafer. (d) Impurity concentrations of the non-etched (green), and etched 'dirty' silicon wafer (blue). The grey bar represents the limit of detection (LOD): all elements are above this value. The error bars show the standard deviation between the multiple determinations.

The formation of MG-SiNWs is more complicated than that of EG- or UMG-Si. There are two kinds of MG-Si including blocks and powder. Because small MG-Si pieces were directly cracked from MG-Si blocks by mechanical forces, the surfaces were very rough and full of morphological defects. Since there would be much more Ag deposition at morphological defects than other areas (see Fig. 3.12 (b), big Ag dendrites were formed), the Ag deposition time was extended to 5 min for ensuring full coverage of the MG-Si surfaces.

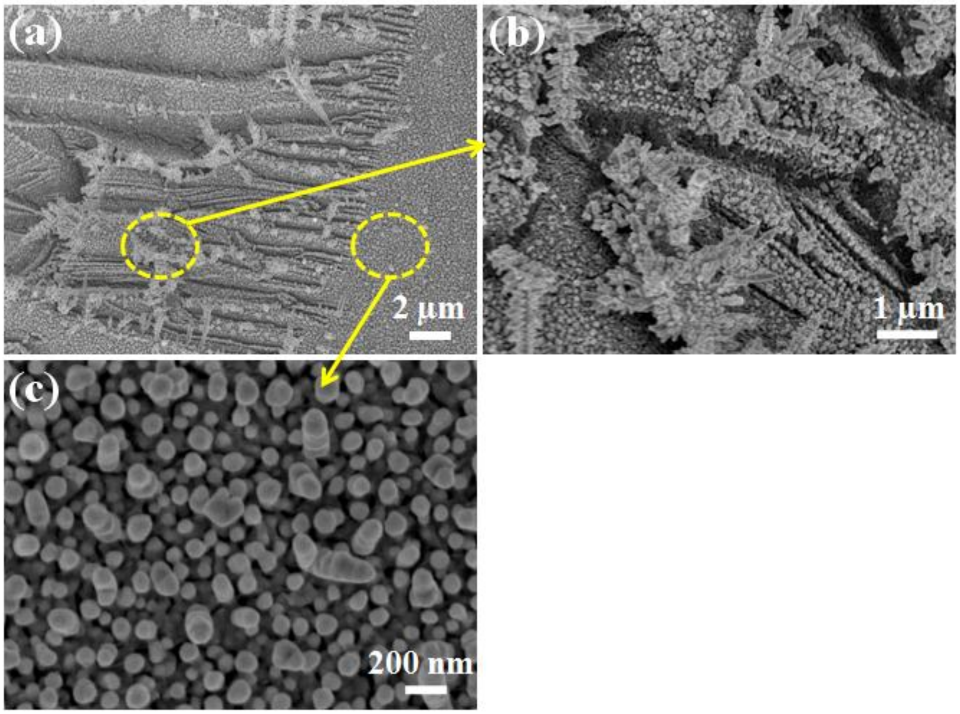

Figure 3.12 Top view SEM images of AgNPs deposited on MG-Si. (b) and (c) are the magnified views of different areas in (a).

Fig. 3.13 shows the top and cross-sectional view of SEM images of the etched MG-SiNWs. Due to much higher amount of metal impurities compared to UMG-Si, SiNWs etched from MG-Si had not only etching pits on their surfaces but became entirely porous. At different areas in MG-Si pieces, the porosity and the length of MG-SiNWs were also different shown in Fig. 3.13(a-d). The growth speed of MG-SiNWs (<0.1 μm/min) was much slower than those of EG- and UMG-SiNWs (~0.3 μm/min). The porosity difference of MG-SiNWs was also confirmed by TEM images (see **Fig. 3.14**). In each MG-SiNW the porosity was uniform with a pore size of 8-20 nm. The etched MG-SiNWs well preserved the crystallinity from their mother substrates. The HRTEM images shown in Fig. 3.14(b, d) show the crystalline phase in between pores.

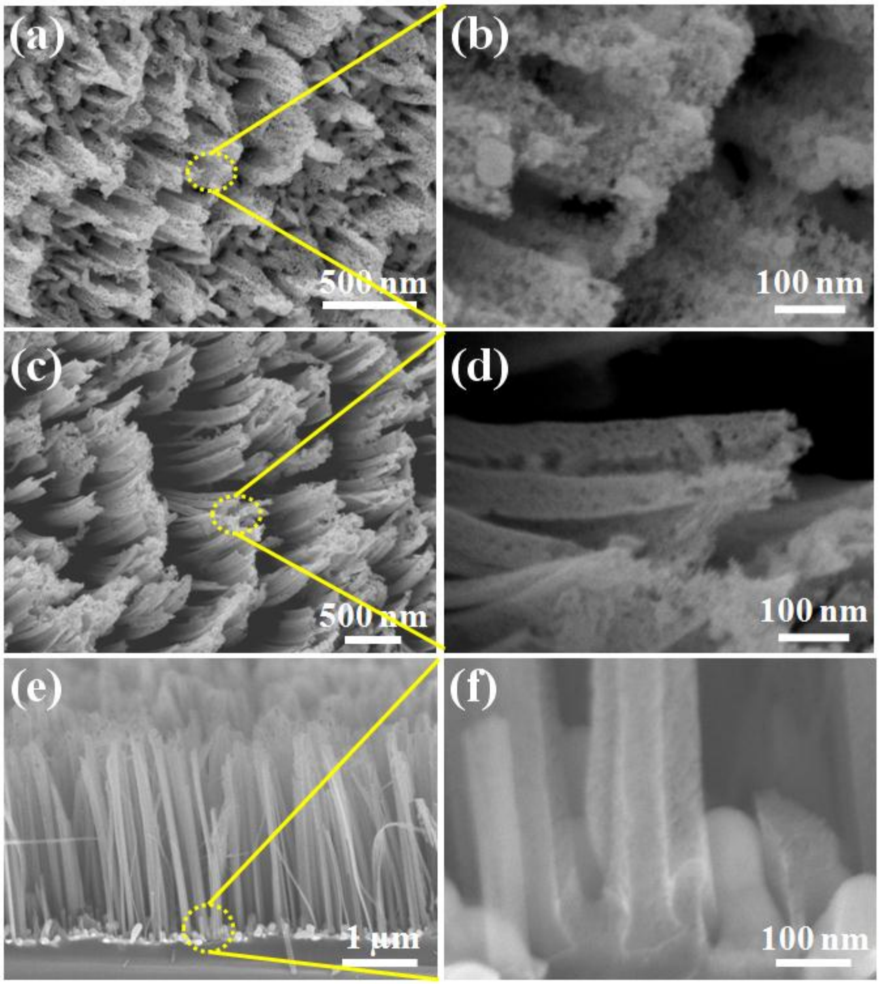

Figure 3.13 SEM images of MG-SiNWs at different areas with different magnifications. (a-d) Tilted-view of SiNWs etched from MG-Si. (e, f) Cross-sectional view of SiNWs etched from MG-Si. (b), (d) and (f) are the magnified view of (a), (c) and (e), respectively.

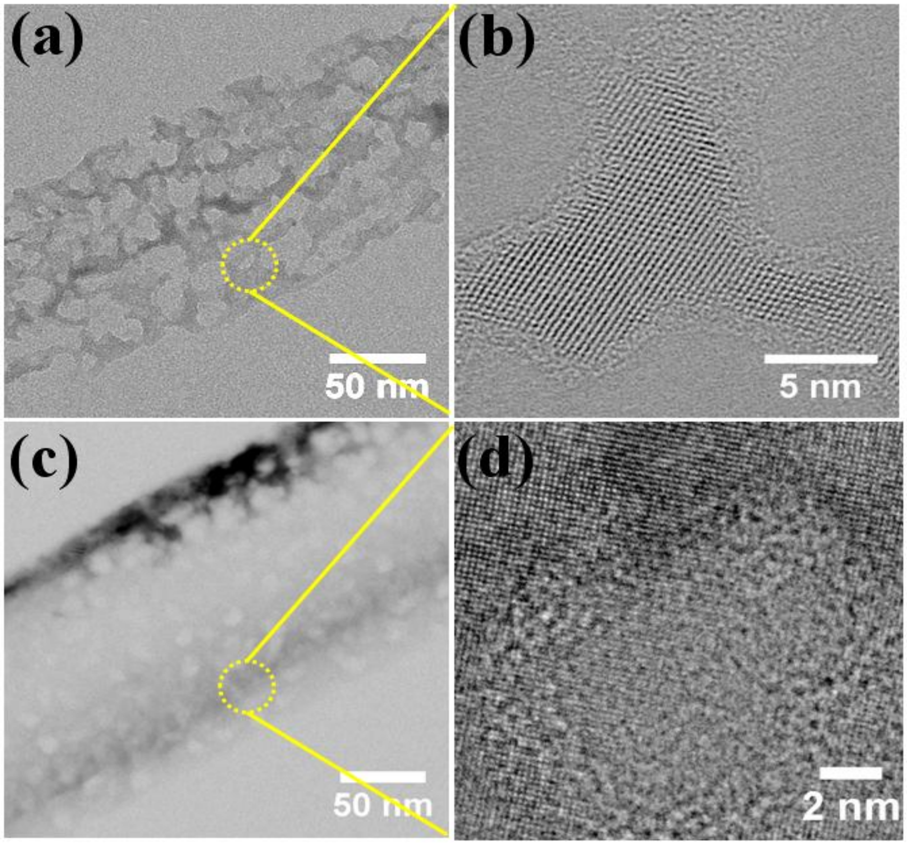

Figure 3.14 TEM images of porous SiNWs with high (a) and low (c) porosity etched from MG-Si (MaCE followed by HNO_3 treatment). (b) and (d) are the magnified view of (a) and (c), respectively.

To verify that the metal impurities have been removed and MG-SiNWs are clean, we firstly conducted the EDX analysis. The Super-X EDX (from FEI) spectrum of MG-SiNWs (detection limit ~0.1%, **Fig. 3.15**(b)) shows no metal impurities in MG-SiNW, and the EDX mapping of different metal impurities only exhibited the background signals (see Fig. 3.15(c-g)), again confirming that MG-SiNWs were purified.

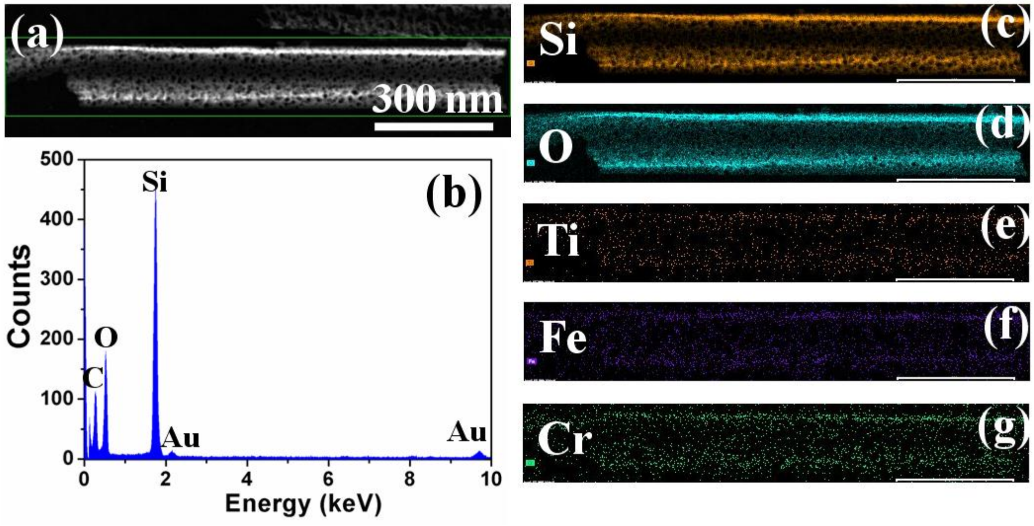

Figure 3.15 (a) TEM image of a SiNW detached from MG-Si. (b) EDX spectrum of the SiNW. The Au signal was from the gold TEM grid. Carbon signal was from the carbon layer on the TEM grid and environmental contaminations. (c-g) EDX mapping of elements including Si, O, Ti, Fe Cr. EDX mapping pictures of other elements were not shown, because they behaved identically as pictures of Ti, Fe, and Cr.

We used inductively coupled plasma optical emission spectroscopy (ICP-OES) to quantitatively compare the impurity level of MG-Si before and after etching. Since the MG-Si piece was too thick to etch more than 50% (thickness > 2 cm), we etched MG-Si powder for impurity comparison. The MG-Si powder contained Si particles with different size ranging from 1-100μm shown in **Fig. 3.16**(a). After etching in HF, H_2O_2 and ethanol solution for 15 min, AgNPs penetrated ~1–2.5 μm deep into the MG-Si particles (see Fig. 3.16 (b-d)).

We compared MG-Si powder with four different treatments, including raw MG-Si particle, MaCE processed, MaCE+HNO_3 processed, and HF+H_2O_2/HNO_3 acid washed (etching without Ag deposition). Simple acid washing could remove all kinds of metals with the reduction ratio of 60-95% agreeing well with previous reports on acid leaching [75] (see **Table 3.1**). MG-Si was upgraded from 99.74 to 99.975%. Removal ratios of most of metals such as Mg, Ti, Cr, Fe, and Ni were higher than those of acid washed one because more surface areas were exposed to the etchant (see Fig. 3.16(e) and Table 3.1). Especially for Fe (impurity showing the largest amount), its concentration decreased by 98%. MG-Si was purified to 99.9881% (without taking Ag catalysts into account). Compared with the acid washed sample, however, Ca showed no reduction due its reaction with HF forming CaF_2 precipitates, which could be trapped and adsorbed in porous MG-Si. Transition metals nobler than Pb were not removed as effective as for the acid washed sample shown in the Table 3.1, and the amount of Cu was even higher. The subsequent HNO_3 step further purified MG-Si to 99.9884%, by washing out the Ag catalysts, as well as CaF_2 and metals adsorbed on porous MG-Si particle. Fig. 3.16(e) revealed the metals which were more improved compared with acid washed sample, the purification enhancement of the HNO_3 step was large for Ca, Pb, and Cu, but small for relatively light metals Zn, Cr, Ni.

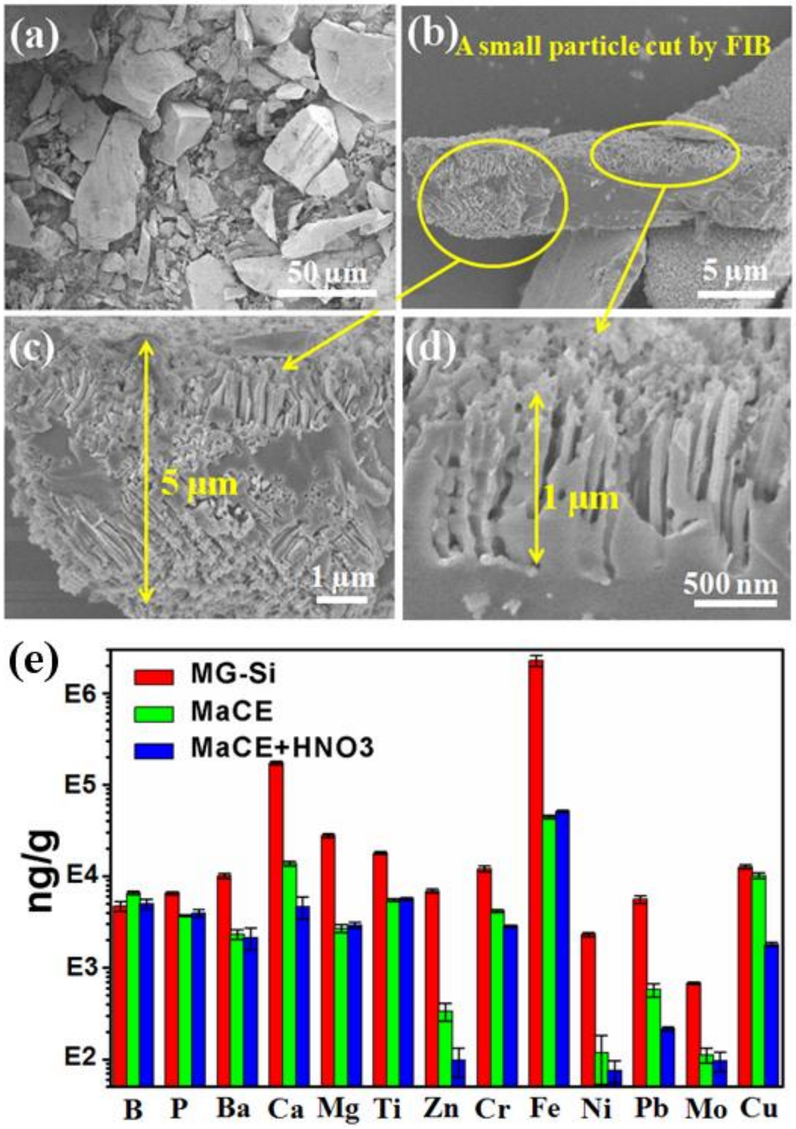

Figure 3.16 SEM images of MaCE processed MG-Si at different magnifications: (a) Top view, (b-d) Cross-sectional view. The MG-Si particle was cut by plasma FIB. (e) The impurity levels in MG-Si powders treated by three different methods: MaCE (green), MaCE+HNO_3 (blue), and etching without Ag (red).

ng / g	B	P	Ba	Ca	Mg	Ti	Zn
MG-Si	**4.7E+03**	**6.6E+03**	**1.0E+04**	**1.7E+05**	**2.8E+04**	**1.8E+04**	**6.9E+03**
acid wash	**5.7E+03**	**4.4E+03**	**3.3E+03**	**1.3E+04**	**8.0E+03**	**6.8E+03**	**2.6E+02**
Reduction percentage	**No**	**32.6%**	**67.4%**	**92.7%**	**71.8%**	**62.2%**	**96.2%**
MaCE	**6.6E+03**	**3.7E+03**	**2.3E+03**	**1.4E+04**	**2.7E+03**	**5.5E+03**	**3.4E+02**
Reduction percentage	**No**	**43.2%**	**77.1%**	**92.0%**	**90.4%**	**69.4%**	**95.1%**
MaCE+HNO_3	**5.0E+03**	**3.9E+03**	**2.1E+03**	**4.7E+03**	**2.9E+03**	**5.7E+03**	**9.8E+01**
Reduction percentage	**No**	**40.0%**	**78.8%**	**97.3%**	**89.5%**	**68.5%**	**98.6%**

ng / g	Cr	Fe	Ni	Pb	Mo	Cu	
MG-Si	**1.2E+04**	**2.3E+06**	**2.3E+03**	**5.6E+03**	**6.8E+02**	**1.3E+04**	
Etching without Ag	**5.3E+03**	**1.0E+05**	**3.0E+02**	**3.8E+02**	**8.6E+01**	**7.9E+02**	
Reduction percentage	**56.7%**	**95.6%**	**87.2%**	**93.6%**	**87.3%**	**93.8%**	
MaCE	**4.2E+03**	**4.4E+04**	**1.2E+02**	**5.8E+02**	**1.1E+02**	**1.0E+04**	
Reduction percentage	**65.4%**	**98.1%**	**94.9%**	**89.7%**	**83.6%**	**19.5%**	
MaCE+HNO_3	**2839.87**	**5.1E+04**	**7.5E+01**	**2.2E+02**	**9.7E+01**	**1.8E+03**	
Reduction percentage	**76.6%**	**97.8%**	**96.7%**	**96.1%**	**85.8%**	**85.8%**	

Table 3.1 Impurity amount in raw MG-Si powder, acid washed (etching without Ag), MaCE and MaCE+HNO_3 processed ones. Reduction percentage indicates the metal removal ratio (***in comparison with raw MG-Si***). Co and Ag are below detection limit.

3.3 Discussion: A chemical mode

3.3.1 Etching attack at the SiNW sidewalls

During the formation of SiNWs, there is a constant etching attack at the SiNW sidewalls resulting in the defect or tiny pore formation on the SiNW surface. X. Zhong et al. [76] ascribed such attack to the slow dissolution of Ag catalysts in the HF and H_2O_2 solution according to the following reaction:

$2Ag + H_2O_2 + 2H^+ \rightarrow 2Ag^+ + 2H_2O$ (e.q. 3.1)

Even most of Ag^+ ions can be quickly reduced back to the original Ag catalyst by taking electrons from oxidizing Si, however, part of Ag^+ ions diffuse upwards from the root of SiNWs, and renucleate on the sidewalls. The reaction is

$Si + 4Ag^+ + 6F^- \rightarrow 4Ag + SiF_6^{2-}$ (e.q. 3.2)

The renucleated tiny Ag particles again act as new etching sites. We confirm such reaction by EDX mapping and adding HCl solution (1 M) into the etchant. Fig. 3.17 shows the cross sectional view of SiNWs and the corresponding EDX mapping of Ag element. The distribution of Ag elements demonstrated gradient concentration towards the etching direction. Furthermore, if HCl was added, the transparent etchant turned into white blurry solution due to formation of AgCl precipitates; and no SiNWs could be obtained.

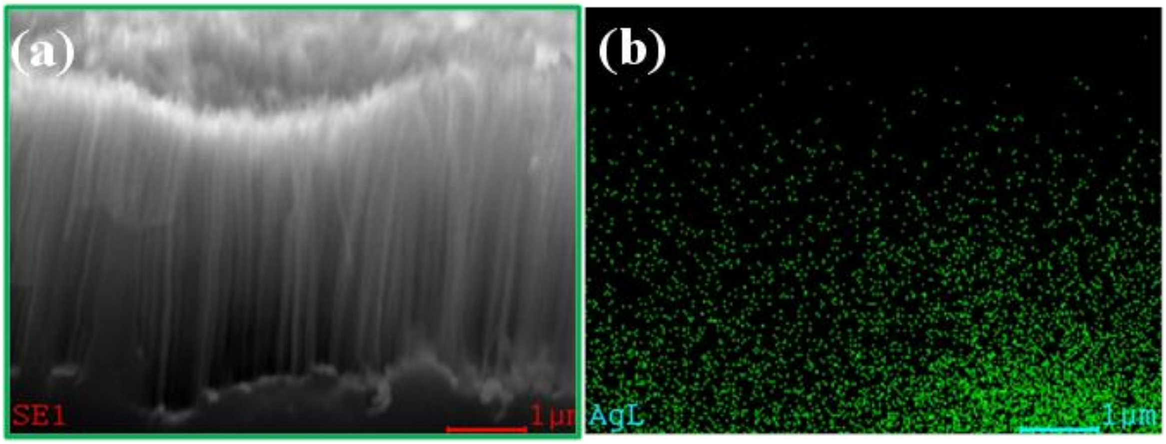

Figure 3.17 (a) SEM image of the obtained SG-SiNWs after etching in 5 M HF + 0.3 M H_2O_2. (b) Corresponding Ag elemental mapping image by the EDX spectroscopy.

Increasing the doping level of the Si wafer would cause more redeposition of Ag nuclei at the SiNW sidewalls, due to large number of defective sites near dopants that are favorable for the etching. Thus, there were more tiny pores formed at the side walls of SiNWs for p^+-type Si. For the p^{++}-type Si, SiNWs turned into totally porous (see Fig. 3.4). Such Ag dissolution and redeposition mechanism also leads to the imperfect formation of SiNW arrays (see Section 3.1.2). Because part of thermal evaporated Ag catalysts were dissolved, they failed to confine the SiNW size to the diameter of the PS beads.

3.3.2 Etching model of porous SiNW formation

To understand the upgrading effect showing the relevance between the reduction levels of metals (see **Fig. 3.18**) and a formation of porosity in MG-SiNWs, we need to consider the following three key factors:

1. Heterogeneous distribution of metal impurities inside MG-Si [77-79];

2. Effect of dissolved metal ions on MaCE;

3. Interaction between different metal ions.

Different solid solubilities between impurity elements in Si mainly cause a non-uniform distribution of metal impurities. During solidification of Si from molten state, impurities (e.g. Fe) with concentrations exceeding their low solid solubilities mainly segregate along the grain boundaries [77,78]. Since the grain boundaries are morphologically defective in crystal structures, the nucleation of AgNPs preferentially occurs at these defect sites which are energetically more favorable for etching. As a result, a high Si dissolution rate is observed at grain boundaries than other areas (see **Fig. 3.19** and **Table 3.2**), the strong removal of Fe is thus reasonable upon MaCE.

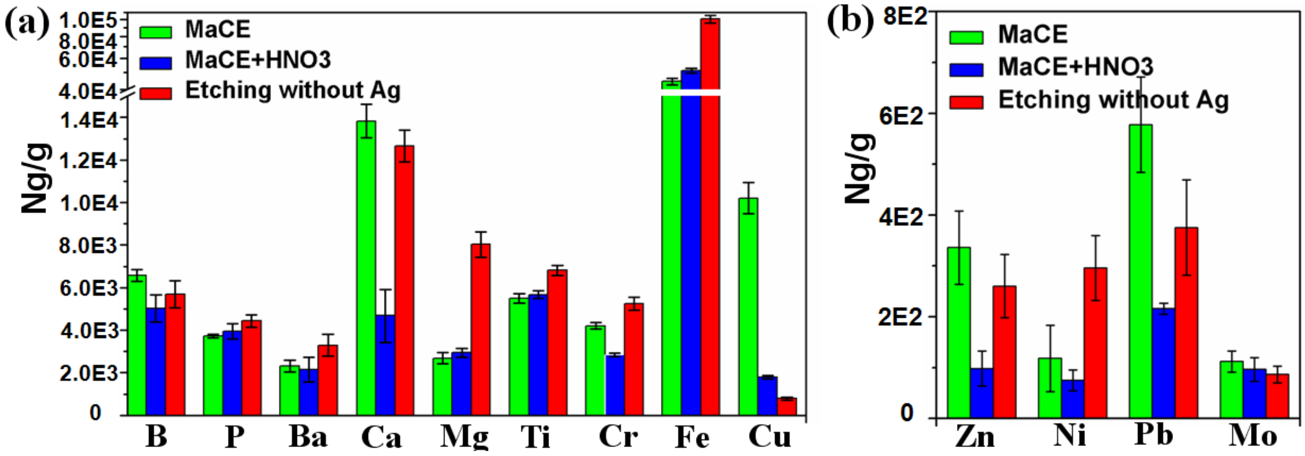

Figure 3.18 (a-b) Impurity levels in MG-Si powder treated by three different methods: MaCE (green), MaCE+HNO_3 (blue), and HF+H_2O_2/HNO_3 (acid wash without Ag deposition (red))

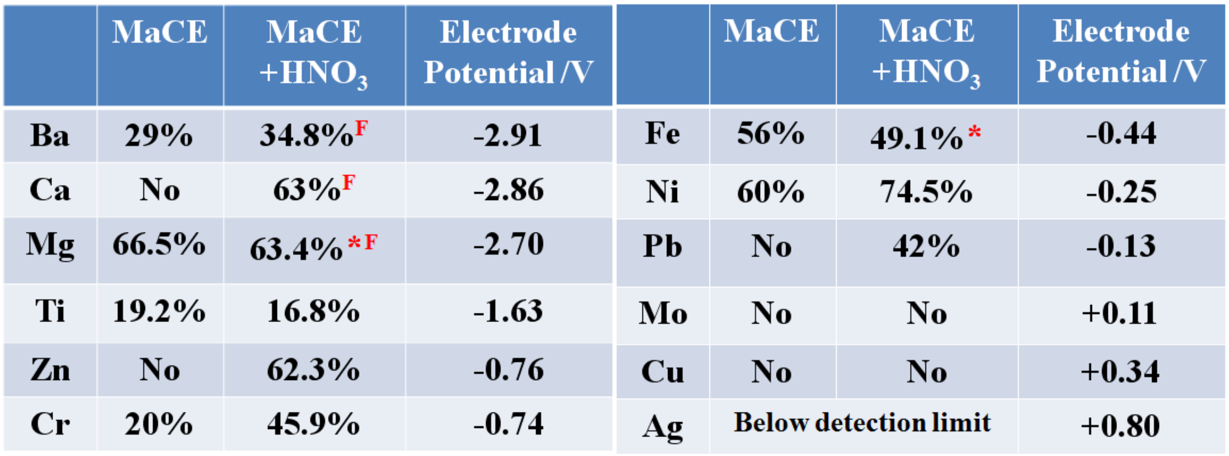

	MaCE	MaCE +HNO_3	Electrode Potential /V		MaCE	MaCE +HNO_3	Electrode Potential /V
Ba	29%	34.8%^{F}	-2.91	Fe	56%	49.1%*	-0.44
Ca	No	63%^{F}	-2.86	Ni	60%	74.5%	-0.25
Mg	66.5%	63.4%*^{F}	-2.70	Pb	No	42%	-0.13
Ti	19.2%	16.8%	-1.63	Mo	No	No	+0.11
Zn	No	62.3%	-0.76	Cu	No	No	+0.34
Cr	20%	45.9%	-0.74	Ag	Below detection limit		+0.80

Table 3.2 Table lists reduction ratios of MG-Si samples treated by MaCE and MaCE+HNO_3 (***in comparison with MG-Si etched without Ag***). Red-colored 'F' denotes the metal ions reacted with HF to be fluoride precipitates. Red-colored '*' indicates a possibility of contamination from the environment, which causes an increase of reduction ratios upon HNO_3 cleaning. The standard electrode potential data were extracted from Ref. 17.

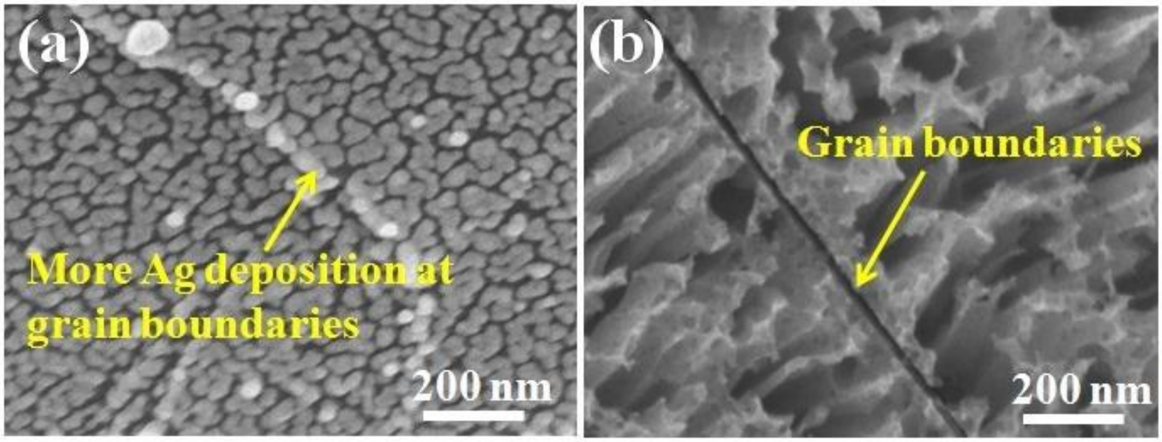

Figure 3.19 Top-view SEM images of the MG-Si particle (a) after Ag deposition, and (b) after MaCE.

The second factor (effect of dissolved metal ions) also plays a crucial role during MaCE of MG-Si. During the ‘drilling’ process of AgNPs, metal impurities would be dissolved upon exposure to the acidic etchant. **Fig. 3.20** (a,b) show that many tiny metal particles spreading all over the surfaces of MG-SiNWs. We confirm that most of nanoparticles are Ag by energy dispersive X-ray spectrometer installed in SEM (SEM-EDX) (see **Fig. 3.21**). As stated in Section 3.3.1, Ag catalysts locating at the roots would be partially dissolved, diffuse upwards and renucleate on the sidewalls of nanowires to initiate new etching pathways. Since there are a large amount of defective sites near the dopants in heavily doped Si (10^{19}-10^{20}cm^{-3}), many AgNPs will renucleate at the NW surfaces. Here, the doping level of MG-Si is low (B - 6.6×10^{17} cm^{-3} and P -3.0×10^{17} cm^{-3}). Therefore, we speculate that the metal impurities instead of dopants are the reason of the nucleated Ag particles on MG-SiNWs.

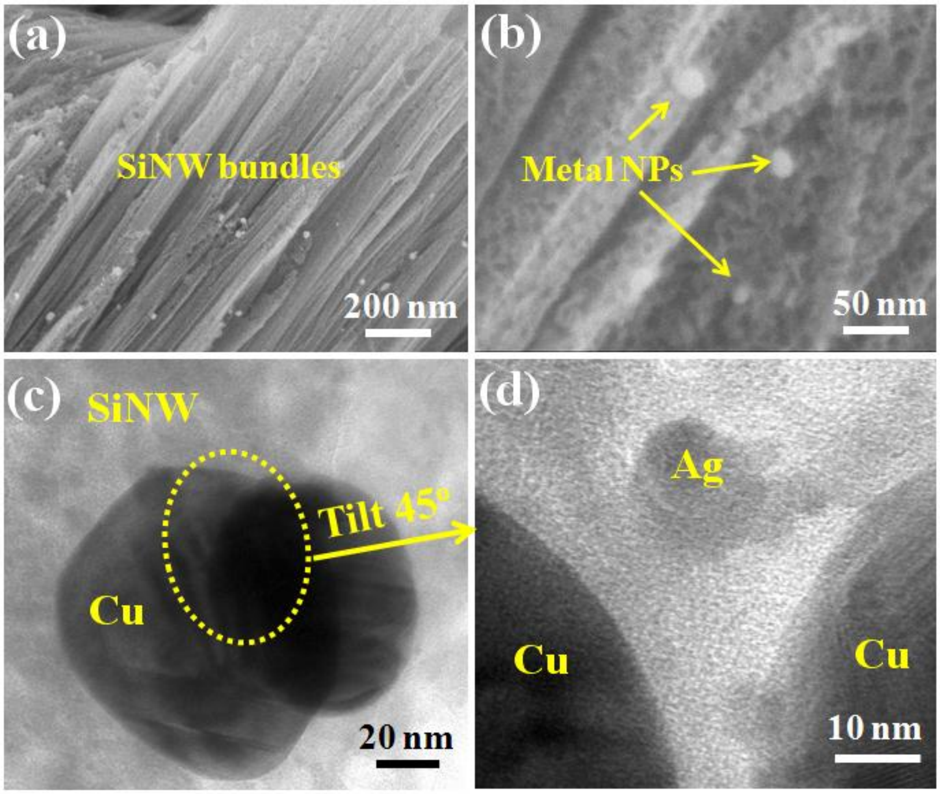

Figure 3.20 (a, b) SEM images of MG-SiNW bundles formed after MaCE at low and high magnification. (c, d) TEM images of metal NPs on MG-SiNWs at low and high magnification. The white dots in (a) and (b) are metal nanoparticles.

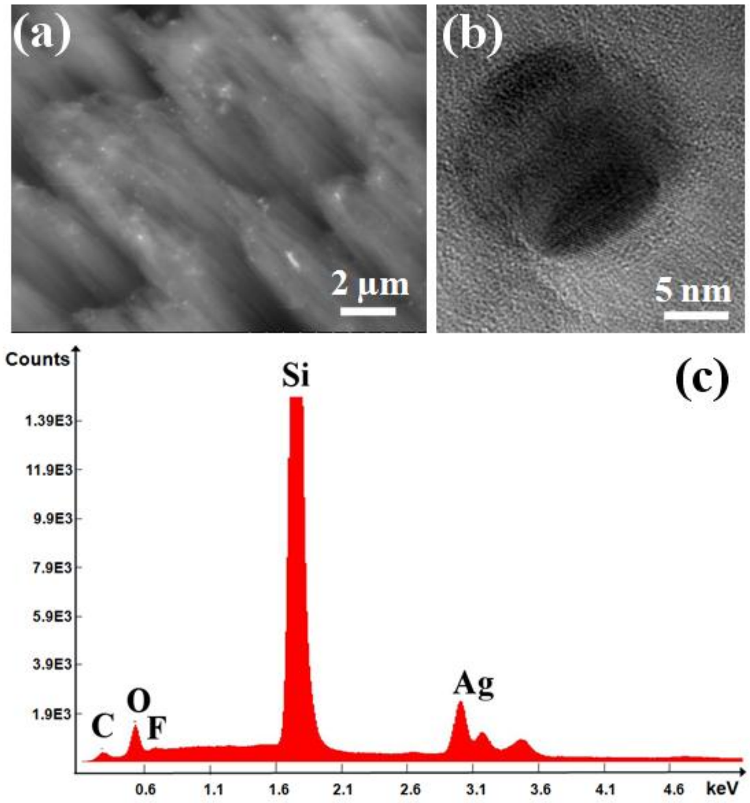

Figure 3.21 (a) SEM images of MG-SiNWs. White dots are the metal nanoparticles. (b) A tiny Ag particle in a MG-SiNW. (c) EDX spectrum of the MG-SiNW shown in (a).

In order to confirm our assumption, we first conducted the etchant contamination experiment during MaCE of ultra-pure EG-Si. The etchants were separately contaminated each with 1mM metal ions, i.e., Ca^{2+}, Fe^{2+}, Co^{2+}, Ni^{2+}, Cu^{2+}, and Ag^{+}. Metals nobler than Ni or Co, were easily nucleated at the Si surface at the cost of the dissolution of SiNWs (see **Fig. 3.22**). The reactions are as follows [33]:

Metal deposition: $M^{+} + e^{-} \leftrightarrow M^{0}$ $E_{o} \geq \sim -0.3$ V vs. NHE (Nobler than Co)

Silicon dissolution: $Si^{0} + 6F^{-} \longrightarrow [SiF_{6}]^{2-} + 4e^{-}$ $E_{o} = -1.24$ V vs. NHE

We find the NW dissolution rate would increase with the positive increase of the standard electrode potential of metal [80], because the driving force for such reaction is the potential difference between the above two half-cell reactions. Metals with enough positive electrode potential (i.e. Cu, Ag) would fully cover the Si surface. During MaCE of MG-Si, the concentrations of dissolved metal ions are estimated to vary in a big range from ~20 μM (Fe) to ~7.1×10^{-3} μM (Mo) (suppose 0.1 g MG-Si dissolved in 100 mL etchant) depending on their original concentrations inside MG-Si. In the second etchant contamination experiment, the six kinds of metal ions above mentioned were mixed together. With the increase of mixed metal ion concentration, the growth speed of EG-SiNWs was lowered from 0.36 μm/min (no metal ions) to 0.14 μm/min (1 μM metal ions) to 0.08 μm/min (10μM), indicating the slow dissolution of EG-SiNWs (see **Fig. 3.23**). In the real case, the etching environment during MaCE of MG-Si is far more complex than simply mixing the metal ions. The metal impurities are originally non-uniformly distributed, and their concentrations differ from area to area. But, why do MG-SiNWs turn to be uniformly porous?

We propose a new etching model as shown in **Fig. 3.24**, explaining the influence of metal impurities on the NW morphology. In this model, metal impurities are classified metals into three types: M_1metal with large negative redox potentials (from Ba to Fe listed in Table 3.2), M_2 metal with moderate negative redox potentials (from Ni to Mo), M_3 metal with small positive redox potentials (Cu, Ag). For M_1 metals, they simply exist as ions after dissolution (Ti, Cr, Fe), or precipitates (MgF_2, CaF_2, BaF_2). M_2 ions can attract the electrons emitted from Si, and are renucleated at the SiNW surfaces, causing Si dissolution and porosity formation. Due to the instability of M_2 metals, they would be dissolved again in the etchant, and a repeated renucleation/dissolution cycle is formed. For M_3 metals, there is an extra Ag^+ source from the dissolution of original Ag catalysts locating at the roots of SiNWs. Compared with M_2 metals, Cu and Ag ions not only have the repeated cycle etching, but also catalyze the etching reactions for dissolving more Si area surrounding metals, due to the high catalytivity of their metallic particles. The metal ions become uniformly distributed because of the diffusion of metal ions in the etchant. Hence, homogeneous distributed pores in MG-SiNWs are created.

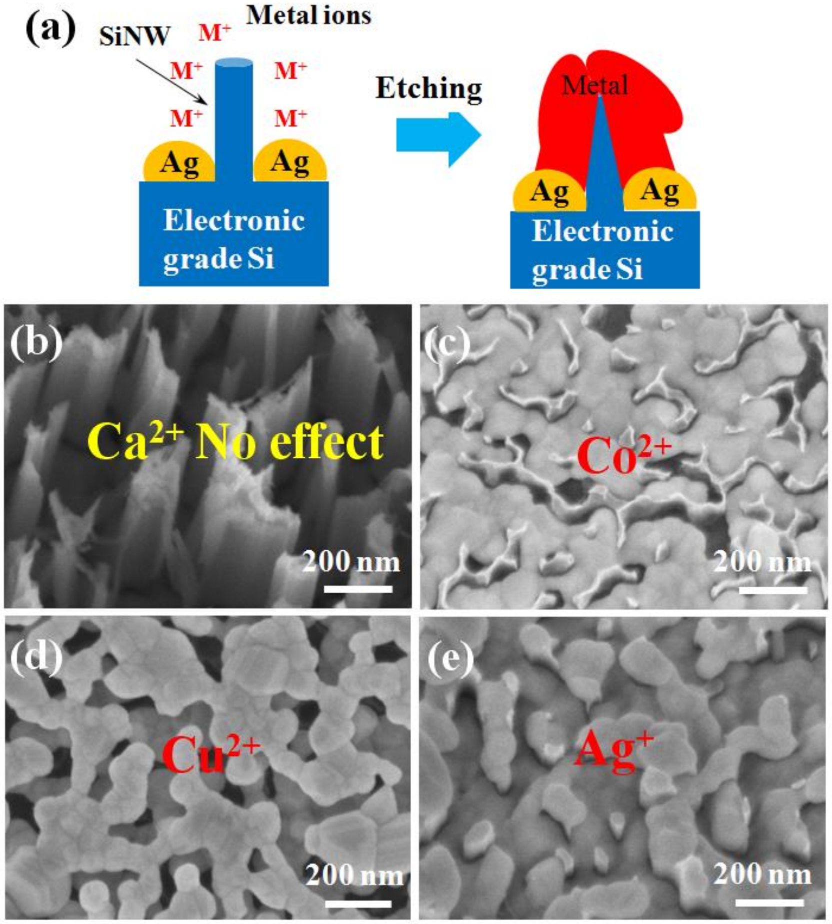

Figure 3.22 (a) Schematic of the effect of metal ions on MaCE. Tilt SEM images of the EG-Si surfaces after etching in solutions HF + H_2O_2 each contaminated with 1 mM different metal ions (b) Ca^{2+}, (c) Co^{2+}, (d) $Cu^{2+}$and (d) Ag^+.

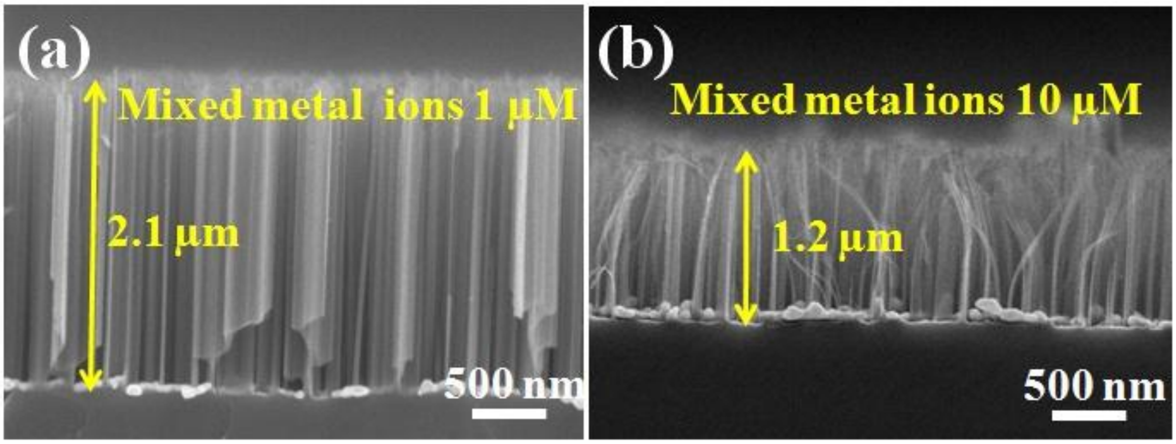

Figure 3.23 Cross-sectional SEM images of SiNWs obtained from the contaminated etching solution HF + H_2O_2. The contamination was done by mixing six different metal ions (Ca^{2+}, Fe^{2+}, Ni^{2+} Co^{2+}, Cu^{2+}, Ag^{+}) with a concentration of (a) 1 μM and (b) 10 μM, respectively.

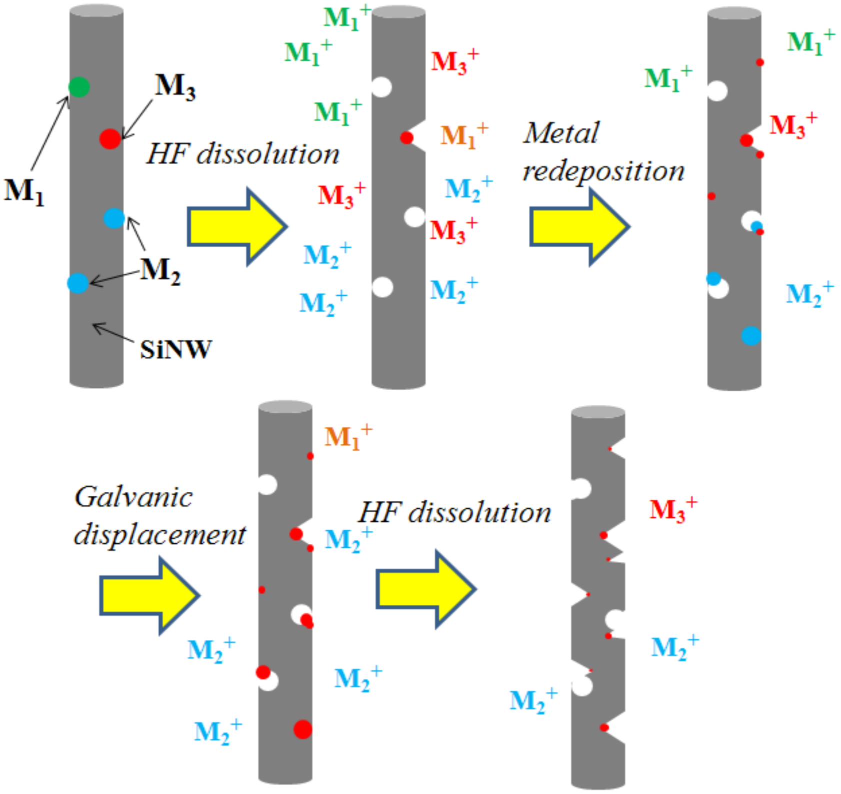

Figure 3.24 Schematic diagrams of the new etching model for MaCE of MG-SiNWs. Three different colors represent three different types of metals: M_1 (Ba, Ca, Mg, Ti, Cr, Zn, Fe, green

color), M_2 (Ni, Co, Pb, Mo, blue color) and M_3 (Cu, Ag, red color). M^+ represents the dissolved metal ions.

Given a third factor stressing the interaction of different metals, it is reasonable that galvanic displacement would happen if the noble metal M_3 ions surround the renucleated M_2 metal particles. As shown in Fig. 3.24, such reaction would replace all the renucleated M_2 particles with M_3 particle. Furthermore, because such reaction would deplete M_3 ions in the etchant, and Cu amount is low in MG-Si, it would promote the dissolution of original Ag catalysts at the root of SiNWs. As a result, there are much more tiny Ag particles nucleated at MG-SiNWs than those at EG-SiNWs.

To verify our model, we carefully conducted the TEM-EDX analysis of several MG-SiNWs without HNO_3 treatment. Most of tiny metal particles are Ag agreeing with large area SEM-EDX analysis, and no M_1 and M_2 particles are detected. Interestingly, Cu particles can be found in few MG-SiNWs shown in Fig. 3.20(c). Since there are no Cu ions in the etchant, it provides the direct evidence of the dissolution/renucleation model. We unexpectedly find that the diameter of Cu particles (60-90 nm) is much bigger than that of the neighboring Ag particle (~ 9 nm). We speculate that due to the positive electrode potential of Cu, its renucleation speed is quicker and its displacement speed by Ag is lower than those of M_2 metals. Based on our model, we can conclude that the difficulty of removing a metal by MaCE increases with the positive increase of its electrode potential. Therefore, MaCE is easy to remove M_1, hard to remove M_2 and very difficult to remove M_3. The subsequent HNO_3 cleaning step is thus critically important for purifying MG-Si.

3.4 Summary

In this chapter, we demonstrate the power of MaCE. It not only can create large areas of SiNWs from ‘clean’ Si (EG- and SG-Si) and ‘dirty’ UMG- and MG-Si, but also has the ability to remove the metal impurities inside ‘dirty’ Si. Through element analysis (ICP-MS and ICP-OES), we confirm the superior purification of MaCE over the traditional acid leaching. The MG-Si powder was upgraded from 99.74 to 99.9884%, and the UMG-Si wafer was purified from 99.999772 to 99.999899%. Furthermore, the strong metal impurity removal process induced unique features in SiNWs. For UMG-Si, some SiNWs showed local line etching defects; and for MG-Si, uniform porous feature was developed inside SiNWs. In order to explain the porosity formation in SiNWs and different reduction levels of metal impurities in ‘dirty’ Si, we propose a new chemical etching model. This model takes into consideration of various dissolved metal impurities from ‘dirty’ MG-Si and Ag^+ ions from original Ag catalysts in the etchant. The metal ions (nobler than Ni or Co) go through diffusion and repeated metal renucleation/dissolution cycles, forming SiNWs with homogeneously distributed pores despite of heterogeneously metal impurity distribution in MG-Si. This model not only highlights the importance of controlling the metal ion concentration and selecting metal types for engineer porous features in NW, but also explains the reason of the difficulty of removing noble metals such as Cu.

We believe the obtained SiNWs from ‘dirty’ Si would have a great potential of applying not only in solar energy conversion, but also in thermoelectrics, lithium ion battery and sensors while keeping fabrication cost extremely low. Moreover, this room temperature MaCE technique can be easily scaled up for mass production, and would possibly emerge as a new route to upgrade MG-Si to solar grade in the near future.

4

POROUS Si FABRICATED BY PaCE

Previous literatures have reported that porous Si films can be fabricated by using Pt as the catalyst instead of Ag [31,81]. The main reason is that Pt is a highly active catalyst for decomposing H_2O_2 [65]. Thus, excessive holes would be injected leading to the formation of a highly porous structure. However, the fabrication of uniform microporous (micro-PSi) or mesoporous Si (meso-PSi) film by MaCE has not been reported in the literature yet, and also the possibility of controlling the porosity has not been shown.

In Section 4.1, through systematic studies of Pt nanoparticle assisted chemical etching (PaCE) of Si wafers with various doping levels, we report that uniform meso-PSi can be obtained by etching highly doped p^+-type Si (0.01-0.02 Ω cm). In contrast, non-uniform micro-PSi was formed on lightly doped p- and n-type Si. Through changing the HF and H_2O_2 concentration, we achieve a flexible tuning of meso-PSi layer. Moreover, a meso-PSi membrane can be obtained.

To understand the morphological difference of the produced micro- and meso-PSi, a physical model based on the nano-Schottky contact is proposed in Section 4.2. This model also explains the observed but unexpected motion of metal NPs during etching. The mechanism of porosity tuning is also analyzed.

4.1 Porous Si fabricated by Pt assisted chemical etching

Cz-grown, electronic grade, single-side polished p-type and n-type, single-crystal Si(100) wafers with two types of resistivity, 1-10 Ω cm (p^-, n^-, moderately doped) and 0.01-0.02 Ω cm (p^+, n^+, highly doped) were used in this study.

Sparsely distributed spherical Pt nanoparticles (PtNPs) were deposited on the Si surfaces using galvanic displacement by immersing the Si samples into a solution containing 0.5 M HF and 1 mM K_2PtCl_6. As shown in **Fig. 4.1**, the diameter of the PtNPs ranges from 50-200 nm, and the density and size of NPs slightly decrease with the doping level. In contrast, a high density of almost touching AgNPs is easily formed in all kinds of silicon wafers (see Fig. 3.1).

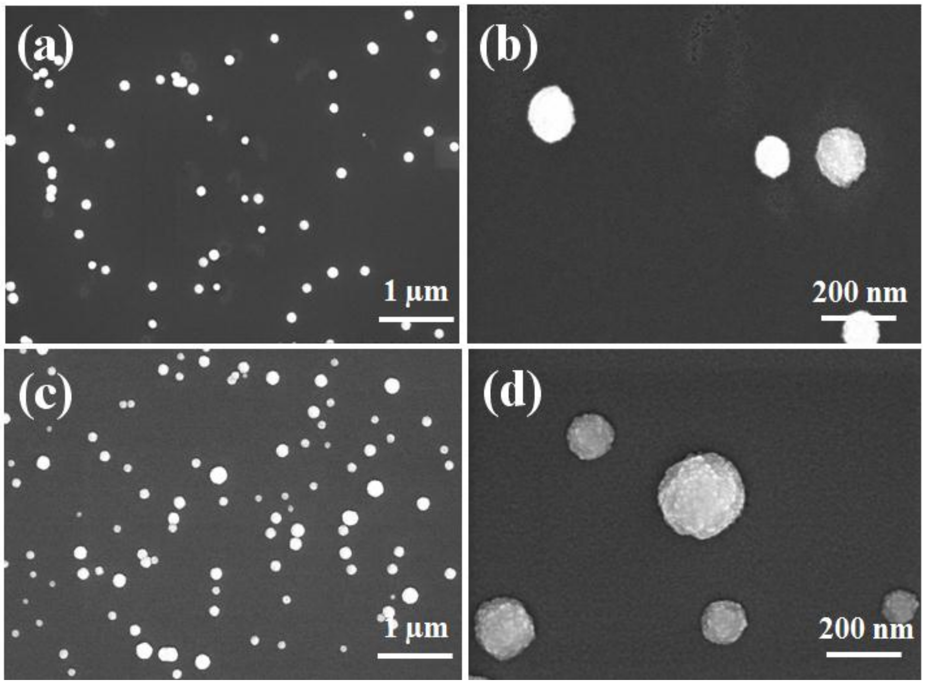

Figure 4.1 Top-view SEM images of Pt nanoparticles (NPs) deposited on silicon substrates with different doping level: (a-b) PtNPs deposited on moderately doped p^--type Si (1-10 Ω cm) for 3

min, (c-d) PtNPs deposited on highly doped p^+-type Si (0.01-0.02 Ω cm) for 3 min. (b) and (d) are the high magnified view of (a) and (c), respectively.

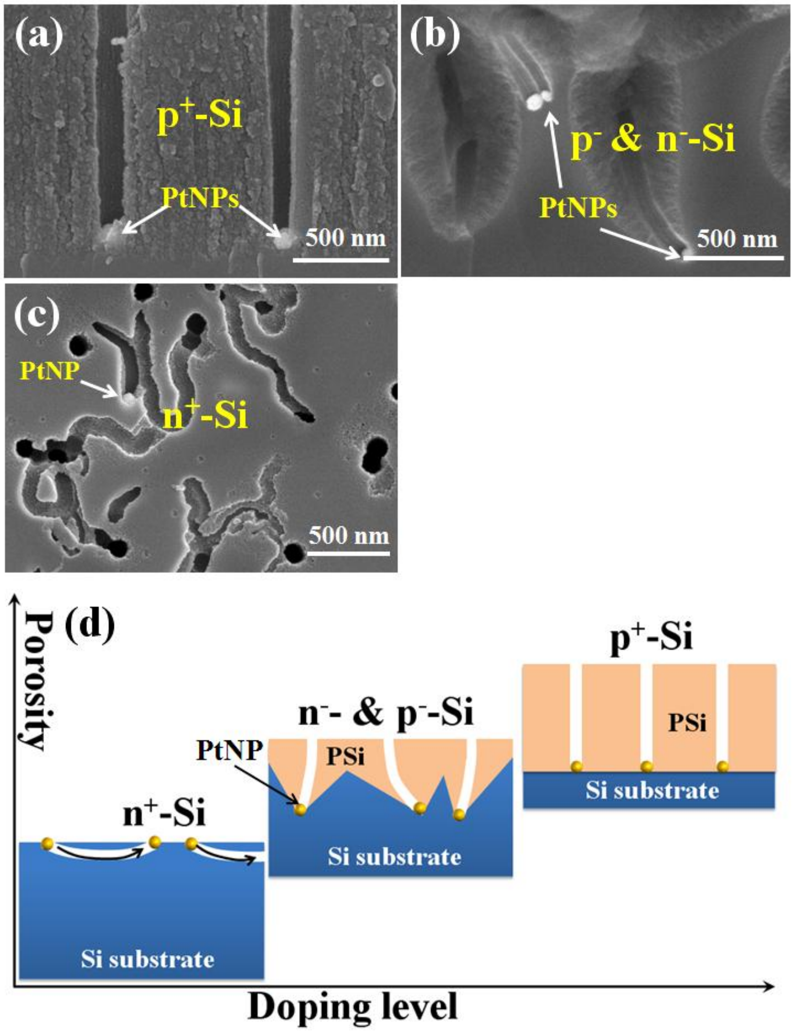

Figure 4.2 SEM images of (a) p^+-Si after etching, (b) p^--Si and n^--Si after etching, and (c) n^+-Si after etching. (a) and (b) are cross-sectional views. (c) is the top-view. (e) A schematic map of porosity vs. doping level of silicon.

We firstly investigate PaCE on Si samples with various levels of doping as shown in **Fig. 4.2**. Porous Si can be obtained in p^+-, p^-- and n^--type Si. The PtNPs deposited on the n^+-Si are not able to penetrate deep into the Si substrate, and reveal a high mobility near the surface during etching. Thus, in this work we mainly concentrate on the etching of p^+- and p^--Si.

Fig. 4.3(a-d) show cross-sectional SEM and TEM images of as-generated PSi in p^+-Si. Silicon beneath the PtNPs was dissolved, and macropores of about d_{macro} = 80 nm were drilled in the <100> direction (see Fig. 4.3(b)) by the PtNPs. Meso-PSi formed in areas without metal coverage as it has already been observed in Ref. 31. The porosification of meso-PSi was very uniform, and its etching rate was nearly the same as the macropore etching rate below the PtNPs. In contrast, SiNWs were obtained without formation of meso-PSi on the highly doped p^+-Si for MaCE with AgNPs under the same etching condition.

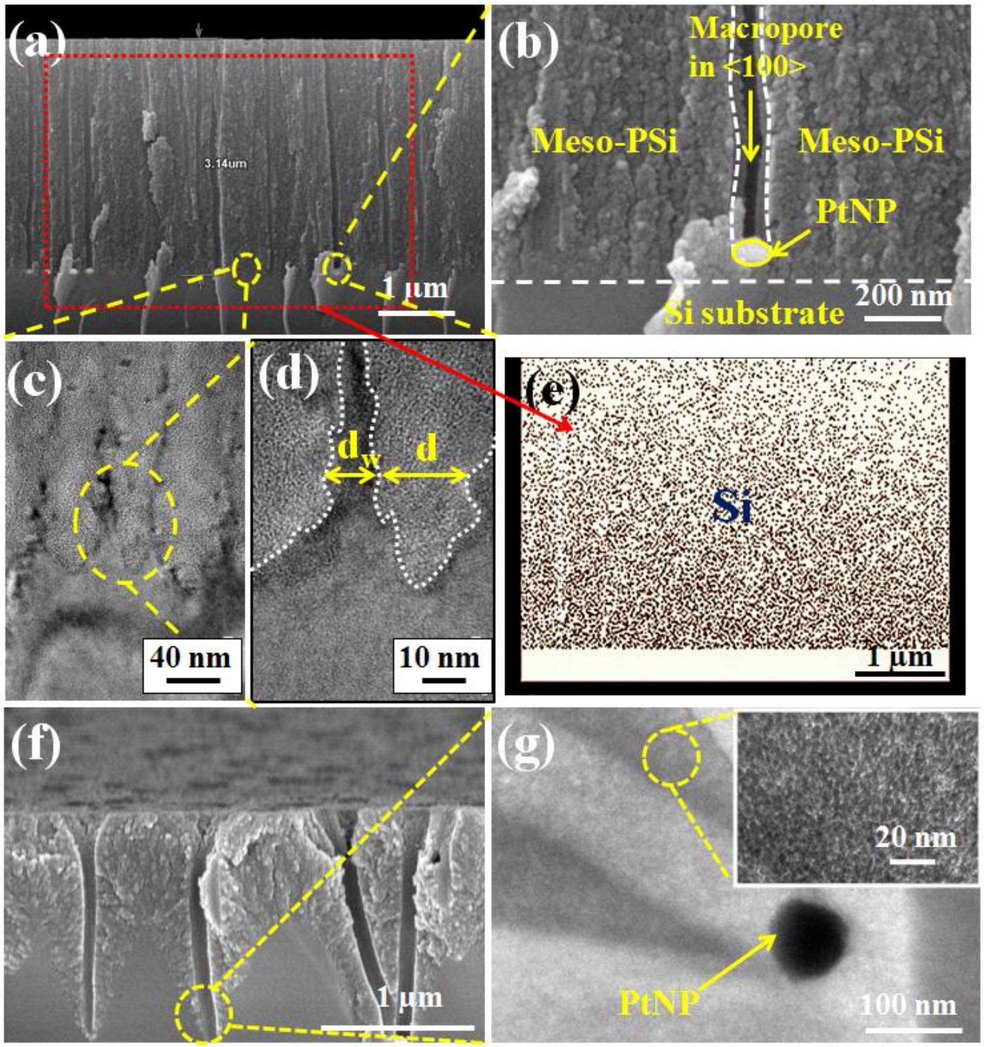

Figure 4.3 (a, b) Cross-sectional SEM images of meso-PSi fabricated by etching of a PtNPs loaded highly doped p^+-Si substrate (0.01-0.02 Ω cm) in HF and H_2O_2 solution; (c,d) HRTEM images of meso-PSi at different magnification; (e) EDX mapping of Si; (f, g) Cross-sectional SEM images of micro-PSi by etching of a PtNPs loaded, moderately doped p^--Si substrate (1-10 Ω cm). (b) and (g) are the magnified view of (a) and (f), respectively. The dashed white lines show the border of PSi structure in (c) and (d).

The HRTEM images in Fig. 4.3(c-d) reveal the structural details of the meso-PSi region. The dark regions observed in the TEM images are due to the diffraction contrast created by strain fields along the PSi/Si interface [29]. The pore diameter d is around 20 nm, and the pore wall thickness d_w increases with the depth (d_w~10 nm at the bottom). The etched morphology is very similar to the electrochemically etched mesoporous layers [82]. The energy-dispersive X-ray (EDX) mapping in Fig. 4.3(e) reveals the gradually varying porosity of the meso-PSi. Very low Pt signals are distributed in the meso-PSi layer, indicating the etching attacks the PSi sidewalls (see **Fig. 4.4**). A similar behavior was observed for MaCE based on AgNPs [76]. To validate such an attack from the redeposited Pt nuclei, a Pt wire was placed close to the bare wafer. As a result the polished Si surface turned into PSi, verifying the slow dissolution of Pt into the etchant.

The etched morphologies of Si are totally different for Si wafers with a low doping level. For moderately doped p^--type Si, the macropores induced by PtNPs are surrounded by extremely high porous micro-PSi as shown in the SEM and HRTEM images shown in Fig. 4.3(f) and (g). Compared with meso-PSi, silicon was less dissolved, resulting in non-uniform micro-PSi film.

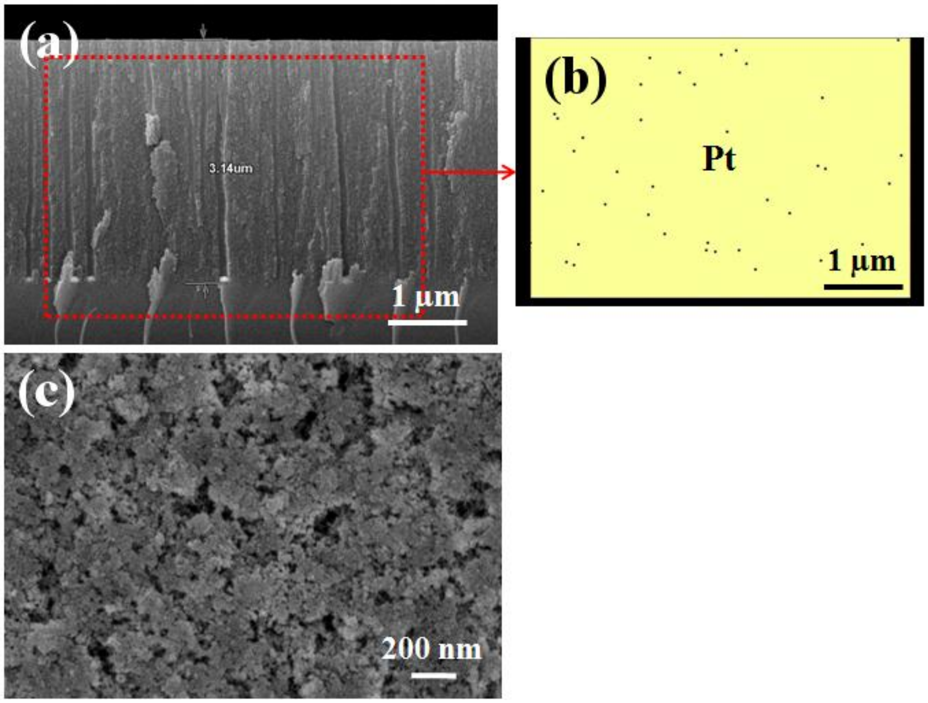

Figure 4.4 (a) Cross-sectional SEM image of meso-PSi etched from p^+-type Si (b) EDX mapping of Pt element in the red square area marked in (a). (The image color was processed to enhance the contrast.) (c) Top view of PSi etched by immersing Pt wire in the etchant solution. The distance between Pt wire and Si substrate was kept around 0.5 cm.

In order to demonstrate the flexibility of PaCE for controlling the porosity and etching rate, the influence of HF and H_2O_2 concentrations during etching of meso-PSi was studied seen in **Fig. 4.5**. A porosity increase can be achieved by decreasing the HF concentration or increasing the H_2O_2 concentration. As shown in Fig. 4.5, decreasing the HF concentration from 15 M to 2.5 M would increase the porosity of meso-PSi (Region II in Fig. 4.5(e), constant H_2O_2 concentration 0.3 M), and meanwhile the etching rate is lowered from 1.7 to 0.5 μm/min. If the HF concentration is lower than 2.5 M, the etching enters the electropolishing region (Region I in Fig 4.5(e)).

We find that the porosity of meso-Si is very sensitive to the change of H_2O_2 concentration. A slight increase of the H_2O_2 concentration above 0.5 M (constant HF concentration 5 M) significantly enhances the Si dissolution reaction, causing strong etching non-uniformity and significant cracking of meso-PSi films. Stable meso-PSi growth is only achieved for the Region II in Fig. 4.5(f). At high H_2O_2 concentration, lots of H_2 bubbles were observed due to the fast etching. These bubbles would cause inhomogeneous etchant diffusion, and impose strong capillary forces to crack the highly porous PSi film of low mechanical strength [29]. Significant cracking was created during N_2 drying of samples (Region III in Fig. 4.5(f)). High H_2O_2 concentration also leaded to the dissolution of the top of meso-PSi. Thus, the etching rate increase is lowered when the H_2O_2 concentration is around 0.75 M (see Fig. 4.5(f)).

The porosity and the thickness of meso-PSi layer can be well controlled by changing the HF or the H_2O_2 concentration, and the etching time within Region II. A meso-PSi membrane was fabricated by using a two-step etching process consisting of a low (0.3 M) and a high (2 M) H_2O_2 concentration shown in Fig. 4.5(c) and (d). The second step was applied for a very short time, and ethanol was added to reduce the capillary forces to reduce cracking.

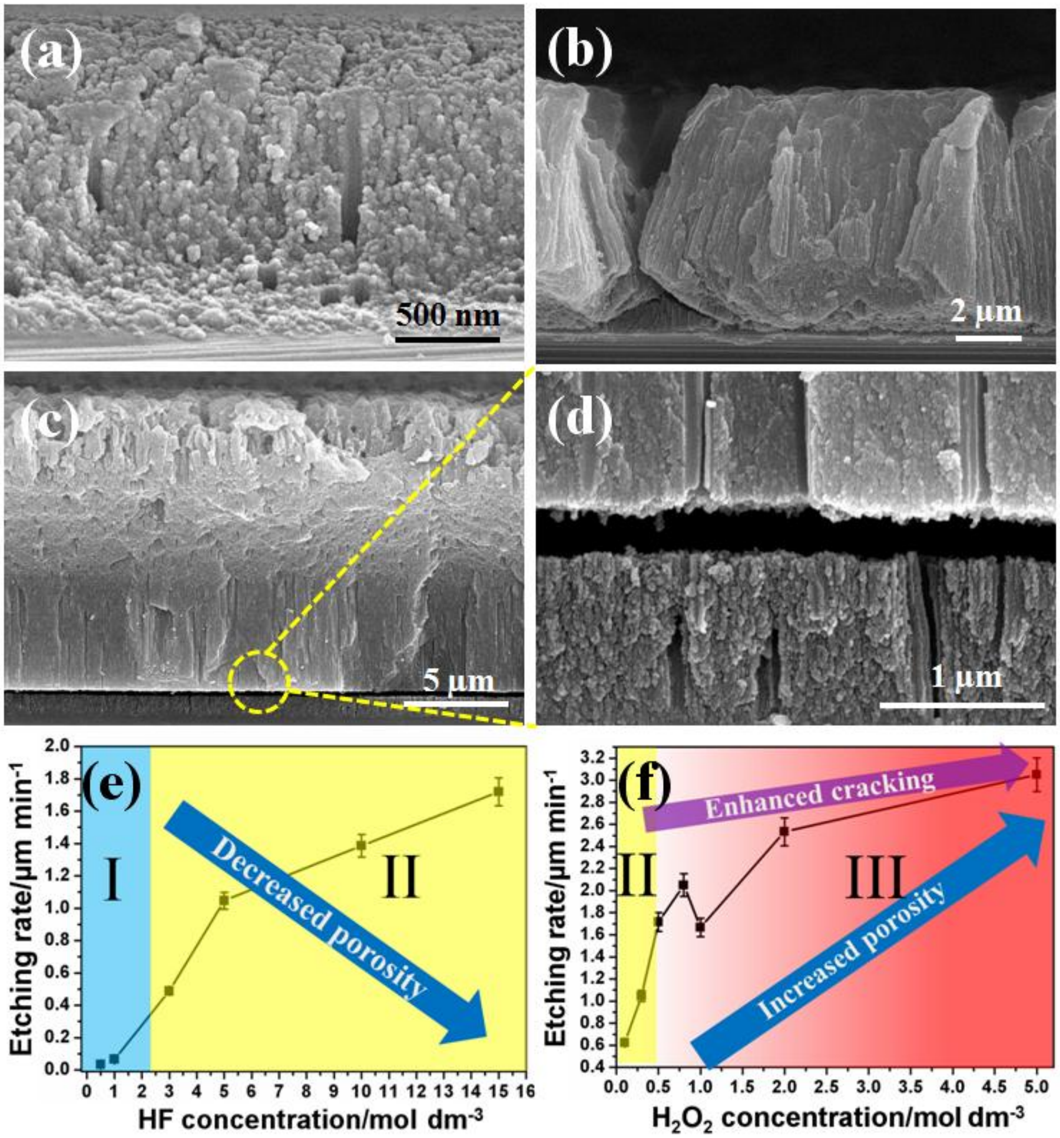

Figure 4.5 SEM images of meso-PSi formed at (a) 3 M HF and 0.3 M H_2O_2, (b) 5 M HF and 0.6 M H_2O_2, (c, d) A meso-PSi membrane fabricated using two etching steps (first step 5M + 0.3 M H_2O_2, second step 5M + 2 M H_2O_2), (e) Dependence of etching rate on the HF concentration while keeping the H_2O_2 concentration constant at 0.3 M, (f) Dependence of etching rate on the H_2O_2 concentration while keeping the HF concentration constant at 5 M. I is the electropolishing regime, II is the stable meso-PSi growth regime, and III is the meso-PSi cracking regime.

4.2 Discussion of results: A physical model

4.2.1 A new etching model based on nano-Schottky contact

There are three major steps involved in PaCE:

(1) Hole supply by the H_2O_2 reduction,

(2) Hole transport over the electronic barriers of electrolyte/Pt and Pt/Si,

(3) Si dissolution by HF.

The morphology of porous Si is determined by the step which is rate limiting. Since Pt can decompose H_2O_2 more effectively than Ag [65], more holes would be supplied while using PtNPs as the catalysts. This leads to higher etching rates and porosities compared to Ag assisted etching. Thus, step (1) would not be the rate limiting step. In addition, because the HF concentration used here is 5 M, which is enough to etch through the wafer, step (3) cannot act as the main factor influencing the morphology of porous Si.

To explain the morphological differences between micro- and meso-PSi formed by Pt as a catalyst, the key is to understand the hole flow through the PtNP-Si nano-Schottky contact. In the following, we first derive the band diagram of the interface between p-type Si and PtNPs in the etchant; afterwards, we simulate the electric field distribution of the PtNP-Si nano-Schottky contact based on Tung's model [83].

The band diagram is sketched in **Fig. 4.6**. When a p-type Si is brought in contact to the etchant, band bending occurs at the Si surface, resulting from equilibration of the Fermi energy level in Si with that of the chemical potential (redox potential) in the etchant [84]. The result of such an equilibration is the formation of an energetic (Schottky) barrier Φ_B^o that inhibits charge transfer at the interface. After metal NP deposition, the Fermi level E_F(M) is found to be relatively low compared with E_F(E), near the valence band edge of E_V(E). The conduction and valence band edges (E_C(M) and E_V(M)) at the metal NP-Si change their energetic locations according to E_F, while the band edges of E_C(E) and E_V(E) at the etchant-Si interface remain constant [84]. Meanwhile, the local barrier height at the NP-Si interface is lowered to $\Phi_{B,M}$, depending on the value of the metal work function.

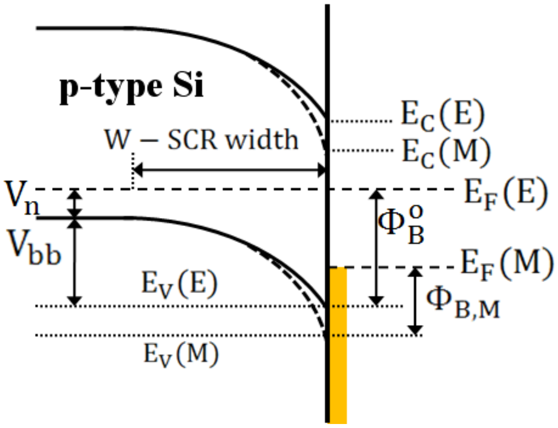

Figure 4.6 (a) Schematic energy band diagram for a metal NP/p-Si in the dark. E_F, E_C, and E_V are the Fermi level, conduction and valence band of p-Si, respectively. *E(M)* and *E(E)* represent the energy levels of metal-Si and metal-etchant contact, respectively. SCR is the space charge region. Φ_B^o is the surface barrier height of Si-solution contact. $\Phi_{B,M}$ is the surface barrier height of metal-Si. V_n is the energy difference between the Fermi level and valence band of silicon and V_{bb} represents the band bending. The band bending potential V_{bb} is the difference between the flat band potential V_{fb} and the open circuit voltage V_{OCP} .

Simulation of the nano-Schottky contact

The simulation of the nano-Schottky contact between Si and metal nanoparticle (NP) follows the model established by Tung [83].

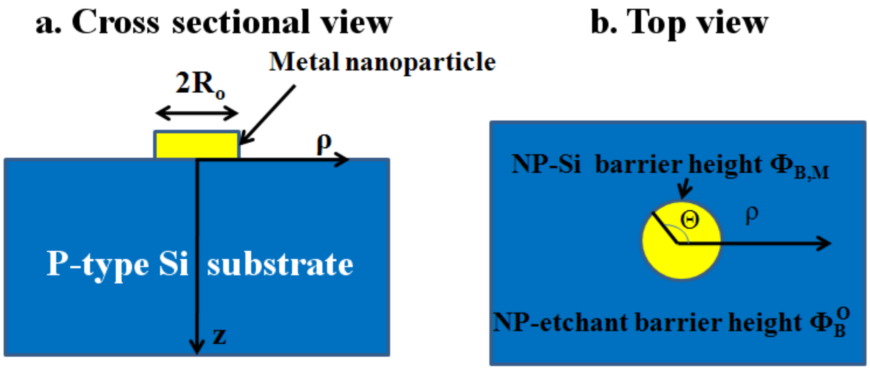

Figure 4.7 Schematics of the metal NP-Si nano-Schottky contact with established cylindrical coordinates (ρ, Θ, z), (a) cross sectional view, (b) top view.

Fig. 4.7 shows the top and cross sectional view of one NP covering the Si substrate, and the established cylindrical coordinates (ρ, Θ, z). R_O is the radius of metal NP. The potential underneath NP inside the semiconductor can be expressed as:

$$V\,(\rho, z) = V_{bb}\left(1-\frac{z}{W}\right)^2 + \frac{\Delta}{2\pi}\int_0^{2\pi}\int_0^{R_o}\frac{\rho_1 z}{[z^2+\rho^2+\rho_1^2-2\rho\rho_1\cos(\Theta_1)]^{3/2}}d\rho_1 d\Theta_1 \text{(e.q. 4.1)}$$

where W is the space charge region width. From ref. [85], Δ can be obtained as, $\Delta = \Phi_B^O - \Phi_{B,M} = V_{OCP/Si-Pt} - V_{OCP/Bare\ Si} = 0.22$ V (see **Fig. 4.8**), where V_{OCP} is the open circuit potential.

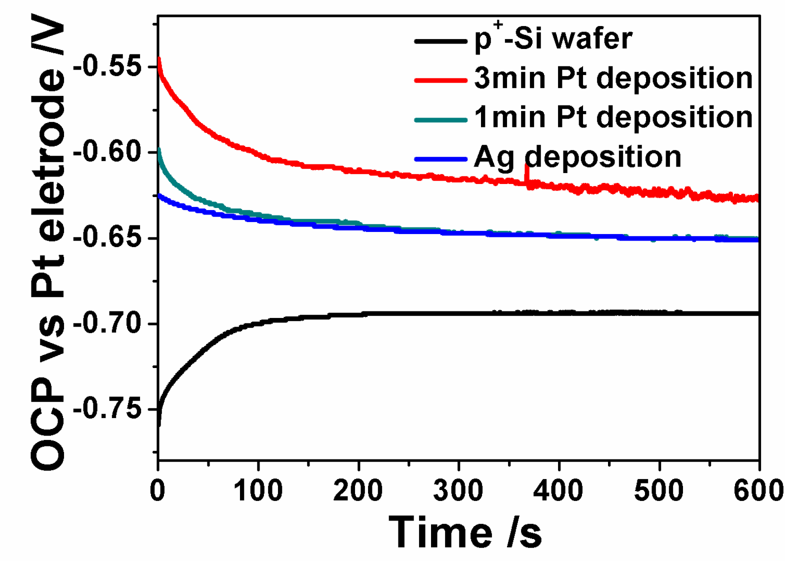

Figure 4.8 Time dependence of OCP for p$^+$-type Si etching with 3 min Pt deposition (red), 1min Pt deposition (green), Ag deposition (blue), and non-treatment (black)

The electrical field can be calculated as: **E**= -grad(V). The space charge region *W* [29] is given by:

$$W = \sqrt{\frac{2\varepsilon_o \varepsilon V_{bb}}{eN_A}} \text{(e.q. 4.2)}$$

where ε_o is the permittivity of free space; ε is the dielectric constant of silicon. Here, *W* ~ 9-16 nm for high doped p-type silicon. For the p-type silicon with resistivity above 1 **Ω** cm, *W* is slightly above *W* = 200 nm. The value of V_{fb} can be extracted from the Mott-Schottky plot [86] as seen in Fig. 4.9, V_{fb}= -0.2 V. Thus, $V_{bb} = V_{fb} - V_{OCP}$ = 0.56 V. Because the HF + H_2O_2 solution would dissolve the Pt electrode and etch the Si substrate, the measurement of the Mott-Schottky plot was conducted in 5 M HF without H_2O_2 to roughly obtain the V_{fb} value.

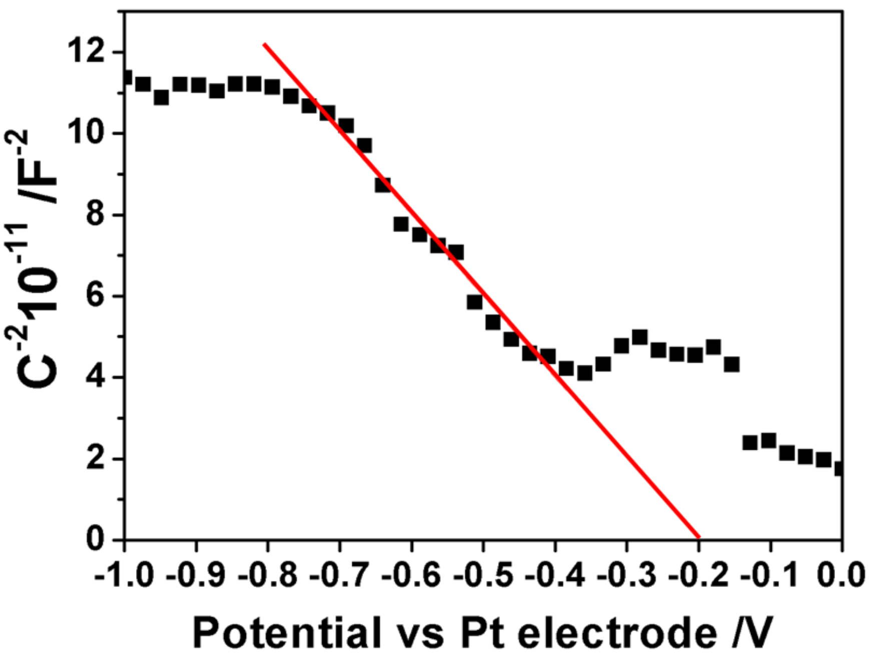

Figure 4.9 The Mott-Schottky plot of high doped p^+-type silicon in 5 M HF solution. The red line is the linear fit by the software.

The simulated electric field distribution is shown in **Fig. 4.10**. Compared to highly-doped Si with a small space charge region (SCR) width (W ~ 9-16 nm), moderately-doped Si with a SCR width W > 200 nm shows more twisted electrical field lines at the NP-Si interfacial boundary. The strength of the electric field at the boundary is enhanced and its direction turns back to the solution side. The holes would not only flow into the vertical direction, but also into the side direction, causing extra Si dissolution (see in Fig. 4.10(d)). In this model, the doping level of the substrate also influence the hole transport over the Schottky barrier of Pt/silicon interface. For moderately-doped p^--type Si, the transport will be dominated by thermionic emission whereas for heavily doped p^+-Si, the transport will be dominated by tunneling [29]. It is expected that tunneling leads to higher local currents and therefore higher dissolutions rates than thermionic emission (the measured values are shown in Fig. 4.12), thus explaining the different porosities and etching rates.

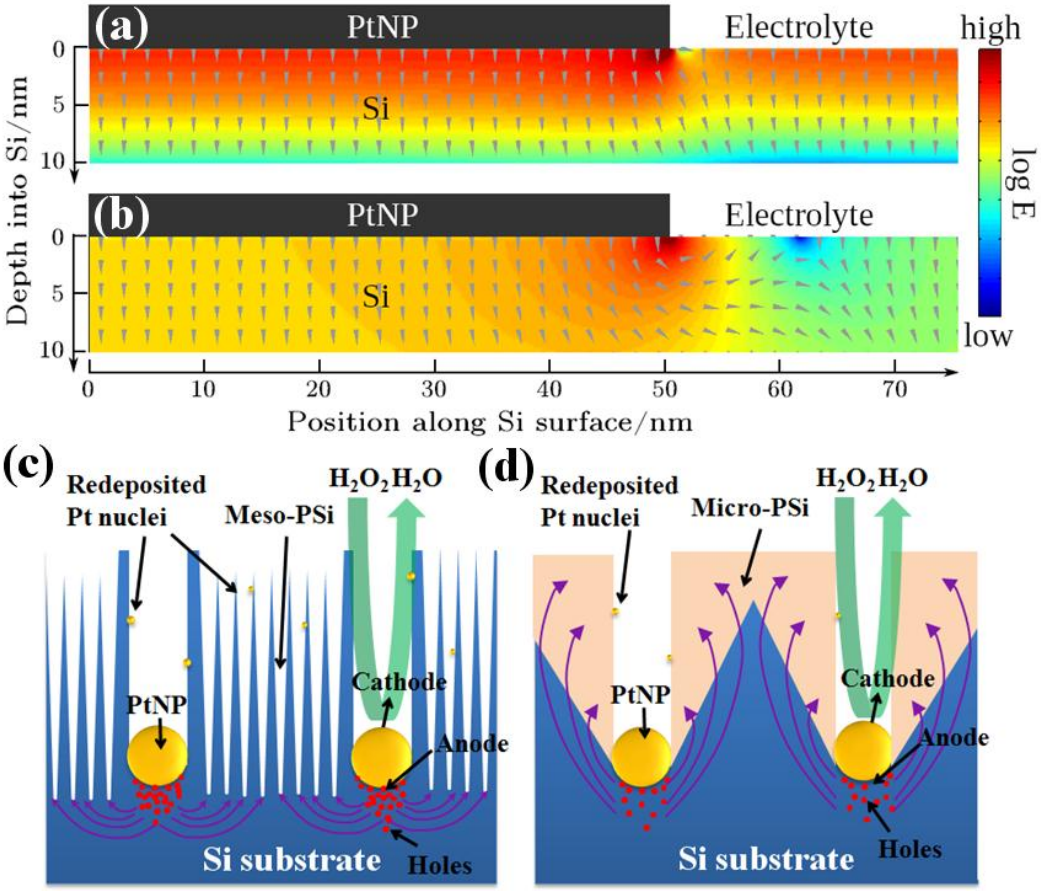

Figure 4.10 (a-b) Simulation of the electrical field distribution of a NP (radius R=50 nm) decorated Si substrate with different SCR width: (a) 12 nm, and (b) 200nm. Schematic of the etching process: (c) Meso-PSi formation in highly doped p^+-type silicon. The purple arrows point to the flow direction of holes, (c) Micro-PSi formation in moderately doped p^--type silicon. The yellow circles are PtNPs. The red circles represent holes (Color version is available online).

This model can also explain why in the case of meso-PSi the pore walls are passivated. For highly-doped Si, holes easily tunnel through the SCR, and then move to the adjacent backside area as sketched in Fig. 4.10(c). This is very similar to electrochemical etching (ECE) with applied bias for supplying holes from the backside. Here, the numerous NP-Si cells act as microscopic electrodes providing an almost uniform anodic bias. According to the well-known ECE theory, d_w is usually constrained to the SCR width due to hole depletion [82,87], or smaller than 5 nm due to quantum size effects [29,88]. Here, the formed meso-PSi are first passivated by the SCR effect ($d_W \sim W$ see Fig. 4.10(d)), and afterwards, the pore walls are laterally etched until the quantum size effect constrains etching due to the redeposited Pt nuclei at the sidewalls.

4.2.2 Understanding the origin of the mobility of PtNPs

It is worth noting that in Fig. 4.2 and 4.3, the etching paths of PtNPs show a strong dependence on the doping level. With the decrease of p-type doping and increase of n-type doping, the etching paths become more curved. Previous literature also reported that if the metal nanoparticles are not densely interconnected, the sparsely distributed metal nanoparticles including Ag [56], Au [57], Pt [58], and Pd [59] sometimes travel in unexpected directions through the silicon. Especially for Pt and Pd, the etching paths are very wavy.

Since the etching direction of metal NPs directly determine the obtained morphology of porous Si, it is critical to understand why the metal NPs show the mobility during etching. Previously, Peng et al. [64] proposed an electrokinetic model to explain the autonomous motion of AgNPs. The electron flow through NPs is coupled with proton translocations in the fluid, which implies an electrical field capable of introducing electrokinetic effects. This model neglects the influence of the Si-metal contact on charge transfer, and cannot fully explain the mobility of metal catalysts.

Here, based on the developed etching model (in Section 4.2.1), we suggest that the mobility of PtNPs was caused by the unbalance of cathodic (j_C) and anodic currents (j_A) in the microscopic PtNP-Si electrochemical cell. The cathodic current equals the holes generated at the cathode; and the anodic current equals the holes transported through the metal-Si Schottky barrier for silicon dissolution. Since Pt can decompose H_2O_2 more effectively than Ag, j_C is greatly enhanced [65].

We suggest that the anodic current j_A plays a crucial role during the investigated etching process. Contributions to j_A consist normally of diffusion, thermionic emission (TE), or tunneling of holes [9]. We estimate the contribution from the diffusion current to be insignificant due to the blocking effect of the surface energy barrier. TE of holes from the metal over the barrier $\Phi_{B,M}$ into the silicon is known as a dominant process for p^- and n^--Si [29]. In the case of p^+-type Si, heavy doping shifts E_F towards E_{VB}, and reduces $\Phi_{B,M}$ further. Moreover, the SCR width is squeezed and the electrical field is magnified in the SCR, allowing the holes to pass the SCR by band-to-band tunneling [89]. It is expected that tunneling leads to higher local currents, and therefore more Si dissolution than TE, thus explaining the PSi structures shown in Fig. 4.2(b) and (c). In contrast, after the deposition of Pt onto n^+-Si, $\Phi_{B,M}$ becomes much higher than that of n^-, p^- and p^+, due to the large work function of Pt [90]. j_A is significantly depressed, and no highly porous structure is produced (see Fig. 4.2(c)).

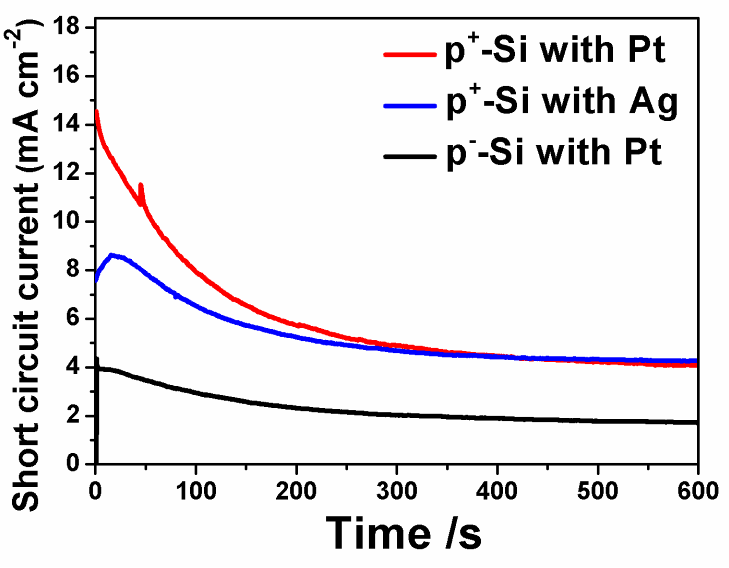

Figure 4.11 Time dependence of short circuit current during etching, p$^-$-Si with Pt deposition (black), p$^+$ with Pt deposition (red), and Ag deposition (blue).

In order to validate the hypothesis, OCP and short circuit current were measured (see Fig. 4.8 and **Fig. 4.11**) by a potentiostat using two Pt wires as the counter and the reference electrode. The actual Schottky barrier difference $\Phi_{B,M}$ - $\Phi_B{}^o$ equals the OCP difference[85]: Δ = $OCP_{Si/Etchant} - OCP_{Si/metal}$. As the value of Δ increases, the barrier height of $\Phi_{B,M}$ decreases. With the increase of PtNP deposition time, Δ also increases. After 3 min of Pt deposition, Δ is 0.22 V for the highly-doped Si, which is larger than the 0.18 V for the highly-doped Si which was almost completely covered with Ag, and the 0.19 V for moderately-doped Si. The short circuit current for highly-doped Si loaded with PtNPs was 3 times higher than that for moderately-doped Si at the starting point of etching, proving the higher tunneling current than that from TE. The reduction of OCP and short circuit current was caused either by the degradation of metal-Si contact [91].

The mobility difference also rises due to the difference in j_A. As previously stated, the high catalytic activity of Pt over Ag generates high j_C. In the case of low $\Phi_{B,M}$ at p^+-type Si, j_A arising from tunneling can effectively accept all holes for etching. However, decreasing the p-type doping would increase $\Phi_{B,M}$, as j_A from TE cannot digest the large amount of holes coming from the cathode. The excessive number of holes which accumulate at the NP-Si interface are then able to attack the Si non-(100) crystal planes with a higher density of silicon back bonds, resulting in a non-<100> etching direction. In the extreme case of heavy n-type doping, the surface barrier is high enough such that the vertical etching is greatly suppressed, and accumulated holes tend to etch silicon in random horizontal directions.

4.2.3 Mechanism of porosity tuning

As previously stated in Section 4.2.1, the PaCE of p^+-type Si has high similarities to ECE, thus the porosity tuning by changing the HF concentration may be explained by the well-known ECE theory. According to the ECE theory [29,92], there is a critical current density j_{PS}, which roughly defines the transition point from the PSi region (anodic current $j_A < j_{PS}$, charge-supply limited) to electropolishing ($j_A > j_{PS}$, chemical-reaction limited). The porosity is proportional to the j_A/j_{PS}. j_{PS} can be calculated as [29]:

$$j_{\mathrm{PS}} = C c_{\mathrm{HF}}^{3/2} \mathrm{e}^{-E_{\mathrm{a}}/(k_{\mathrm{B}} T_{\mathrm{HF}})} \qquad \text{(e.q. 4.3)}$$

where C is a constant value, C_{HF} is the HF concentration, Ea is the activation energy for the reaction, k_B is the Boltzmann constant, T_{HF} is the absolute temperature.

Since $j_{PS} \propto C_{HF}^{3/2}$, decreasing the HF concentration would increase the porosity while keeping j_A unchanged [29]. In other words, the Si dissolution shifts more to the tetravalent electropolishing regime (see eq. 1.5) and the etching becomes more isotropic leading to higher porosity as shown in Fig. 4.5(a). Meanwhile, the etching rate is lowered due to increased dissolution valence. The etching enters the electropolishing region when the HF concentration is smaller than 3 M.

For MaCE of p-type silicon in a solution containing HF and H_2O_2, the cathodic current density j_C can be described by the following equation [93]:

$$j_C = -zek_c n_s C_{ox} \exp\left(-E_a/k_B T\right) \quad \text{(e.q. 4.4)}$$

where z is the number of electrons transferred during the reaction, e is the elementary charge, k_c is the rate constant, n_s is the electron density at the Si/HF/(oxidant agent) solution interface, Cox is the concentration of oxidant (H_2O_2) at the interface, Ea is the activation energy for the cathodic reaction, k_B is the Boltzmann constant and T is the absolute temperature.

Thus, increasing the H_2O_2 concentration would enhance the value of j_C, leading to an increased amount of holes available for injecting into Si. As a result, j_A is enhanced, and the porosity would be increased.

4.3 Summary

In this chapter, we show that MaCE has the strong capability of fabricating micro- and meso-PSi, and the flexibility of controlling the porosity by changing the HF/H_2O_2 concentration. By systematically studying the etching of silicon substrates with different doping levels/types, the charge transfer process between PtNP and Si was unveiled. The morphological difference of porous Si strongly depends on the nano-Schottky barrier height, which was confirmed by the electrostatic simulation. In addition, the interplay between the cathodic j_C and the anodic j_A current in the microscopic electrochemical cell also perfectly explains the origin of the mobility of PtNPs, which is different from previous understanding. Our work provides a facile and cost-effective route to fabricate various PSi structures, which can be easily scaled to wafer size with high etching uniformity. Since the etching area would be no longer constrained by electrochemical cell size, this technique can be directly applied to layer transfer photovoltaics by reducing process complexities and improving the yield.

PEC STUDY OF SINW FOR WATER SPLITTING

5

Applying the fabricated SiNWs for photoelectrochemical (PEC) water splitting is the focus of this chapter. As previously stated in the introduction Section 1.5, the nanowire architecture is able to provide high optical absorption along its axial direction, while facilitating collection of carriers radially over a distance sufficiently short to compensate for short minority carrier collection lengths [94,95]. This key advantage solves the problem of utilizing an antireflective layer (e.g. SiNx, ITO, ZnO) for suppressing the optical reflectance, since these antireflective layers would either inhibit the electron transfer or dissolve in the acidic electrolyte. Furthermore, the reduced carrier collection length would improve the photocurrent and allow the use of low-grade inexpensive metallurgical Si.

Until now, several publications have reported that nanostructured Si including nanoporous and nanowired Si showed both enhanced photocurrent and more than 400 mV anodic on-set potential (V_{OS}) shift for the H_2 evolution reaction (HER) in sulfuric acid electrolyte [96,97]. However, the enhancement of photocurrent by Si nanostructures varied in a wide range. Oh et al. reported that the saturated photocurrent (J_{ph}) of nanoporous Si (Au assisted etching) was ~1.2 times higher than that of planar structures [94]. The ratio was ~1.58 for nanoporous Si (Ag assisted etching) reported by U. Sim et al. [98], and 1.2 for nanowire (Ag assisted etching) reported by Huwang et al. [96]. In addition, there has been controversy in the literatures regarding on the origin of the anodic V_{OS} shift. It was hard to conclude whether the V_{OS} shift is due to the flat band potential change [96], the surface area increase [97], or other possible factors. Furthermore, even with some theoretical calculations [95], none of the reports have demonstrated how to design nanostructured Si photoelectrodes specifically for the HER.

Herein, we systematically study various factors including metal impurities, etching time and Ag coverage on the PEC performance in Section 5.1.1. We design a simple process by applying a post KOH etching process of SiNWs in Section 5.1.2. This strategy is able to reveal the HER mechanism of nanostructured Si due to three major effects caused by KOH etching. Firstly, post KOH etching removes the defects at SiNW surfaces allowing us to investigate how the surface defects which originate from fabrication process influence the PEC performance. Secondly, through carefully tuning the KOH etching time, the surface roughness can be exactly controlled. Thus, the effect of surface roughness on PEC performance can be easily revealed. Finally, post KOH etching would shrink the SiNW size, and generate tapered SiNWs, enabling us to study the surface and shape effect on the HER. The detailed mechanism is discussed in Section 5.2. Furthermore, in association with optical measurements and simulations, we find that tapered SiNW is an optically and electrically perfect candidate for the HER.

5.1 PEC performance of SiNWs

5.1.1 Effect of NW construction and metal impurities

The optical properties of UMG-SiNW and EG-SiNW were measured firstly. Since the UMG-SiNWs are slanted in different angles due to various crystallographic orientations of UMG-Si, the upper parts of slanting NWs reflect more incoming light than vertical EG-SiNWs (see Section 3.1 and 3.2). From the total reflectance spectra (see **Fig. 5.1**), the reflectance of UMG-SiNW (MaCE 5 min) is ~5- 6% in the wavelength range from 300 to 1000 nm, which is roughly 2% higher than that of EG-SiNW with the same etching time. Extending the MaCE time would increase the NW length resulting in the increased optical paths. Therefore, UMG-SiNW with 15 min etching shows slightly lower reflectance. However, UMG-SiNW with etching time more than 30 min would increase the reflectance due to agglomeration of SiNWs.

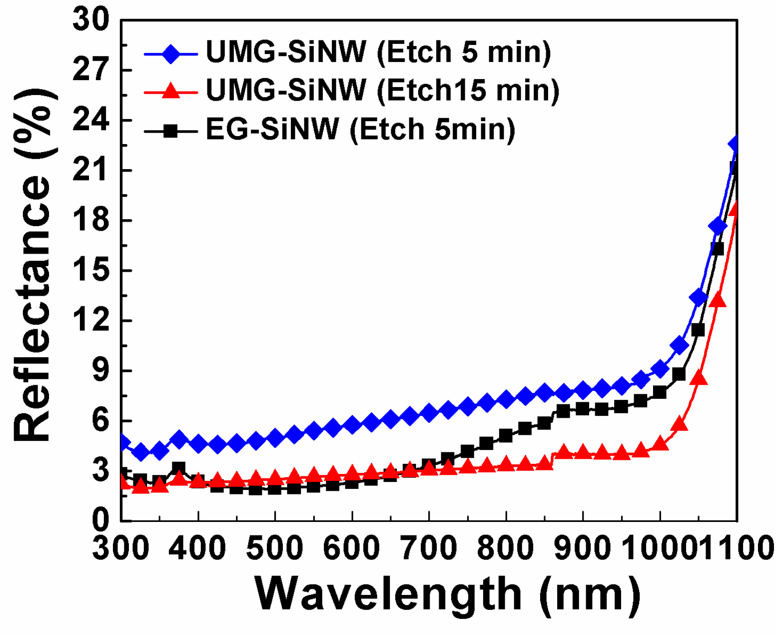

Figure 5.1 Total reflectance spectra of UMG-SiNW etched for 15 min on the non-polished as-cut wafer (orange circle), UMG-SiNW etched on the polished surface etched for 5 min (blue diamond), 15 min (red up-triangular), 30 min (Cyan down-triangular), and EG-SiNW etched for 15 min (black square).

Fig. 5.2(a, b) shows the schematics of the SiNW based PEC cell. As stated in the introduction part Section 1.5, a space charge region (SCR) is built at the interface between Si and electrolyte. The photocurrent generation is mainly due to the electric field within the SCR which can rapidly separate photogenerated carriers.

Fig. 5.2(c) compares the photocurrent density-potential (J-V) behavior of EG-SiNW, UMG-SiNW (etched for 5 min) and their planar counterparts. The J_{ph} of EG-SiNW just shows slight enhancement than that of the planar counterpart. In contrast, the photocurrent density of the UMG-SiNWs shows a 35% increase in photocurrent in comparison to the UMG-Si wafer. Interestingly, the onset potential V_{os}, shows an anodic shift of 200 mV in the UMG-SiNWs in comparison to the polished UMG-Si wafer (Fig. 4(d)). For the EG-SiNWs, this shift is greater than 400 mV.

With increasing etching time of the UMG-Si, the dark current is reduced linearly (see Fig. 5.2(c,d)). On the contrary, such a decrease in dark current was not observed for the EG-SiNWs. By contaminating EG-Si with metal impurities such as Cu and Ag, a significant enhancement of dark current is found as shown in **Fig. 5.3**. Therefore, we speculate that this phenomenon is due to the successive removal of metal impurities in UMG-Si as described in Section 3.2, and that the material quality is improved.

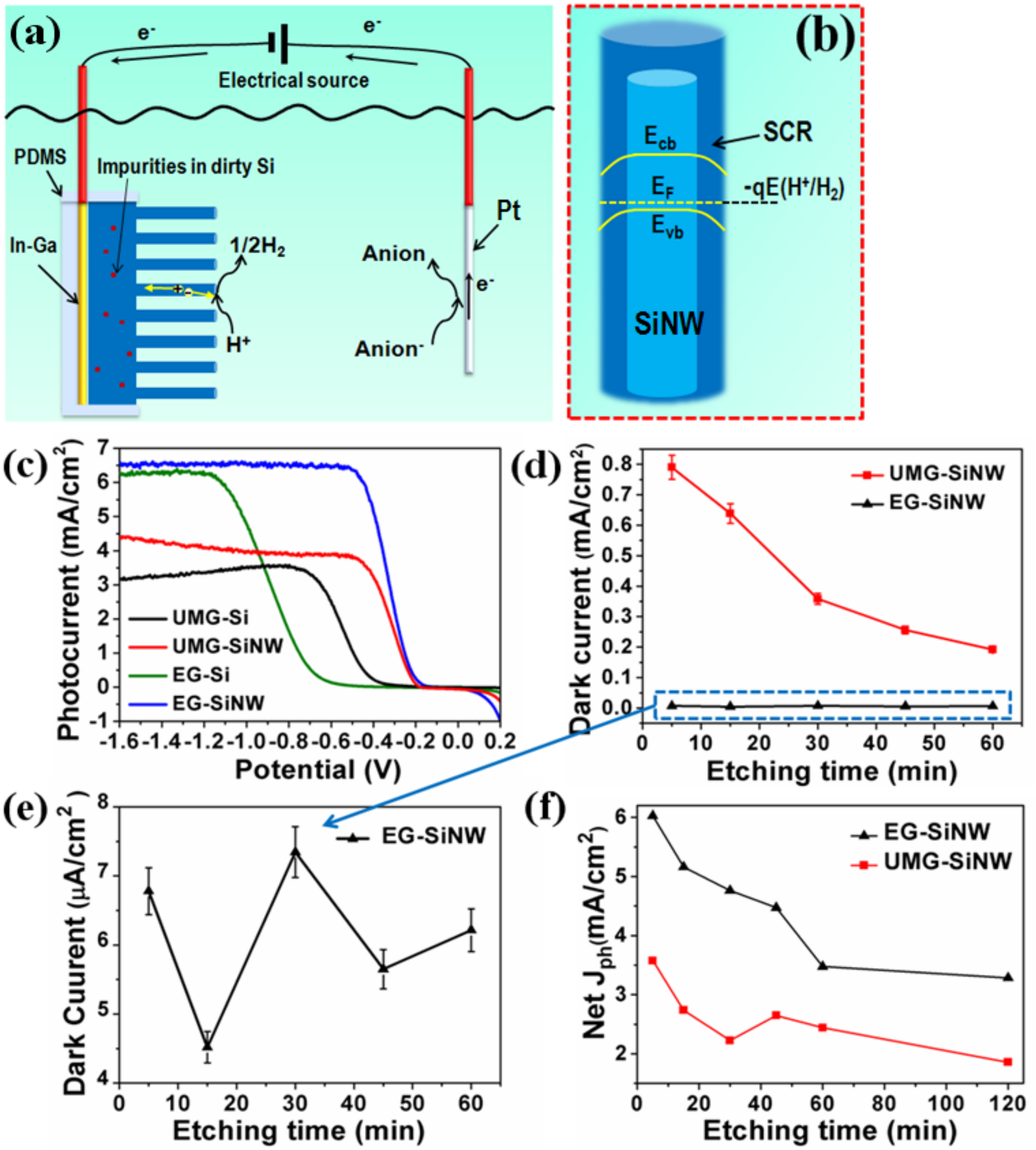

Figure 5.2 (a) Schematic diagrams of a PEC cell using p-type UMG-SiNW as a photocathode for hydrogen evolution. (b) Band bending and space charge region (SCR) formation of UMG-SiNW after immersing into the electrolyte. (c) Photocurrent densities (J) versus potential (V) curves under simulated solar illumination of EG-Si wafer (Cyan), EG-SiNW (5 min etching) (Blue), polished UMG-Si (Black), and UMG-SiNW (5 min etching) (Red). (d) Dark current density versus etching time curve of EG-SiNW (enlarged plot from (c)). (e) Net J_{ph} versus the etching time.

However, despite the decease of dark current, the net J_{ph} (which equals J_{ph} minus dark current density) of UMG-SiNW meets a reduction with the increased length of nanowire by prolonging the etching time. Such a decrease is also observed in EG-SiNW (see Fig. 5.2(d,e)). As described before, increasing the NW length reduces the reflectance. Thus, we conclude that J_{ph} is not closely related to the light absorption; instead, it is correlated to the increased surface area, which will be discussed in Section 5.2.

Fig. 5.4 compares the stability of photocurrent during the cycling of MaCE purified UMG-SiNWs and planar UMG-Si. The UMG-SiNWs exhibited a better stability than their mother substrate (planar UMG-Si), which proves that during water splitting NW structures likely tolerate oxidation more than the planar structure does.

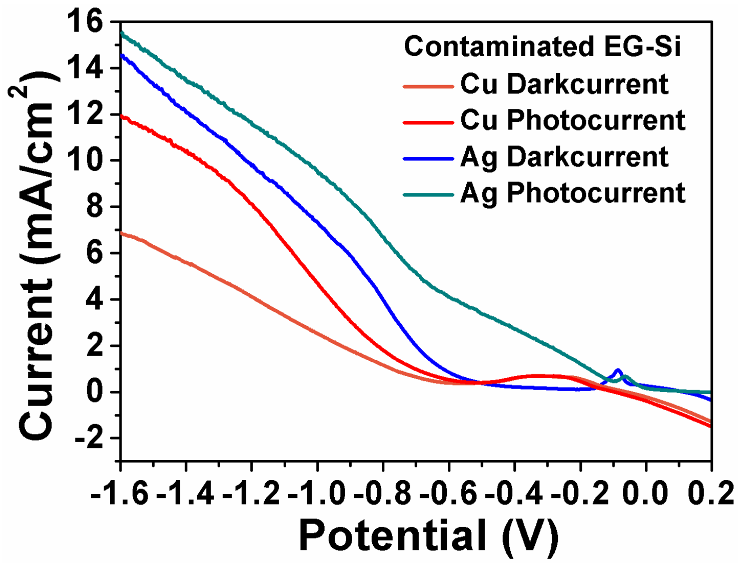

Figure 5.3 I-V characteristics of EG-Si contaminated with Cu and Ag. The contamination was done by annealing 5 nm metal layers at high temperature in N_2 atmosphere.

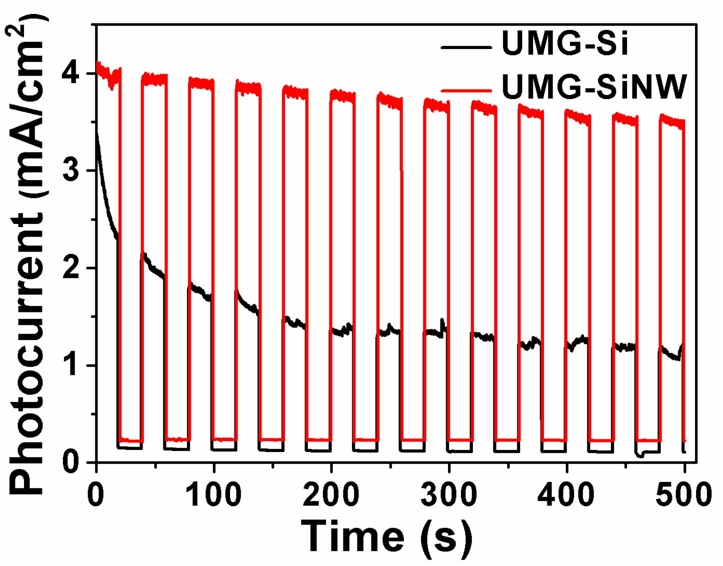

Figure 5.4 (a) Photocurrent response of the UMG-Si (Black) and the UMG-SiNW (Red) versus ON-OFF cycles of illumination at a potential of -0.6V.

5.1.2 Effect of post-KOH etching

Fig. 5.5 shows the morphological changes of SiNWs with the increase of post KOH etching time. The original SiNWs were agglomerated together due to Van der Waal forces. From the tilted SEM image in Fig. 5.5(a), some etching defects i.e. tiny pores can be observed. After KOH etching (30 s), SiNWs were sharpened, and well separated. Such tapering processes are mainly due to the higher etching rate in the <110> direction over the <100> direction at the top of the SiNWs [28]. SiNWs with small diameters (~50 nm) can be easily removed during this process. Increasing the KOH etching time leads to a continuous dissolution of SiNWs and a rapid decrease of areal density of SiNWs. Tapered SiNWs would disappear after 90 s etching, leaving behind a rugged Si surface. Fig. 5.5(e) shows the anodic scanning current-voltage (J-V) curves of Si samples. Because the anodic Si oxide formation at the SiNW surfaces is a surface-limited process, the anodic charges passing through the NW surfaces during the anodic passivation are proportional to the surface area [96]. A possible measure of the surface roughness γ is:

$$\gamma = A_{Nano}/A_o = C_{Nano}/C_{Planar} \qquad \text{(e.q. 5.1)}$$

where A_{Nano} is the surface area of the SiNW/electrolyte interface, A_o is the projected area defined by sealing (γ =1 for planar Si), C_{Nano} and C_{Planar} are the anodic charge passed through the SiNWs and the planar Si respectively during anodic oxidation. The anodic charges can be calculated by integrating the J-V curve. **Fig. 5.6**(c) shows the relationship between the obtained γ value and the post KOH etching time. γ decreases linearly with the etching time from 13.6 (original SiNW) to 4.1 (SiNW with 90 s KOH etching).

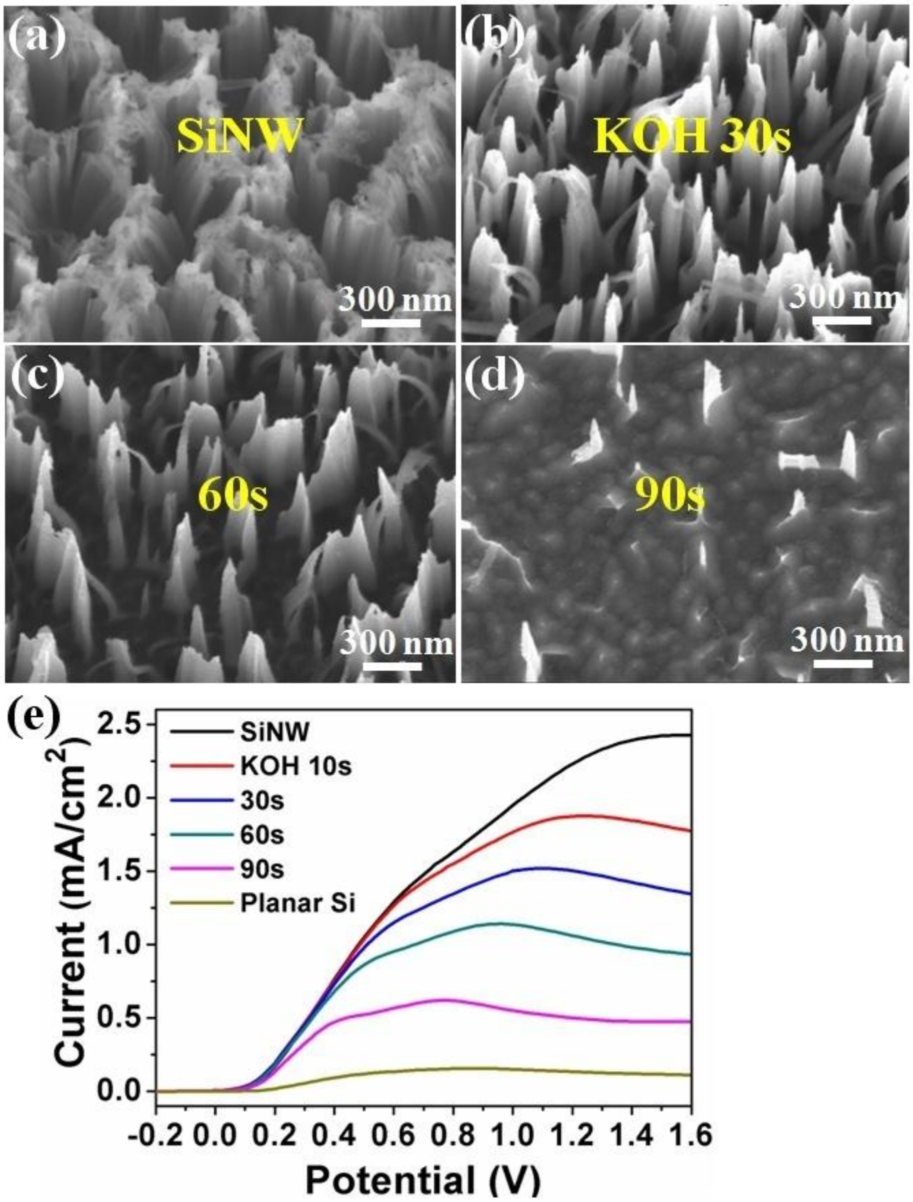

Figure 5.5 Tilted SEM views of SiNWs with different post KOH etching times (a) 0 s (b) 30 s (c) 60 s (d) 90 s. (e) Linear anodic scanning of Si samples in a H_2SO_4 electrolyte.

The reflectance of SiNWs demonstrates a strong dependence on the post KOH etching time. Even with a significant decrease of density and surface area of the SiNWs after the post KOH etching, the averaged light absorption loses only 1.6% for 20 s etching, and 7.1% for 30s etching. In the near UV region (300-450 nm), tapered SiNWs (10-20 s etching) exhibits a lower reflectance than a not etched one. The main reason is that the sharpening process of SiNWs leads to a gradual volume fraction increase towards the root of SiNWs, inducing the graded refractive index effect. The refractive index mismatch was lowered to a minimum at the interface between the tapered SiNW layer and the substrate. We also simulated SiNWs and tapered ones with the same height and density (see simulation details) using the commercial software COMSOL Multiphysics. In the simulations, the two kinds of nanostructures are approximated as periodic Si nanorods (SiNRs) and nanocones (SiNCs) respectively. The intermediate state between SiNWs and SiNCs is the Si nanofrustrum (SiNF). According to the reflectance curves seen in Fig. 5.6(d), SiNCs show much lower reflectance than SiNWs and SiNFs in a range of 300-1100 nm. The reflectance spectrum of SiNCs becomes smoother compared to the case of SiNWs due to a better refractive index matching between air and Si substrate.

The reflectance of SiNWs in the near infrared (NIR) range (1200-2200 nm) was also measured experimentally as shown in Fig. 5.6(b). Interestingly, there is a gradual increase of NIR light reflectance with the post KOH etching time. Since the sub-bandgap light absorption is mainly due to the high density of surface defect states [99], the NIR light reflectance increase points to the removal process of surface defects by KOH etching.

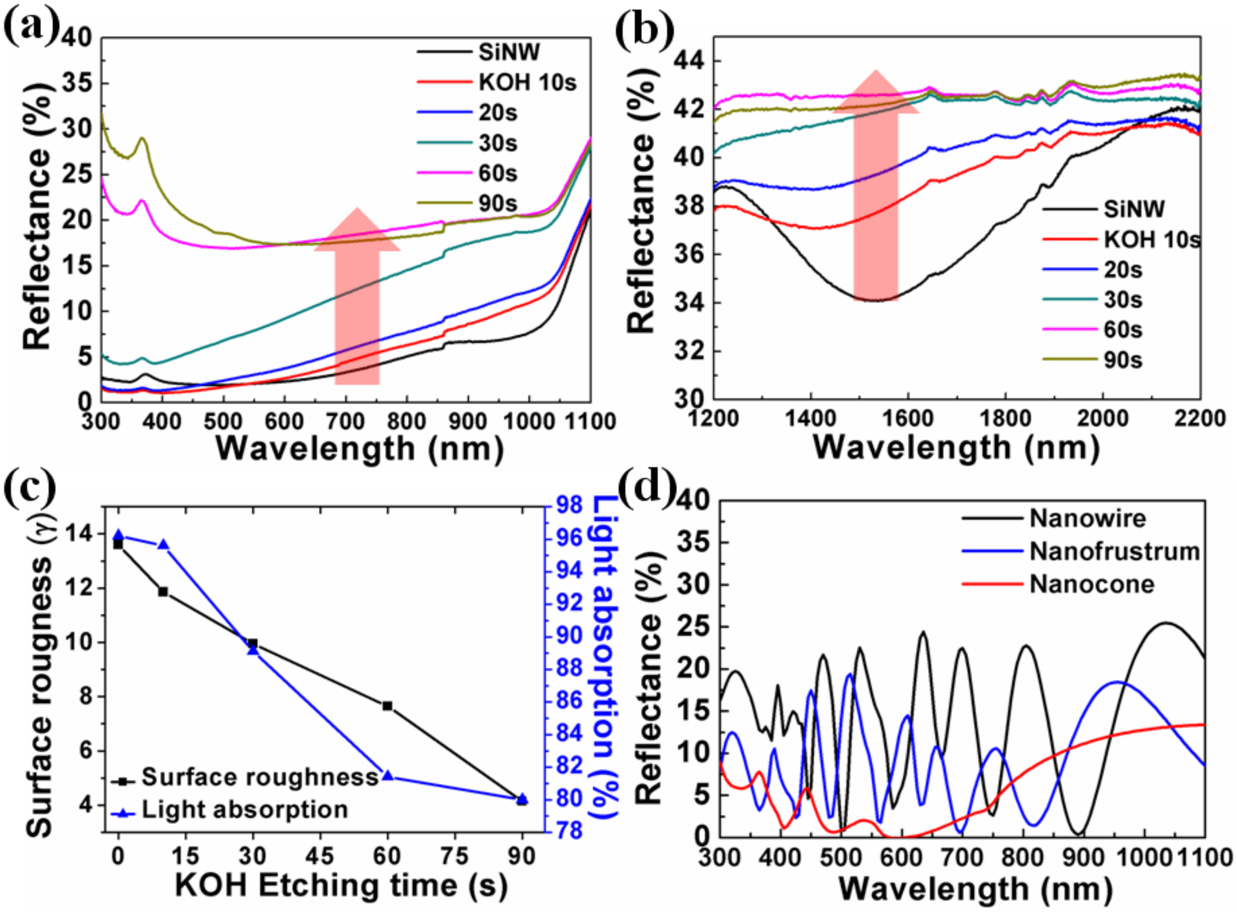

Figure 5.6 Total reflectance spectra of SiNWs with different post KOH etching time in the wavelength range of (a) 300-1100 nm, (b) 1200-2200 nm. (c) Dependence of surface roughness and light absorption on the post KOH etching time. (d) Simulated reflectance spectra of silicon nanowires, nanofrustums and nanocones. The detailed geometric parameters are given in the end of the chapter.

5.2 Discussion of results

5.2.1 Effects of light absorption and surface defects on the J_{ph}

Fig. 5.7(a) shows the PEC performance of planar Si and SiNWs after different KOH etching times. The original SiNWs (MaCE for 5 min) shows a ~15% increase in J_{ph} compared to its planar counterpart in addition with a 400 mV anodic shift of Vos, agreeing with previous reports. Interestingly, after post KOH etching for 10 s, the J_{ph} increases more than 23% than that of planar Si, and the V_{OS} shows a 500 mV anodic shift. The J-V curve is shifted more positively by prolonging KOH etching to 30 s without changing the J_{ph} value. Further increasing the KOH etching time degrades the PEC performance.

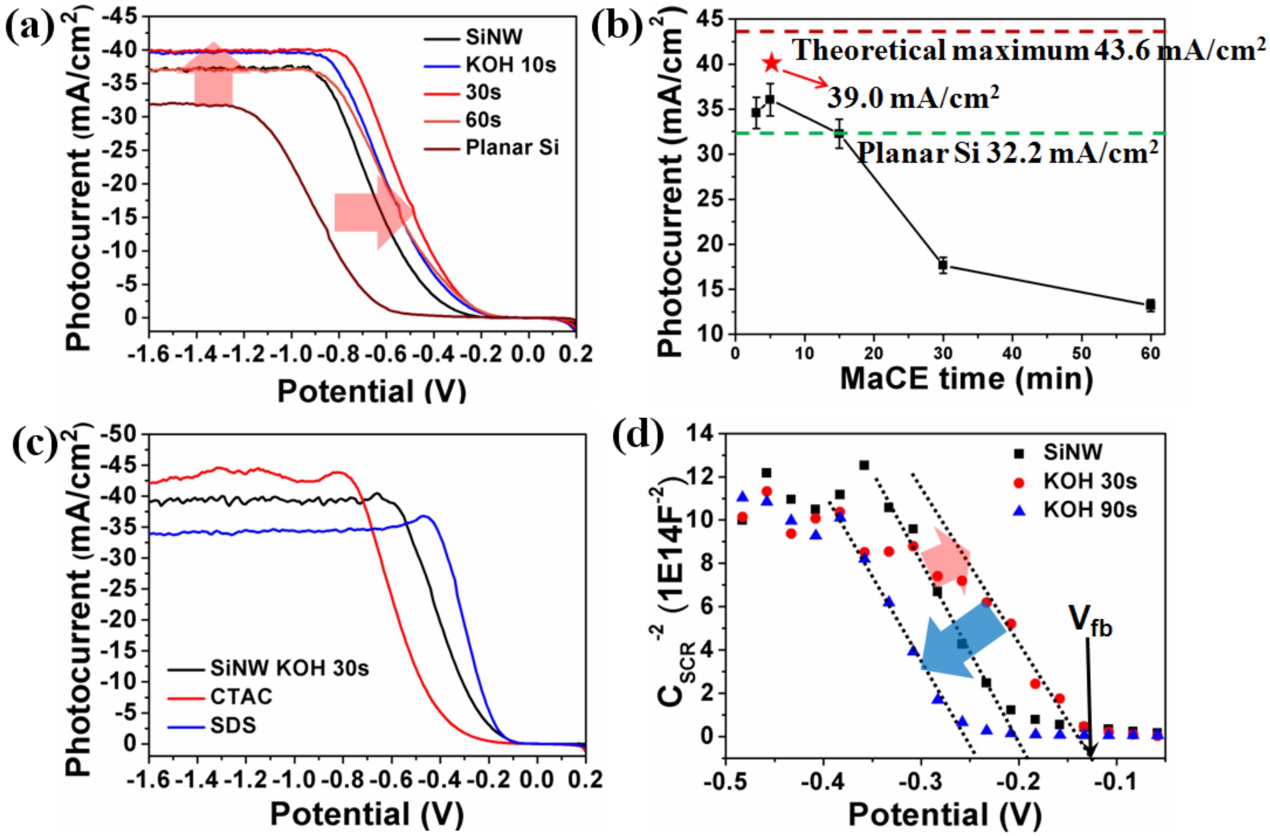

Figure 5.7 Photoelectrochemical (PEC) J-V curves of planar Si and SiNW after different post KOH etching times measured under 1 sun illumination. (b) Saturated photocurrent value versus MaCE etching time of SiNW. The red star represents the saturated photocurrent value of SiNW after 30 s KOH etching (39.0 mA/cm^2). The dashed dark red line represents the theoretical maximum of photocurrent (43.6 mA/cm^2). The dashed green line represents the saturated photocurrent value of planar Si. (c) PEC J-V curves of SiNWs after 30 s KOH etching measured with different surfactants: CTAC (red) and SLS (blue). (d) Mott-Schottky plot of SiNWs after different post KOH etching times (measured at 1000 Hz): original SiNWs (black square), KOH 30 s (red circle), and KOH 90 s (blue triangular).

Previous understandings on photocurrent enhancement are mainly ascribed to the strong light absorption [96,97]. However, after 60 s post KOH etching, the tapered SiNW sample lost ~20% light absorption, but the J_{ph} remained the same as that of the original SiNWs. This phenomenon reveals that most of the photon generated electrons and holes in SiNWs are not effective participating in HER, instead, they quickly recombine at the interface of the electrolyte and the SiNW due to a high surface recombination velocity S. The value S is related to the photogenerated minority carrier lifetime τ [100,101]:

$$\frac{1}{\tau} = \frac{1}{\tau_{\mathrm{Bulk}}} + \frac{S}{2d} \approx \frac{S}{2d} \qquad \text{(e.q. 5.2)}$$

where τ_{Bulk} is the bulk lifetime of photogenerated minority carriers, which can be assumed to be infinite for high quality Si material; d is the sample thickness.

Assuming Shockley-Read-Hall recombination processes, S is related to the density of surface defect states [100]:

$$S = \nu_t \sigma N_{ss} \gamma \text{(e.q. 5.3)}$$

where υ_t is the carrier thermal velocity, σ is the trap cross section, Nss is the microscopic density of surface defects per unit surface area.

Through eq. (2) and (3), we derived the ratio of surface defect density between SiNWs (N_{ssNano}) and planar Si ($N_{ssPlanar}$):

$$\frac{N_{\mathrm{ssNano}}}{N_{\mathrm{ssPlanar}}} = \frac{S_{\mathrm{Nano}}}{\gamma S_{\mathrm{Planar}}} = \frac{\tau_{\mathrm{Planar}}}{\gamma \tau_{\mathrm{Nano}}} \text{ (e.q. 5.4)}$$

Fig. 5.8 shows the measured carrier lifetime of planar Si (~222.4 μs) and SiNWs (~12.0 μs) chemically passivated with hydrogen by an HF dip. The surface defect density per unit surface area of the SiNW sample is calculated to be ~1.36 times higher than that of the planar Si according to eq. 5.4. The formation of these defects during MaCE is possibly due to the dissolution of Ag catalysts and the subsequent renucleation of tiny Ag particles at the SiNW sidewalls during MaCE. Thus, extending the etching time significantly degrades the photocurrent due to the increased surface defect density. In addition, since the SiNW top is exposed to the etchant for the longest time compared to other parts of the SiNWs, the areal density of surface defects (i.e. tiny pores seen in Fig. 5.5(a)) at the top is the highest. By taking advantage of the anisotropic properties of KOH etching, these defects can be effectively removed, which is confirmed by the NIR light reflectance change. As a result, the photocurrent is improved.

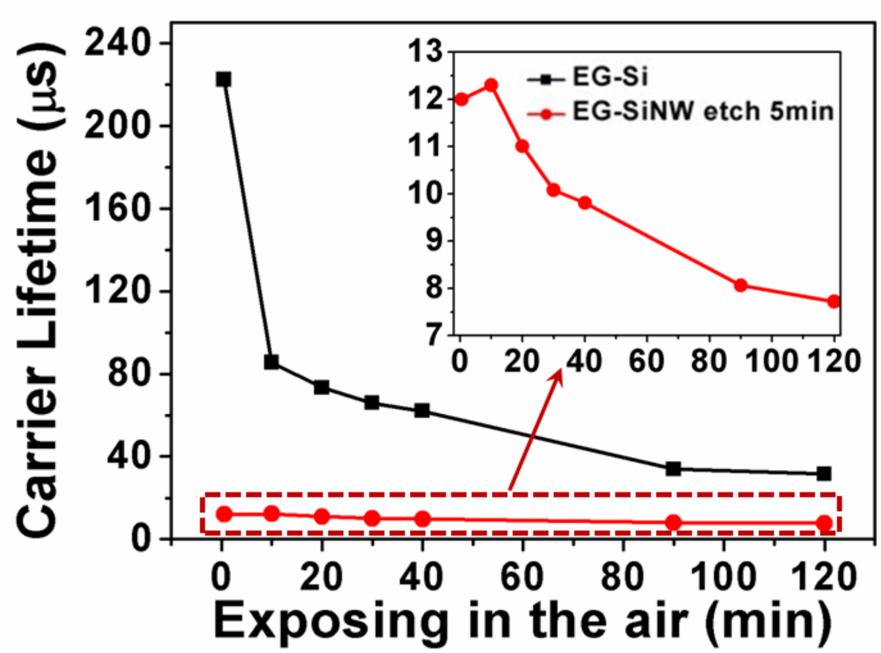

Figure 5.8 Lifetime versus exposing time in air after HF dipping. Planar EG-Si(100) wafer (Black square), EG-SiNW etched for 5 min (Red circle).

5.2.2 The origin of the V_{OS} anodic shift

The most interesting finding in this chapter is that even though the surface area is reduced, tapered SiNWs show a larger shift of the V_{OS} (see Fig. 5.7(a)). This finding solves the key controversy on the origin of the V_{OS} shift: Through providing additional sites for the HER, nanostructured Si with high surface areas can lower the required overpotential. Here, we propose that the V_{OS} shift can be ascribed to the increased surface effect.

The key advantage of NW based PEC is the conformal radial charge-separation at the interface of the NWs and the electrolyte. Thus, the perquisite is that SiNWs with diameters of tens of nanometers should be larger than twice the width of the space charge region (W_{SCR}). Therefore SiNWs can support an internal electric field caused by band bending. Otherwise, full depletion of NWs would deteriorate the PEC performance both in photocurrent and photovoltage. W_{SCR} depends on the potential drop in SCR (V_{SCR}) and the doping level of the Si substrates [102],

$$W_{SCR} = \sqrt{\frac{2\varepsilon_o \varepsilon V_{SCR}}{eN_A}} \qquad \text{(e.q. 5.5)}$$

where ε_o is the permittivity of vacuum, ε is the dielectric constant of Si, e is the elementary charge, and N_A is the doping concentration. The value of V_{fb} can be extracted from the Mott-Schottky plot shown in Fig. 3(d). Thus, the value of V_{SCR} is obtained as $V_{SCR} \approx V_{app} - V_{fb}$. V_{app} is the applied potential.

Based on the equation 5.5, the W_{SCR} is estimated to be 220 nm for the original SiNWs, and 310 nm for SiNWs after 30s KOH etching time at a small applied potential $V_{app} = -0.3$ V. Herein, the much improved PEC performance by nanostructuring proves that these SiNWs should not be full depleted. Thus, we speculate that the surface effect in SiNWs plays a critical role in increasing the p-type doping inside SiNWs. Such an increase would consequently reduce the SCR width, and modulate the internal band bending in the SiNWs.

It has been reported previously that due to ‘electron pulling’ by the terminating hydrogen, electrons transfer from the Si core to the surface and change the band bending at the surface [103]. This charge transfer is negligible for bulk silicon but is significant for surface-dominated SiNWs with carrier concentrations that are considerably higher. SiNWs with surface passivant hydrogen atoms would exhibit an increased hole concentration. This phenomenon is indeed observed in our experiments. Through post KOH etching, the obtained tapered SiNWs have higher surface-to-volume ratios than the original SiNW. The hole concentration of tapered SiNWs would be more enhanced than before. As illustrated in **Fig. 5.9**(a), the surface band bending would be stronger, producing a high photovoltage. This explains the anodic shift of V_{OS} and V_{fb} that was observed in Fig. 3(a) and (c). If the post KOH etching exceeds more than 60 s, the surface-to-volume ratio of SiNWs decreases, and the V_{OS} and V_{fb} shifts cathodically.

For the further verification of our concept, two kinds of surfactants including anionic surfactant sodium dodecyl sulfate (SDS) and cationic surfactant cetyl trimethyl ammonium chloride (CTAC) were added to the electrolyte. Fig. 5.7(c) shows their influence on the PEC performance.

SDS shifts the J-V curve even more anodically, and CTAC shifts in the opposite cathodic direction. Fig. 5.9(c, d) shows the band bending change induced by surfactants. For SDS, its alkyl tail would adsorb at the NW surface, and the negative charged head group would point to the solution side. According to a previous report [104], positive surface dipoles form at the Si surface under such circumstances. These positive dipoles attract electrons to the SiNW surface causing enhanced downward band bending. In contrast, for CTAC, surface band bending in SiNWs is weakened due to the formation of negative surface diploes. The addition of surfactants also influences J_{ph}, CTAC improves the photocurrent to ~42.5 mA/cm^2, approaching the theoretical limit. On the contrary, SDS reduces the photocurrent to ~32.5 mA/cm^2. This phenomenon suggests that the surfactants not only own the ability to change the band bending, but also have the possibility to reduce or increase the surface recombination. The detailed study of the passivation mechanisms by surfactants is currently ongoing.

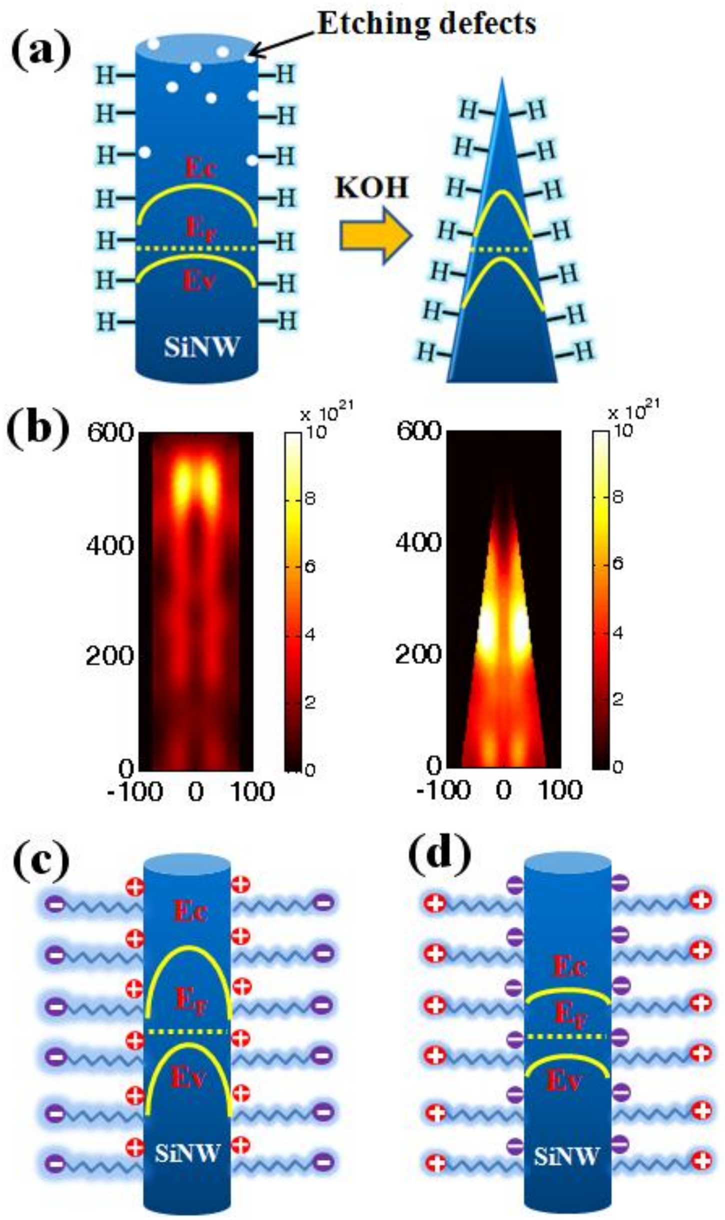

Figure 5.9 (a) Schematic diagram of the SiNWs tapering process by post KOH etching. H represents the hydrogen termination. E_C, E_F and E_V are the conduction band, Fermi level and valence band of Si, which are marked as yellow line. (b) Calculated electron generation rates for straight SiNWs and tapered SiNWs under one AM 1.5 solar irradiation. Schematic diagrams of (c) anionic and (d) cationic surfactants on the band bending in SiNWs. Purple and red circles represent negative and positive charges, respectively.

5.2.3 Design considerations for solar water splitting applications

To understand the superior performance of tapered SiNWs, we simulated the electron generation rates (EGR) throughout the structure and demonstrated their distribution in the cross-section through the center of SiNWs and tapered ones (see in simulation details at the end of this chapter). As shown in Fig. 5.9(b), the electron generation rate (EGR) in tapered SiNWs (in simulation approximated as SiNCs) is on average ~40% higher than that in original SiNWs. More interestingly, we find that the strongest EGR region ($\sim 8\times 10^{21}$ electrons per cm^3) is located at the top of SiNWs, where many etching defects existed and acted as recombination centers. In contrast, the strongest EGR region for tapered ones is located at the upper middle region ($\sim 1\times 10^{22}$ electrons per cm^3), well matching the strong band bending shown in Fig. 5.9(a). As a result, the photocurrent of tapered SiNWs is much higher than that of SiNWs, which is in accordance with our experimental data. Once the surface is properly passivated, the photocurrent can easily almost achieve close to the theoretical limit ~43.6 mA/cm^2. In the case of designing highly efficient nanostructured Si based water splitting devices, the high EGR region should couple with the enhanced band bending while avoiding the defect region in nanostructures. For commonly used Si nanostructures by MaCE or RIE, we strongly suggested removing the top part of nanostructures where there are lots of surface damages and etching defects.

5.3 Summary

In this chapter, we investigate the PEC water splitting properties of SiNWs as photocathode. Compared with planar Si, SiNW structures show an enhanced photocurrent (~15% increase) and an anodic shift of V_{OS}. For UMG-Si, after the construction of SiNWs, the photocurrent increases more than 35% due to an additional successive metal impurity removal. In order to further improve the photocurrent and understand the mechanism of PEC performance enhancement, we employ a simple approach to tune the surface area and shape of SiNWs by applying post KOH etching. We find that controlling the surface defect density is critically important for achieving a high photocurrent instead of pursing excellent light absorption in nanostructured Si. Post KOH etching can effectively remove the defects without sacrificing much light absorption. The tapered SiNWs with shrunk sizes after KOH etching also provide direct evidence that the anodic shift of V_{OS} is due to the surface effect. Changing the passivants or adsorbates (i.e. anionic and cationic surfactants) at the NW surface can modulate the surface band bending of SiNWs. Combining theoretical simulations and the experimental approach, we prove that tapered SiNW is an excellent candidate for photoelectrochemical HER. With careful surface passivation, the efficiency of tapered SiNWs can achieve the theoretical limit.

Simulation details:

A three dimensional finite element method (FEM) simulation is performed using a commercially available FEM package (COMSOL Multiphysics 4.2a). Truncated cones are periodically distributed in a square lattice manner. The period, bottom diameter and height of the truncated cones are fixed to be p=200 nm, d=150 nm and h =600 nm, which are chosen to be similar to our experimental data. In our modeling, the top diameter (t) is varied to form different geometries. When t approaches 0, we have an explicit nanocone array; when t equals to d = 150 nm, we have a Si nanowire array; when $0<t<d$, it is a nanofrustum array. The schematics are shown in Fig. S3.

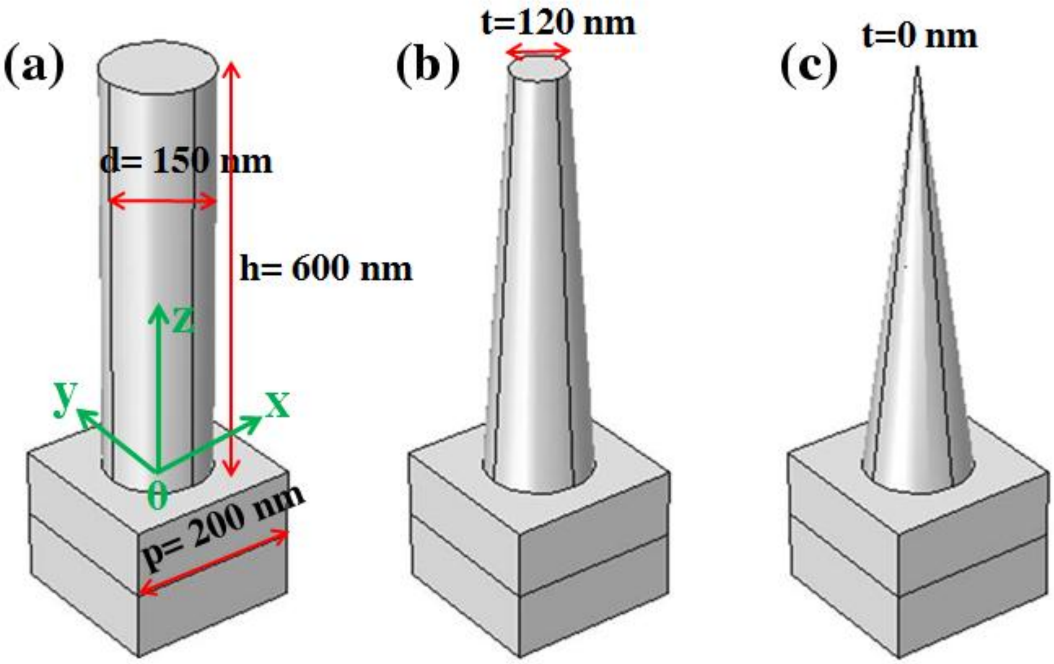

Figure 5.10 Schematic representing Si nanowire, nanofrustrum and nanocone.

In the simulations, only one unit cell is considered in which only one nanocone is included. The incident light is set to be x-polarized propagating along the –z axis. Boundary conditions of perfect magnetic conductors (PMCs) were used for y=-p/2 and y=p/2 planes, and perfect electric conductors (PECs) conditions were used for the other two planes, x=-p/2 and x=p/2. Perfect matched layers (PMLs) were used at the top and bottom of the unit cell and ended with the scattering boundaries. The reflectance is determined by:

$$R = 1 - \frac{\iint P_z dxdy}{E_{in}}$$

in which Pz is the is the averaged power flow in a probe plane in front of the cell and E_{in} is the total energy of the incident light in each cell. The electron generated rate is calculated using the following spectral weighted integration

$$EGR = \int \frac{\varepsilon"|E|^2}{2\hbar}\Gamma_{solar}(\lambda)\,d\lambda$$

in which $\varepsilon"$ is the imaginary part of permittivity, E is the calculated electric field, and $\Gamma_{solar}(\lambda)$ is the AM1.5 solar irradiance spectrum. The EGR reveals the number of electrons that are generated in a specific position per second.

6

CONCLUSION REMARKS AND OUTLOOK

6.1 Concluding remarks

In this thesis, we achieve three major approaches in nanofabrication by MaCE and application of Si nanostructures for PEC water splitting. Fig. 6.1 shows the final overview of the obtained results:

(1) Large areas of SiNWs were fabricated from UMG-Si and MG-Si. Compared with EG-SiNW or SG-SiNW, some UMG-SiNWs showed local line etching defects. For MG-Si with much higher metal impurity concentration, MG-SiNWs was not solid; instead they demonstrated uniform porosity inside SiNWs. During the fabrication of UMG-SiNWs and MG-SiNWs, the metal impurities inside ‘dirty’ Si can be effectively removed. The purification is superior over traditional acid leaching methods: from 99.74 to 99.9884% for the MG-Si powder, and from 99.999772 to 99.999899% for the UMG-Si wafer. This approach opens a new way for upgrading UMG-Si and MG-Si to solar grade Si. This room temperature etching technique also can be easily scaled up for mass production. We believe MaCE would possibly emerge as a new cost-effective route to upgrade MG-Si to solar grade while skipping the ‘Siemens process’ in the near future.

(2) Through PtNP assisted chemical etching (PaCE), we have successfully fabricated meso-PSi with high uniformity. Etching rates exceeding 1.7 μm/min have been obtained under optimized conditions. Since PaCE can be easily scaled to wafer size, and the etching area is no longer constrained by electrochemical cell size, this technique can be directly applied to layer transfer technologies in photovoltaics or surface micromachining in microsystem technologies reducing process complexities and improving the yield. The Pt can be recycled after the process and in principle be reused.

(3) We applied the obtained SiNWs to PEC water splitting. SiNWs show a superior performance over planar Si in both enhanced photocurrent and anodic shift of onset potential (Vos). The purification effect in UMG-Si also improves the photocurrent by more than ~35%. Through post KOH etching of Si nanowires (SiNWs), we obtained tapered SiNWs with a surface area and shape that is gradually tuned. This simple approach enables us to study the effects of nanostructured Si on the HER by excluding several interference factors, such as surface area, light absorption and surface defect density. We find that instead of pursing excellent light absorption in nanostructured Si, controlling the surface defect density is of critically importance for achieving high photocurrents. The tapered SiNW with shrunk sizes after KOH etching also provides direct evidence that the anodic shift of Vos is due to the surface effect. Thus, Si nanostructures should be small enough to induce strong band bending inside the SiNWs. Combining theoretical simulations and the experimental approach, we prove that tapered SiNW is an excellent candidate for the photoelectrochemical HER. With careful surface passivation, the efficiency of tapered SiNWs can achieve the theoretical limit.

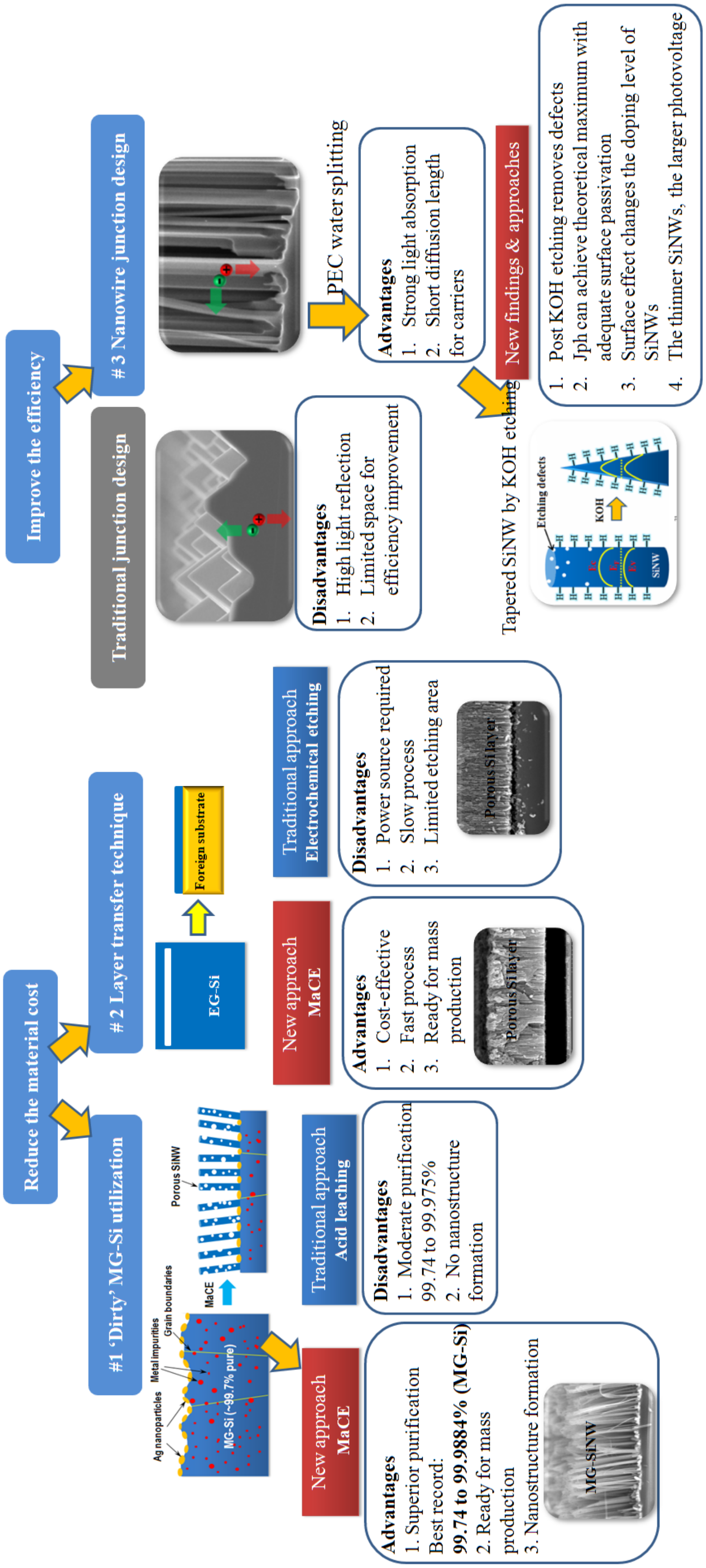

Figure 6.1 Final overview of the results (the text in red square represents our approaches).

6.2 Outlook of nanostructured Si based solar energy conversion device

Nanostructured Si provides a unique platform to design a new generation Si solar energy conversion devices, which is optically thick and electrically thin. Based on our understandings and the results presented in this thesis, we offer some suggestions for further boosting the cell efficiency:

(1) For minimization of surface recombination, Si nanostructures should have the surface area as small as possible while keeping perfect light absorption.

(2) Strong band bending in Si nanostructures is favorable for creating a large photovoltage or reducing the onset potential for water splitting. Through careful surface engineering (e.g. surface functionalization, changing absorbates), the band bending can be modulated. Doping at the nanoscale is always challenging, surface engineering may offer a new way to carefully control the electron or hole concentration inside Si nanostructures. Thus, real nanoscale radial p-n junction solar cells (<100 nm) seem possible.

(3) For a significant reduction of the surface recombination velocity, passivation layers deposited at the surface of nanostructured Si (e.g. Al_2O_3, TiO_2) are required. Al_2O_3 would be adequate for solid state solar cells. For PEC cells, n-type TiO_2 would be an ideal layer not only for passivation, but also for improving the photovoltage and stability.

RERFERENCES

1.Gray F. Moore, Fary W. Brudvig, Enengy conversion in photosynthesis: A paradigm for solar fuel production, Annu. Rev. Condens. Matter. Phys. 2 (2011) 303-327.

2. Renewables 2012 Global status report, website: www.ren21.net.

3. Basic Research Needs for Solar Energy Utilization. Report of the basic energy sciences workshop on solar energy utilization, 2005. Website: science.energy.gov.

4.B. Kumar, M. Llorente, J. Froehlich, T. Dang, A. Sathrum, C. P. Kubiak, Annu. Rev. Phys. Chem. 63 (2012) 541.

5. M. T. Mayer, Y. Lin, G. Yuan, D. Wang, Acc. Chem. Res. 46 (2013) 1558.

6. D. A. Tryk, A. Fujishima, K. Hona, Electrochimica Acta 45 (2000) 2363.

7. Renewable energy technologies: cost analysis series. International Renewable Energy Agency (IRENA) volume 1: power sector, website: http://www.irena.org/

8. AE. Bequerel, Recherches sur les effets de la radiation chimique de la lumière solaire, au moyen des courants électriques. C.R. Acad. Sci. 9, 145–149 (1839).

9. J. Britt, C. Ferekides, Appl. Phys. Lett. 62 (1993) 2851.

10. C.-W. Cheng, K.-T. Shiu, N. Li, S.-H. Han. L. Shi, D. K. Sadana, Nature Comm. 4 (2012) 1577.

11. Y. Itzhaik, O. Nittsoo, M. Page, G. Hodes, J. Phys. Chem. C 113 (2009) 4254.

12. P. Jackson, D. Hariskos, E. Lotter, S. Paetel, R. Wuerz, R. Menner, W. Wishmann, M. Powalla, Prog. in Photovol: Res. App. 19 (2011) 894.

13. A. Luque, S. Hegedus, Handbook of photovoltaic science and engineering. 2nd Edition.

14. M. A Green, K. Emery, Y. Hishikawa, W. Warta, E. D. Dunlop, Solar efficiency tables (version 40) Prog. Photovolt: Res. Appl. 20 (2012) 606.

15. S. Pizzini, Solar Energy Materials Solar Cells 94 (2010) 1528.

16. A. V. Shah, H. Schade. M. Vanecek, J. Meier, E. Vallat-Sauvain, N. Wyrsch. U. Kroll, C. Droz, J. Bailat, Prog. Photovolt: Res. Appl. 12 (2004) 113.

17. http://en.wikipedia.org/wiki

18. L. Pavesi, L. D. Negro, C. Mazzoleni, G. Franzo, F. Priolo, Nature 408 (2000) 440.

19. V. Schmidt, J. V. Wittemann, U. Goesele, Chem. Rev. 110 (2010) 361.

20. M.-H. Park, M. G. Kim, J. Joo, K. Kim, J. Kim, S. Ahn, Y. Cui, J. Cho, Nano Lett. 9 (2009) 3844.

21. T. Geppert, S. L. Schweizer, U. Gösele, R.B. Wehrspohn, Appl. Phys. A, 84 (2006) 237.

22. V. Kochergin, H. Föll, Mater. Sci. Eng. R. 52 (2006) 93.

23. J.-Y. Jung, K. Zhou, H.-D. Um, Z. Guo, S.-W. Jee, K.-T. Park, J.-H. Lee, Opt. Exp. 36 (2011) 2677.

24. Y. Cui, Z. Zhong, D. Wang, W. U. Wang, C. M. Lieber, Nano Lett. 3, 149 (2003).

25. C. K. Chan, H. Peng, G. Liu, K. McIlwrath, X. F. Zhang, R. A. Huggins, Y. Cui, Nature Nanotech. 3 (2008) 31.

26. K.-T. Park, Z. Guo, H.-D. Um, J.-Y. Jung, J. M. Yang, S. K. Lim, Y. S. Kim, J.-H. Lee, Opt. Exp. 19 (2011) A41.

27. Nanostructures and Nanomaterials: Synthesis, Properties and applications. Imperial College Press, 2004.

28. X. Li, H.-S. Seo, H.-D. Um, S.-W. Jee, Y. W. Cho, B. Yoo, J.-H. Lee, Electrochimica Acta 54 (2009) 6978.

29. V. Lehmann, Electrochemistry of silicon. Wiley-VCH, Weinheim, 2002.

30. H.-S. Seo, X. Li, H.-D. Um, B. Yoo, J.-H. Kim, K.-P. Kim, Y. W. Cho, J.-H. Lee, Mater. Lett. 63 (2009) 2569.

31. X. Li, P. W. Bohn, Appl. Phys. Lett. 77 (2000) 2572.

32. K.-Q. Peng, Y. Wu, H. Fang, X. Zhong, Y. Xu, J. Zhu, Angew. Chem. Int. Ed. 44 (2005) 2737.

33. Z. Huang, N. Geyer, P. Werner, J. d. Boor, U. Gösele, Adv. Mater. 23 (2011) 285.

34. L. Schirone, G. Sotgiu, M. J. Montecchi, J. Lumin. 80 (1998) 163.

35. L. Hu, G. Chen, Nano Lett. 7 (2007) 3249.

36. J. Y. Kwon, D. H. Lee, M. Chitambar, S. Maldonado, A. Tuteja, A. Boukai, Nano Lett. 12 (2012) 5143.

37. J.-Y. Jung, Z. Guo, S.-W. Jee, H.-D. Um, K.-T. Park, J.-H. Lee, Opt. Exp. 18 (2010) A286.

38. B. M. Kayes, N. S. Lewis, H. A. Atwater, J. Appl. Phys. 97 (2005) 114302.

39. B. Tian, X. Zheng, T. J. Kempa, Y. Fang, N. Yu, G. Yu, J. Huang, C. M. Lieber, Nature 449 (2007) 885.

40. T. Song, S.-T. Lee, B. Sun, Nano Energy 1 (2012) 654.

41. L. Tsakalakos , J. Balch, J. Fronheiser , B. A. Korevaar , O. Sulima, J. Rand, Appl. Phys. Lett. 91 (2007) 233117.

42. E. C. Garnett , P. D. Yang , J. Am. Chem. Soc. 130 (2008) 9224 .

43. J.-Y. Jung, Z. Guo, S.-W. Jee, H.-D. Um, K.-T. Park, M. S. Hyun, J. M. Yang, J.-H. Lee, Nanotechnology 21 (2010) 445303.

44. J. S. Huang, C. Y. Hsiao, S. J. Syu, J. J. Chao, C. F. Lin, Sol. Energy Mater. Sol. Cells 93 (2009) 621.

45. K. Hagedorn, C. Forgacs, S. Collins, S. Maldonado, J. Phys. Chem. C 114 (2010) 12010.

46. D. R. Kim, C. H. Lee, P. M. Rao, I. S. Cho, X. Zheng, Nano Lett. 11 (2011) 2572.

47. L. He, C. Jiang, Rusli, D. Lai, H. Wang, Appl. Phys. Lett. 99 (2011) 021104.

48. J. M. Foley, M. J. Price, J. I. Feldblyum, S. Maldonado, Energy Environ. Sci. 5 (2012) 5203.

49. A. G. Cullis, L. T. Canham, P. D. Calcott, J. Appl. Phys. 82 (1997) 909.

50. J.H. Petermann, D. Zielke,J. Schmidt, F. Haase, E.G. Rojas, R. Brendel, Prog. Photovolt. Res. Appl. 20 (2012) 1.

51. J. V. Hoeymissen, V. Depauw, I. Kuzma-Filipek, K. V. Nieuwenhuysen, M. R. Payo, Y. Qiu, I. Gordon, J. Poortmans, Phys. Status Solidi A 208 (2011) 1433.

52.M. Ernst, R. Brendel, IEEE J. Photovol. 3 (2013) 723.

53. R. Brendel, Sol. Energy 77 (2004) 969.

54. Y. Xiao, X. Li, H.-D. Um, X. Gao, Z. Guo, J.-H. Lee, Electrochimica Acta 74 (2012) 93.

55. Z. P. Huang, N. Geyer, L. F. Liu, M. Y. Li, P. Zhong, Nanotechnology 21 (2010) 465301.

56. J. Oh, H.-C. Yuan, H. M. Branz, Nature Nanotech. 7 (2012) 743.

57. D. H. Wan, H. L. Chen, S. Y. Chuang, C. C. Yu, Y. C. Lee, J. Phys. Chem. C, 112 (2008) 20567.

58. K. Tsujino, and M. Matsumura, Electrochem. Solid Stat. Lett. 8 (2005) C193.

59. M. Lipinski, J. Cichoszewski, R. P. Socha, T. Piotrowski, Acta Physics Polonica 116 (2009) S117.

60. K. S. Nahm, Y. H. Seo, H. J. Lee, J. Appl. Phys. 81 (1997) 2418.

61. K. Peng, Y. Yan, S. Gao, J. Zhu, Adv. Func. Mater. 13 (2003) 127.

62. C. Chartier, S. Bastide, C. Levy-Clement, Electrochimica Acta 53 (2008) 5509.

63. O.J. Hildreth, W. Lin, C.P. Wong, ACS Nano 12 (2009) 4033.

64. K. Peng, A. Lu, R. Zhang, S.-T. Lee, Adv. Func. Mater., 18 (2008)3026.

65. C.-L. Lee, K.T. Tsujino, Y. Kanda, S. Ikeda, and M. Matsumura, J. Mater. Chem. 18 (2008) 1015.

66. A. J. Nozik, Ann. Rev. Phys. Chem. 29 (1978) 189.

67. Encyclopedia of Electrochemistry. Vol. 6 Semiconductor Electrodes and Photoelectrochemistry

68. M. G. Walter, E. L. Warren, J. R. McKone, S. W. Boettcher, Q. Mi, E. A. Santori, N. A. Lewis, Chem. Rev. 110 (2010) 6446.

69. I. Oh, J. Kye, S. Hwang, Nano Lett. 12 (2012) 298.

70. X. G. Zhang, Electrochemistry of Silicon. Kluwer Academic/Plenum Publishers, 2001.

71. J. Oh, T. G. Deutsch, H.-C. Yuan and H. M. Branz, Energy Environ. Sci., 2011, 4, 1690-1694.

72. U. Sim, H.-Y. Jeong, T.-Y. Yang, K. T. Nam, J. Mater. Chem. A, 2013, DOI: 10.1039/c3ta00048f.

73. Y. Qu, L. Liao, Y. Li, H. Zhang, Y. Huang, X. Duan, Nano Lett. 9 (2009) 4539.

74. M. Seibt, K. Graff. J. Appl. Phys. 63 (1988) 4444.

75. J. Dietl, Solar Cells 10 (1983) 145.

76. X. Zhong, Y. Qu, Y.-C. Lin, L. Liao, X. Duan, Appl. Mater. Interf. 3 (2011) 261.

77. X. Ma, J. Zhang, T. Wang, T. Li, Rare Metals 28 (2009) 221.

78. S. A. McHugo, A. C. Thompson, I. Perichaud, S. Martinuzzi, Appl. Phys. Lett. 72 (1998), 3482.

79.D. Laush, K. Petter, R. Bakowskie, J. Bauer, O. Breinstein, C. Hagendorf. 27th EUPVSEC, DOI: 10.4229/27thEUPVSEC2012-2CO.13.4.

80. Y. H.Ogata, K. Kobayashi, M. Motoyama, Curr. Opin. Solid State Mater. Sci.10 (2006) 163.

81. S. Chattopadhyay, X. Li, P. W. Bohn, J Appl. Phys. 91 (2002) 6134.

82. Y. Xiao, X. Li, H.-D. Um, X. Gao, Z. Guo, J.-H. Lee, Electrochimica Acta 74 (2012) 93.

83. R. T. Tung, Phys. Rev. B 45 (1992) 13509.

84. Y. Nakato, H. Yano, S. Nishiura, T. Ueda, and H. Tsubomura, J. Electroanal. Chem. 228 (1987) 97.

85. Z. Huang, N. Geyer, L.F. Liu, M.Y. Li, P. Zhong, Nanotechnology 21 (2010) 465301.

86. D. Q. Liu, D. J. Blackwood, J. Electrochem. Soc. 159 (2012) H909.

87. H. Föll, M. Christophersen, J. Carstensen, G. Hasse, Mat. Sci. Eng. R 39 (2002) 93.

88. L. T. Canham, Appl. Phys. Lett. 57 (1990) 1046.

89. W.-K. To, C.-H. Tsang, H.-H. Li, Z. Huang, Nano Lett. 11, 5252 (2011).

90. S. M. Sze, K. K. Ng, Physics of semiconductor devices; Wiley, NJ, 2007.

91. P.Sharma, Y.-L. Wang, Appl. Phys. Exp. 4, 025001(2011).

92. J.-N. Chazalviel, R.B. Wehrspohn, F. Ozanam, Mat. Sci. Eng. B 69-70 (2000) 1.

93. J. Kim, Y. H. Kim, S.-H. Choi, W. Lee, ACS Nano 5 (2011) 5242.

94. X. Li, Y. Xiao, J. H. Bang, D. Lausch, S. Meyer, P.-T. Miclea, J.-Y. Jung, S. L. Schweizer, J.-H. Lee, R. B. Wehrspohn, Adv. Mater. 25 (2013) 3187.

95. J. M. Foley, M. J. Price, J. I. Feldblyum, S. Maldonado, Energy Environ. Sci. 5 (2012) 5203.

96. I. Oh, J. Kye, S. Hwang, Nano Lett. 12 (2012) 298-302.

97. J. Oh, T. G. Deutsch, H.-C. Yuan, H. M. Branz, Energy Environ. Sci., 4 (2011) 1690.

98. U. Sim, H.-Y. Jeong, T.-Y. Yang, K. T. Nam, J. Mater. Chem. A, 2013, DOI: 10.1039/c3ta00048f.

99. L. Tsakalakos, J. Balch, J. Fronheiser, M.-Y. Shih, S. F. LeBoeuf, M. Pietrzykowski, P. J. Codella, B. A. Korevaar, O. Sulima, J. Rand, A. Davuluru, U. Rapol. J. Nanophotonics, 1 (2007) 013552.

100. K. Hagedorn, C. Forgacs, S. Collins, S. Maldonado, J. Phys. Chem. C 114 (2010) 12010.

101. N. S. Lewis, Inorgan. Chem. 44 (2005) 6900.

102. T. Geppert, S. L. Schweizer, U. Goesele, R. B. Wehrspohn, Appl. Phys. A. 84 (2006) 237.

103. C.-S. Guo, L.-B. Luo, G.-D. Yuan, X.-B. Yang, R.-Q. Zhang, W.-J. Zhang, S.-T. Lee, Angew. Chem. Int. Ed. 121 (2009) 10080.

104. F. Camacho-Alanis, H. Castaneda, G. Zangari, N. S. Swami, Langmuir, 27 (2011) 11273.

Publications

Some parts and figures of this work have appeared previously in the following publications:

Journal articles and conference papers

(1) **X. Li**, Y. Xiao, J. H. Bang, D. Lausch, S. Meyer, P.-T. Miclea, J.-Y. Jung, S. L. Schweizer, J.-H. Lee, R. B. Wehrspohn
Upgraded silicon nanowires by metal-assisted etching of metallurgical silicon: a new route to nanostructured solar-grade silicon
Adv. Mater. 25 (2013) 3187.

(2) **X. Li**, Y. Xiao, C. Yan, J.-W. Song, V. Talalaev, S. L. Schweizer, K. Piekielska, A. Sprafke, J.-H. Lee, R. B. Wehrspohn
Fast electroless fabrication of uniform mesoporous silicon layers
Electrochimica Acta 94 (2013) 57.

(3) **X. Li**, Y. Xiao, C. Yan, K. Zhou, S. L. Schweizer, A. Sprafke, J.-H. Lee, R. B. Wehrspohn
Influence of the mobility of Pt Nanoparticles on the anisotropic etching properties of silicon
ECS Solid State Letters 2 (2013) 22.

(4) **X. Li**, S. L. Schweizer, A. Sprafke, J.-H. Lee, R. B. Wehrspohn
Nanowires from dirty multi-crystalline Si for hydrogen generation
Proc. of SPIE 2013, doi:10.1117/12.2024231

(5) **X. Li**, A. Sprafke, S. Schweizer, R.B. Wehrspohn
Purifying metallurgical silicon to solar grade silicon by metal assisted chemical etching
OSA conference: Renewable Energy & the Environment (2013)

http://dx.doi.org/10.1364/FREEFORM.2013.JM3A.8

(6) M. Otto, M. Kroll, B. Gesemann, **X. Li**, A. N. Sprafke, R. B. Wehrspohn et al.
Passivation of common black silicon surfaces by ALD deposited Al2O3
Photovoltaic Science and Engineering Conference PVSEC (2013)

(7) C.Yan, **X. Li**, K. Zhou, A. Pan, P. Werner, S.L. Mensah, A.T. Vogel, V. Schmidt
Heteroepitaxial growth of GaSb nanotrees with an ultra-low reflectivity in a broad spectral range
Nano Lett. 12 (2012) 1799.

(8) **X. Li**, A. Sprafke, S. Schweizer, R. B. Wehrspohn
Wet chemical etched silicon structures for solar energy conversion:nano- vs micro-structures
OSA conference Eindhoven: http://dx.doi.org/10.1364/E2.2012.JM5A.8

(9) Y. Xiao, **X. Li**, H.-D. Um, X. Gao, Z. Guo, J.-H. Lee
Controlled exfoliation of a heavily n-doped porous silicon double layer electrochemically etched for layer-transfer photovoltaics
Electrochimica Acta 74 (2012) 93.

(10) K. Zhou, Z. Guo, **X. Li**, J.-Y. Jung, S.-W. Jee, K.-T. Park, H.-D. Um, N. Wang, J.-H. Lee
The tradeoff between plasmonic enhancement and optical loss in silicon nanowire solar cells integrated with a metal back reflector
Optical Express 20 (2012) 777.

(11) **X. Li**, Z. Guo, Y. Xiao, H.-D. Um, J.-H. Lee
Electrochemically etched pores and wires on smooth and textured GaAs surfaces

Electrochimica Acta 56 (2011) 5071.

(12) **X. Li**, J.-Y. Jung, H.-D. Um, H.-S. Seo, J.-H. Lee
Triangular GaAs microcones and sharp tips prepared by combining electroless and electrochemical etching
Journal of Electrochemical Society 157 (2010) D1.

(13) **X. Li**, H.-S. Seo, H.-D. Um, S.-W. Jee, B. Yoo, J.-H. Lee
A periodic array of silicon pillars fabricated by photoelectrochemicaletching
Electrochimica Acta 54 (2009) 6978.

(14) H.-S. Seo, **X. Li**, H.-D. Um, J.-H. Kim, K.-P. Kim, J.-H. Lee,
Fabrication of truncated silicon pyramid arrays by electrochemical etching
Electrochemcial and Solid-State Letters 12 (2009) D89.

(15) H.-S. Seo, **X. Li**, H.-D. Um, J.-H. Kim, K.-P. Kim, J.-H. Lee
A vertical array of silicon nanowires and sharp tips controlled perfectly by a simple electrochemical etching
Materials Letters 63 (2009) 2567.

(16) H.-D. Um, J.-Y. Jung, **X. Li**, S.-W. Jee, K.-T. Park, H.-S. Seo, J.-H. Leeet al.
A novel photovoltaic nanodevice based on the co-integration of silicon micro and nanowires prepared by electroless etching with conformal plasma doping
International Electron Devices Meeting 2009, (IEEE/IEDM)

(17) S. Yu, G. Kang, **X. Li**, H. Li
Study on the release performance of encapsulated lavender oil

Flavour Fragrance Cosmetics 4 (2008) 17.

Journal articles (In preparation or in submission)

(18) **X. Li**, C. Yan,Y. Xiao,S. L. Schweizer, A. Sprafke , J.-H. Lee, R. B. Wehrspohn
High performance porous metallurgical silicon nanowire for lithium ion battery
In preparation

(19) **X. Li**, Y. Xiao, S. Meyer,S. L. Schweizer, A. Sprafke, J.-H. Lee, R. B. Wehrspohn
Porous Si nanowire self-purified from metallurgical Si: A new etching model
In submission

(20) **X. Li**, Y. Xiao, X. Zhou, S. L. Schweizer, A. Sprafke , J.-H. Lee, R. B. Wehrspohn
Towards maximal hydrogen evolution by applying tapered Si nanowire as photocathode
In submission

(21) J.-Y. Jung, S.-W. Jee, H.-D. Um, **X. Li**, K.-T. Park, J.-H. Bang, J.-H. Kim, J.-H. Lee
A high-performance photoelectrochemical cell employing a tapered Si nanohole array
In submission

(22) M. Otto, M. Kroll, B. Gesemann, **X. Li**, A. N. Sprafke, R. B. Wehrspohn et al.
Black silicon photovoltaics
In submission

International conference (talks and posters)

(1) *Purifying metallurgical silicon to solar grade silicon by metal assisted chemical etching*
OSA Optical Nanostructures and Advanced Materials for Photovoltaics (PV), Tucson,USA, Nov. 2013 (Poster).

(2) *Nanowires from multi-crystalline Si for hydrogen generation*
SPIE Solar Energy + Technology, San Diego, USA, Aug. 2013 (Oral).

(3) *Upgraded silicon nanowires by metal-assisted etching of metallurgical silicon*
International Nanophotonics and Nanoenergy Conference (INPC), Hefei, China, May 2013 (Poster).

(4) *Silicon nanowires self-purified from metallurgical silicon: cost-efficient wire process utilizing dirty Silicon for solar energy conversion*
Material Research Society Spring Meeting, San Francisco, USA, April 2013 (Oral).

(5) *A new route for the electroless fabrication of mesoporous silicon*
German Physical Society (DPG) spring meeting, Regensburg, Germany, March, 2013 (Oral).

(6) *Wet chemical etched silicon structures for solar energy conversion: nano- vs micro-structures*
OSA Optics for solar energy, Eindhoven, Netherlands, Nov. 2012 (Poster).

(7) *Mc-Si nanowire fabricated by metal assisted chemical etching for solar energy conversion*
SPIE Photonics Europe, Brussels, Belgium, April, 2012 (Poster).

(8)*Porous silicon antireflective layer fabricated by platinum nanoparticle assisted chemical etching*

DPG Spring meeting, Berlin, Germany, March, 2012 (Poster).

(9) *Metal assisted chemical etching of Mc-Si wafers for solar cell application*

DPG Spring meeting, Dresden, Germany, March, 2011 (Poster).

(10) *Groove defined micro-pores of GaAs by electrochemical etching*

International Society of Electrochemistry (ISE) Annual meeting, 2009 (Oral).

ACKNOWLEGEMENTS

Here I wish to thank a bunch of people. Without them, I cannot finish the thesis or even start my research.

I want to express my deep gratitude to my supervisor Prof. Dr. Ralf B. Wehrspohn. Without his support, I cannot start my work and have fruitful results after three years' study in Halle. His guidance and suggestions brought me to the right way of doing good research. His deep insight views in both academics and industry taught me how to do meaningful research.

I wish to thank my previous supervisor Prof. Dr. Jung-Ho Lee. He is the person who guided me to semiconductor nanoscience, and taught me how to write the first paper. He strongly supported my research during pursing my master and doctor degree.

I want to thank my colleagues, Dr. Stefan L. Schweizer, Dr. Alexander Sprafke, Prof. Jin Ho Bang, Dr. Joerg Schilling, Dr. Yan Chenglin, Dr. Zhou Keya, Dr. Paul-Tiberiu Miclea, Dr. Andreas Graff, Martin Otto, Dominik Lausch, Jens Beyersdorfer, Claudia Stehr, Doreen Rawald and Susanne Wille for material characterization, scientific discussion and help in daily working days. I would always remember nice words from Stefan and Claudia whenever I do experiments. I would like to thank Dr. Sylke Meyer, who helped me out from the difficult elemental analysis trap.

I am very grateful for my junior Xiao Yanjun. Without his hard work, the road to publishing a nice paper would be impossible. I really appreciate hard work from my Hiwi Maik Rothe, and Junna Wang. I also wish to thank my colleagues in Korea Sang-Won, Han-Don, Jin-Young, Jae-Won, Xuejiao and Xiaoling for helping me during my stay in Hanyang University.

I am deeply indebted to my Frau Xu Ruiwen, my parents, father-in-law and mother-in-law. Without their care and support, I cannot live happily and finish my degree.

Finally, I wish to thank my friends, Wang Pei, Li Zheng for their kind accompany and help in daily life in the past three years. The financial support from International Max Planck Research School (IMPRS) for Science and Technology of Nanostructures is acknowledged.

CURRICULUM VIATE

PERSONAL INFORMATION

XIAOPENG LI (李小鹏)

202/15, No. 1333 Haiyang Road, Pudong District, Shanghai,

People’s Republic of China. Postcode: 200126

Email: lixiaopengtony@gmail.com

Birthday: 14.Nov.1986 Birthplace: Jiangsu, China

EDUCATION

08/2010-Now *Ph.D. Candidate*

Max Planck Institute of Microstructure Physics, Weinberg 2, 06120 Halle (Saale),Germany

Fachgruppe µMD, Martin Luther University Halle-Wittenberg, Heinrich-Damerow-Str.4, 06120 Halle (Saale),Germany

*Aug. 2007~Aug. 2009*Master in Science

Department of Bio-nanotechnology, Hanyang University, Ansan, South Korea

Sep. 2003 ~ July 2007 Bachelor in Chemical Engineering and Technology

Department of Chemical Engineering, East China University of Science and Technology, Shanghai, China

DECLARATION

I hereby declare that this submission is my own work and to the best of my knowledge it contains no materials previously published or written by another person, nor material which to a substantial extent has been accepted for the award of any other degree or diploma at the Martin Luther University of Halle-Wittenberg or any other educational institutions, except where the acknowledgement is made in this thesis. Any contribution made to the research by others, with whom I have worked in Germany, Korea, or elsewhere, is explicitly acknowledged in this thesis. I also declare that the intellectual contents of this thesis are the products of my own work, except to the extent that assistance from others in the project's design and conceptions or in style, presentation and linguistic expression is acknowledged.

Halle (Saale), August, 2013

Signature:

Li Xiaopeng